Rapid Construction of Bridge Piers with Improved Seismic Performance

--

An Initial Study into the use of Concrete Filled Steel Tubes for Bridge Piers and Foundation Connections

by

Dawn E. Lehman
and
Charles W. Roeder

Department of Civil Engineer
University of Washington
Seattle, WA 98195

January 2012

Final Report No. CA12-1972

Final Report submitted to the California Department of Transportation (Caltrans) under Contract No. 59A0641

STATE OF CALIFORNIA DEPARTMENT OF TRANSPORTATION

TECHNICAL REPORT DOCUMENTATION PAGE

TR0003 (REV. 10/98)

1. REPORT NUMBER	2. GOVERNMENT ASSOCIATION NUMBER	3. RECIPIENT'S CATALOG NUMBER
CA12-1972		

4. TITLE AND SUBTITLE	5. REPORT DATE
Rapid Construction of Bridge Pier with Improved Seismic Performance	September 14, 2012
	6. PERFORMING ORGANIZATION CODE
7. AUTHOR(S) Dawn E. Lehman, Charles W. Roeder	8. PERFORMING ORGANIZATION REPORT NO.
9. PERFORMING ORGANIZATION NAME AND ADDRESS Department of Civil and Environment Engineering University of Washington 3935 University Way NE Seattle, WA 98105-6613	10. WORK UNIT NUMBER
	11. CONTRACT OR GRANT NUMBER 59A0641
12. SPONSORING AGENCY AND ADDRESS California Department of Transportation Engineering Service Center 1801 30th Street, MS 9-2/5i Sacramento CA 95816 California Department of Transportation Division of Research and Innovation, MS-83 1227 O Street Sacramento CA 95814	13. TYPE OF REPORT AND PERIOD COVERED Final Report 6/2/2008 – 12/1/2011
	14. SPONSORING AGENCY CODE 913

15. SUPPLEMENTAL NOTES

Prepared in cooperation with the State of California Department of Transportation.

16. ABSTRACT

Concrete filled steel tubes (CFTs) promote economical and rapid construction. For a given section, they offer increased strength and stiffness relative to structural steel and reinforced concrete construction, thereby allowing use of smaller sections. The steel tube serves as formwork and reinforcement to the concrete fill, thereby substantially reducing the labor requirements. CFT components encourage the optimal behavior of each material (concrete and steel) while providing a symbiotic relationship between the two to mitigate undesirable failure modes. The fill increases the compressive strength and stiffness, delays and restrains local buckling of the tube, and enhances ductility and resistance if composite action is achieved.

Both rectangular and circular CFT have been employed, but circular CFT provide better performance, because they provide increased confinement of the concrete and composite action. A missing component for circular CFT construction is reliable and ductile connection designs. The research described herein investigated and develops design procedures for simple and economical connections of circular CFT piers or columns to reinforced concrete foundations, pile caps and wide cap beams. The connection requires no dowels or internal reinforcement connecting the tube to the footing or cap beam. Experiments and analytical studies evaluate the inelastic seismic performance and establish design criteria for the connection. The seismic performance of a CFT column and connection assembly is compared to a conventional reinforced concrete column. The research shows that the proposed connection develops the full capacity of the composite column. The assembly provides excellent ductility and inelastic deformation capacity under seismic loading while mitigating damage even at larger drift demands.

17. KEY WORDS	18. DISTRIBUTION STATEMENT
Concrete filled tubes, CFT, Columns, Rapid Construction, Earthquake Engineering, Seismic Design	No restrictions. This document is available to the public through the National Technical Information Service, Springfield, VA 22161

19. SECURITY CLASSIFICATION (of this report)	20. NUMBER OF PAGES	21. PRICE
Unclassified	105	

Reproduction of completed page authorized

DISCLAIMER STATEMENT

This document is disseminated in the interest of information exchange. The contents of this report reflect the views of the authors who are responsible for the facts and accuracy of the data presented herein. The contents do not necessarily reflect the official views or policies of the State of California or the Federal Highway Administration. This publication does not constitute a standard, specification or regulation. This report does not constitute an endorsement by the Department of any product described herein.

For individuals with sensory disabilities, this document is available in Braille, large print, audiocassette, or compact disk. To obtain a copy of this document in one of these alternate formats, please contact: the Division of Research and Innovation, MS-83, California Department of Transportation, P.O. Box 942873, Sacramento, CA 94273-0001.

ACNOWLEDGEMENTS

Leadership and administration of the grant was deftly provided by Caltrans. The following individuals are thanked for their participation in the project: Ron Bromenshenkel, Michael Cullen, and Peter Lee. Their contact information is provided below.

Ron Bromenschenkel rbromens@dot.ca.gov (916) 227-8151

Michael Cullen mcullen@dot.ca.gov (916) 227-8296

Peter Lee plee@dot.ca.gov (916) 227-8442

TABLE OF CONTENTS

Chapter 1 INTRODUCTION 1

1.1 Research Program 1
1.2 Report Layout 2

Chapter 2 CURRENT DESIGN MODELS FOR AND PRIOR RESEARCH ON CFT 3

2.1 Current Design Methods for CFT 4
2.2 Prior Experimental Results on CFT Beam-Column Components 8
2.3 CFT Column-to-Foundation Connection Tests 11
2.4 Analysis and Evaluation of Simplified Design Models 17
2.5 Continuum (FEM) analysis methods 25

Chapter 3 EXPERIMENTAL PROGRAM 31

3.1 Test Matrix 33
3.2 Specimen Layout and Design 35
3.3 Experimental Setup 36
3.4 Instrumentation 40

Chapter 4 CALTRANS CONNECTION EXPERIMENTAL RESULTS 46

4.1 Overview of Test Matrix 46
4.2 Summary of Individual Test Results 47
4.3 Summary Comments and Further Analysis 65

Chapter 5 DESIGN EXPRESSIONS FOR CFT COLUMNS AND FULLY RESTRAINED FOOTING AND CAP-BEAM CONNECTIONS 66

5.1 Introduction 66
5.2 Design of CFT Bridge Columns 68
5.3 Foundation (or Cap-Beam) Connection Design 77
5.4 Nonlinear Connection Model 80
5.5 Expected Seismic Performance 82
5.6 Post Earthquake Inspection and Evaluation 85
5.7 Design Example 87

LIST OF FIGURES

FIGURE 2-1 MODELS FOR PREDICTION OF RESISTANCE OF CFT 5
FIGURE 2-2 AXIAL LOAD-BENDING MOMENT INTERACTION CURVES FOR CFT 6
FIGURE 2-3 SCHEMATIC OF CFT TEST CONFIGURATIONS 10
FIGURE 2-4 PROPOSED CFT PIER OR COLUMN FOUNDATION CONNECTIONS 11
FIGURE 2-5 TYPICAL TEST SPECIMEN 13
FIGURE 2-6 PHOTO OF SPECIMEN AND TEST SETUP 14
FIGURE 2-7 SPECIMEN-I PERFORMANCE 16
FIGURE 2-8 SPECIMEN-III 16
FIGURE 2-9 COMPARISON OF MEASURED TO PREDICTED PLASTIC STRESS DISTRIBUTION MOMENT RESISTANCE 18
FIGURE 2-10 GEOMETRY USED FOR CLOSED FORM DERIVATION OF STRESS DISTRIBUTION PREDICTION 19
FIGURE 2-11 COMPARISON OF PROPOSED STIFFNESS MODELS IN MEASURED STIFFNESS . 21
FIGURE 2-12 MEASURED VS. PREDICTED MOMENT-CURVATURE BEHAVIOR USING DIFFERENT CONCRETE MODELS IN A FIBER-BASED CROSS SECTION ANALYSIS 23
FIGURE 2-13 EVALUATION OF FIBER-BASED CROSS SECTION MODEL MOMENT PREDICTION USING INAI CONCRETE CONSTITUTIVE MODEL 24
FIGURE 2-14 ABAQUS FINITE ELEMENT MESH AND MODEL 26
FIGURE 2-15 TYPICAL MATERIAL MODELS FOR ANALYSIS 27
FIGURE 2-16 COMPARISON WITH COMPRESSION TEST RESULTS OF SCHNEIDER (1998) 28
FIGURE 2-17 VERIFICATION OF FE MODEL FOR CFT UNDER COMBINED LOADING (MARSON AND BRUNEAU 2004) 29
FIGURE 2-18 VERIFICATION OF CRACK DEVELOPMENT PREDICTIONS 30
FIGURE 3-1 GEOMETRY AND FOOTING REINFORCEMENT 36
FIGURE 3-2 TEST SETUP 37
FIGURE 3-3 SPHERICAL BEARING AND LOW FRICTION SLIDING SURFACE 38
FIGURE 3-4 TYPICAL LATERAL DEFORMATION TEST PROTOCOL 40
FIGURE 3-5 TYPICAL STRAIN GAUGE PLACEMENT 41
FIGURE 3-6 STRAIN GAUGE PLACEMENT ON FOOTING REINFORCEMENT OF SPECIMEN C-7 41
FIGURE 3-7 TYPICAL POTENTIOMETER LOCATIONS 42
FIGURE 3-8 TYPICAL LVDT PLACEMENT 43
FIGURE 3-9 TYPICAL INCLINOMETER PLACEMENT 44
FIGURE 3-10 OPTOTRAK MEASURING SYSTEM 45
FIGURE 4-1 MOMENT-ROTATION BEHAVIOR OF SPECIMEN CT-1 48
FIGURE 4-2 PHOTOS OF SPECIMEN CT-1 49
FIGURE 4-3 MOMENT-ROTATION BEHAVIOR OF SPECIMEN CT-2 50
FIGURE 4-4 PHOTOS OF SPECIMEN CT-2 51
FIGURE 4-5 MOMENT-ROTATION BEHAVIOR OF SPECIMEN CT-3 53
FIGURE 4-6 CRACK FORMATIONS ON SOUTH SIDE OF SPECIMENS (0.6% DRIFT) 53
FIGURE 4-7 PHOTOS OF SPECIMEN CT-3 54
FIGURE 4-8 MOMENT-ROTATION BEHAVIOR OF SPECIMEN CT-4 55
FIGURE 4-9 PHOTOS OF SPECIMEN CT-4 56
FIGURE 4-10 MOMENT-ROTATION BEHAVIOR OF SPECIMEN CT-5 58
FIGURE 4-11 PHOTOS OF SPECIMEN CT-5 58
FIGURE 4-12 MOMENT-ROTATION BEHAVIOR OF SPECIMEN CT-6 61
FIGURE 4-13 PHOTOS OF SPECIMEN CT-6 62
FIGURE 4-14 PHOTOS OF SPECIMEN CT-7 63
FIGURE 4-15 MOMENT-ROTATION CURVE OF SPECIMEN CT-7 64
FIGURE 5-1 MONOLITHIC FOUNDATION CONNECTION 67
FIGURE 5-2 GROUTED FOUNDATION CONNECTION 67
FIGURE 5-3 WELDED ANNULAR RING 67
FIGURE 5-4 COMPARISON OF PROPOSED STIFFNESS MODELS TO MEASURED STIFFNESS .. 71
FIGURE 5-5 STRENGTH DETERMINATION 72

FIGURE 5-6 GEOMETRY USED FOR CLOSED FORM DERIVATION OF STRESS DISTRIBUTION PREDICTION 73
FIGURE 5-7 COMPARISON OF MEASURED TO PREDICTED PSDM RESISTANCE 74
FIGURE 5-8 CONSTRUCTION OF THE STABILITY-BASED INTERACTION CURVE..... 76
FIGURE 5-9 CONE PULLOUT REQUIREMENTS FOR THE EMBEDDED CONNECTION 78
FIGURE 5-10 DETAILING OF REINFORCEMENT ADJACENT TO THE TUBE..... 80
FIGURE 5-11 PROPOSED MODELS FOR NONLINEAR DEFORMATION OF CFT PIERS..... 81
FIGURE 5-12 COMPARISON OF RC AND CFT PIER PERFORMANCE 84
FIGURE 5-13 FOOTING DAMAGE 86
FIGURE 5-14 ELEVATION OF BRIDGE USED IN DESIGN EXAMPLE 87
FIGURE 5-15 P-M INTERACTION DIAGRAM OF COLUMN EXAMPLE..... 89
FIGURE 5-16 COMPARISON OF CFT AND RC COLUMN CROSS SECTIONS 91
FIGURE 5-17 CFT CONNECTION DESIGN..... 91

LIST OF TABLES

TABLE 2.1 CIRCULAR CFT TEST DATA 9
TABLE 2.2 SUMMARY OF TEST SPECIMENS AND RESULTS 13
TABLE 2.3 COMPARISON OF CALCULATED MOMENT STRENGTH RATIOS FOR FIBER-BASED SECTIONAL ANALYSIS 25
TABLE 3.1 TEST MATRIX 34
TABLE 4.1 EXPERIMENTAL PARAMETERS AND TEST RESULTS 46
TABLE 5.1 CONCRETE MIX USED IN TEST SPECIMENS 69

A_c = cross-sectional area of concrete, Sections 2.1, 2.3, 2.4, 3.3, 5.2

A_{cc} = cross-sectional area of concrete in compression, Sections 2.1, 2.4, 5.2

A_s = cross-sectional area of steel, Sections 2.1, 2.3, 2.4, 3.3, 5.2

A_{sc} = cross-sectional area of steel tube in compression, Sections 2.1, 2.4, 5.2

A_{st} = cross-sectional area of steel tube in tension, Sections 2.1, 2.4, 5.2

b_f = width and depth of footing, Section 5.3

c = depth from the location of maximum compressive strain to neutral axis depth, Section 2.1
half the distance across the CFT face at the location of the neutral axis, Sections 2.4, 5.2

C_c = resultant compressive force of concrete ($0.95A_{cc}f'_c$), Sections 2.1, 5.2, 5.7

C_{max} = sum of compression forces in concrete and steel (C_c+C_s), Sections 5.3, 5.7

C_s = resultant compressive force of steel ($A_{sc}F_y$), Sections 2.1, 5.2, 5.7

C_3 = constant for calculation of effective CFT flexural rigidity (EI_{eff}), Section 2.1

C' = constant for calculation of effective CFT flexural rigidity (EI_{eff}), Sections 2.4, 5.2

D = steel tube outer diameter, Sections 1.2, 2.1, 2.2, 2.4, 3.1, 4.1, 4.2, 5.2, 5.3, 5.4, 5.7

d_b = diameter of reinforcing bar, Section 5.3

d_f = total depth of footing, Sections 5.3, 5.7

D_o = annular ring outside diameter for monolithic connection, diameter of corrugated metal form surrounding annular ring in grouted connection, Section 5.3

E_c = modulus of elasticity of concrete, Sections 2.1, 2.4, 5.2, 5.7

E_s = modulus of elasticity of steel, Sections 2.1, 2.4, 5.2, 5.7

EI_{eff} = effective flexural stiffness, Sections 2.1, 2.4, 5.2, 5.7

f'_c = specified compressive strength of concrete, Sections 2.1, 2.3, 3.3, 5.2, 5.3, 5.7

f'_{cf} = specified compressive strength of concrete in footing, Section 5.3

f'_{ct} = specified compressive strength of concrete in tube, Section 5.2

F_{exx} = ultimate tensile strength of weld steel, Section 5.3

F_u = ultimate tensile strength of steel, Sections 3.1, 5.3

F_y = specified yield stress of steel, Sections 2.1, 2.3, 2.4, 3.1, 3.3, 5.2, 5.7

h = concrete depth below steel tube, Section 5.3

I_c = concrete moment of inertia, Section 5.2

I_g = gross cross section moment of inertia, Section 2.1

I_s = steel tube moment of inertia, Sections 2.1, 5.2

K = effective length factor for members in compression, Section 2.4,
elastic stiffness of deflection at the inflection point of the column, Section 5.4

l = length of member in compression, Section 2.4

l_e = embedment depth of CFT into foundation, Sections 3.1, 4.1, 5.3

L_t = length of the tube from the top of the footing to the inflection point, Section 5.4

M = moment strength of CFT subjected to combined bending and axial loading, Sections 2.4, 5.2

M_u = moment strength of CFT subjected to combined bending and axial loading based on plastic stress distribution method, Section 5.4
required moment strength, Section 5.7

P = compression strength of CFT subjected to combined bending and axial loading, Sections 2.1, 2.4, 5.2

P_{cr} = critical buckling load, Sections 2.1, 5.2

P_e = elastic buckling load by the Euler equation, Sections 2.1, 5.2

P_o = compression strength ($0.95f'_cA_c+F_yA_s$), Sections 2.1, 2.3, 2.4, 5.2, 5.7

P_u = required axial strength, Section 5.7

R = empirical term used to relate moment and rotation with a recommended value of 4, Section 5.4

r = radius of gyration of compression member, Section 2.4

steel tube outer radius, Sections 2.4 Equation 4a, 5.2

r_i = steel tube inner radius, Sections 2.4, 5.2

r_m = steel tube mean radius (r-$t/2$), Sections 2.4, 5.2

s = maximum footing tie spacing in the region bounded by $1.5l_e$ ($l_e/2.5$), Section 5.3

t = steel tube thickness, Sections 1.2, 2.1, 2.2, 2.4, 3.1, 4.2, 5.2, 5.3, 5.4, 5.7

T_s = resultant tensile force of steel ($A_{st}F_y$), Sections 2.1, 5.2, 5.7

w = minimum weld size between steel tube and annular ring, Section 5.3

y = distance from centroid to neutral axis, Sections 2.4, 5.2

β_d = constant used for calculation of effective CFT flexural rigidity (EI_{eff}), usually equivalent to 1, Section 2.1

β_1 = factor relating depth of equivalent rectangular compressive stress block to neutral axis depth, Section 2.1

Δ = deflection at the inflection point of the column (Δ/L_t), Section 5.4

Δ_p = deflection at the inflection point at the ultimate moment strength of the column (M_u/K), Section 5.4

δ_s = moment magnification factor, Section 5.7

ε_{cc} = compressive strain in concrete, Section 2.4

ε_{sc} = compressive strain in steel, Section 2.4

ε_{st} = tensile strain in steel, Section 2.4

ε_y = yield strain of steel, Section 2.4

θ = angle measured from the centroid of the CFT to the intersection of the neutral axis and the inner radius, r_i, of the steel tube, Sections 2.4, 5.2
connection rotation, Section 5.3

φ = curvature, Section 2.4
strength reduction factor, Section 5.7

ψ = concrete dilatation angle, Section 2.5

Chapter 1
Introduction

Modern bridge construction requires practical methods to both enhance rapid and efficient construction and meet strict engineering performance requirements for construction in high seismic zones are needed. Bridges building using concrete-filled tube (CFT) pier columns can meet these diverse requirements. CFTs offer high strength, stiffness, and deformability while eliminating the time and costs associated with column formwork and reinforcing cage construction. CFT element permit the use of modern self-consolidating concretes, with further reduces labor and construction time. Use of this construction method permits rapid field construction at reduced construction cost, and it would allow CALTRANS to meet California's transportation needs within budget while minimizing inconvenience to the traveling public.

Prior research has focused on CFT, however there are several shortcomings to that research which prohibits its use for bridge construction without further research. Most previous research has focused on the use of CFT elements for building construction, and as a result the sizes are small. In addition, few studies have focused on connections for CFT column to footings or cap beams, a critical element of a bridge, and the few studies that have focused on connections have resulted in designs that are complex and may not be applicable to bridge construction. The primary objective this research study is the development and validation appropriate pier-foundation connections, including their design and construction methods, for CFT bridge construction. A future study will focus on the pier-to-cap beam connection.

1.1. **RESEARCH PROGRAM**

The research objective was to develop a connection to achieve rapid bridge construction and superior seismic performance. The primary components of the research program were:

- A comprehensive review of past literature and research work to evaluate CFT performance and existing design rules,

- Development and evaluation of an efficient and effective column-to-footing connection through a comprehensive experimental and analytical research program, and
- Development of appropriate design guidelines and recommendations based upon this research program.

1.2. **REPORT LAYOUT**

This is the final report summarizing the research from a study into the use of CFT bridge piers for construction in high seismic zones and the CFT bridge pier-foundation connection. There are four chapters, in addition to this introduction. Chapter 2 summarizes the current design provisions, past research and evaluates current design models using those results. The results of the analysis and evaluation of Chapter 2 led to the development of experimental and analytical research program; the program built on the earlier USArmy research study, and adapted these results to bridge engineering practice. Chapter 3 summarizes the test specimens and test setup of the experimental program. The experimental results are summarized in Chapter 4. The experiments were large-scale specimens, and the test and analytical program was designed to evaluate important design considerations for both the member and the foundation connection. The results are analyzed with respect to one another and the study parameters, which included type of tube, embedment depth, and D/t ratio. Chapter 5 is the culmination of the research and the report. In Chapter 5, a detailed evaluation of the experimental results and design guidelines recommendations is conducted to develop design-office ready expressions for seismic bridge design. The recommendations presented in that chapter provide a comprehensive review of the design requirements and considerations for CFT bridge pier members as well as the pier-foundation connection, and they provide a basis for moving forward with CFT bridge piers in practice. A service-load design example is provided at the end of the chapter. The example redesigns a reinforced concrete two-column bent bridge as a CFT bridge. The bridge piers are smaller with slight increase in total steel volume.

Chapter 2

Current Design Models for and Prior Research on CFT

CFT offers many practical advantages, but it has had limited use in US construction with much wider use in Asia. Relative to conventional structural systems, such as reinforced concrete and steel, CFT components offers increased strength and stiffness. The concrete infill provides stiffness and strength in compression. The steel tube provides large tensile and compressive capacity, and the fill restrains local and global buckling. The inelastic deformation capacity of the CFT system is increased by the confinement of the concrete fill by the thin, ductile steel tube, and this significantly contributes to the seismic performance. Furthermore, CFTs permit rapid construction, because the steel tube serves as formwork and reinforcement to the concrete fill. In addition, the concrete fill can be placed without vibration using self-consolidating concrete (SCC), which in some cases can also provide an additional efficiency.

CFT may employ either circular or rectangular tubes. Rectangular CFT is used more frequently in practice, because their shape permits more direct steel-to-steel connections, but circular CFT is more applicable to deep bridge foundations and offers several major advantages. Shear stress transfer between the steel and concrete is needed to develop composite action, and prior research (Roeder et al. 2009, and Roeder et al. 1999) shows that circular CFT provides greater bond stress transfer, better confinement, and increased shear reinforcement to the concrete fill than rectangular CFT. When the bond stress for CFT members is limited, modest bending moments and some structural connection details dramatically enhance bond stress transfer. As a result, shear connectors are seldom required for these conditions. However, careful attention must be paid to the bond stress requirements for CFT components with high axial load and little or no bending moment. A secure interface between the concrete and the steel is required, and therefore concrete shrinkage must be minimized.

While circular CFT offers great benefits, it is less frequently used, because the design provisions and the structural connections for circular CFTs are not well defined. The following section summarizes the current design methods and connection details for circular CFT.

2.1 CURRENT DESIGN METHODS FOR CFT

Strength and stiffness are important design properties, and the American Institute of Steel Construction (AISC) LRFD and the American Concrete Institute (ACI) 318 Specifications (AISC 2005, ACI 2008) provide expressions to estimate these engineering parameters for CFT members. However, the two specifications provide quite different design limits and expressions for CFT. The American Association of State Highway and Transportation Officials (AASHTO) LRFD Specifications and the Seismic Design Guidelines (AASHTO 2009 and 2007) also provide design rules for CFT, which are also different from the AISC and ACI provisions.

EXPRESSIONS TO PREDICT FLEXURAL RESISTANCE

Chapter I of the AISC Specification (2005a) permits the use of (1) the plastic stress distribution or (2) the strain-compatibility method for predicting the flexural and axial resistance of circular CFT components. The plastic stress distribution method assumes that the section develops a uniform compressive stress of $0.95f'_c$ in the concrete and the full yield stress, F_y, of the steel in tension and compression as illustrated in Fig. 2.1a. The $0.95f'_c$ concrete stress is larger than the stress of $0.85f'_c$ typically used for a Whitney stress block calculation (AASHTO 2011) in recognition of the beneficial effects of concrete confinement in circular CFT. With this method, axial load and bending resistance pairs are determined by satisfying equilibrium over the cross section for each possible neutral axis location to establish the axial-moment (P-M) diagram, as shown in Fig. 2.2a. Small D/t results in larger resistance, because the area of steel is larger relative to the amount of concrete, but larger D/t values results in significantly increased bending moment for modest axial loads as shown in Fig. 3a, because of the increased contribution of concrete fill in compression. Figure 2.2b demonstrates these same effects in dimensionless form.

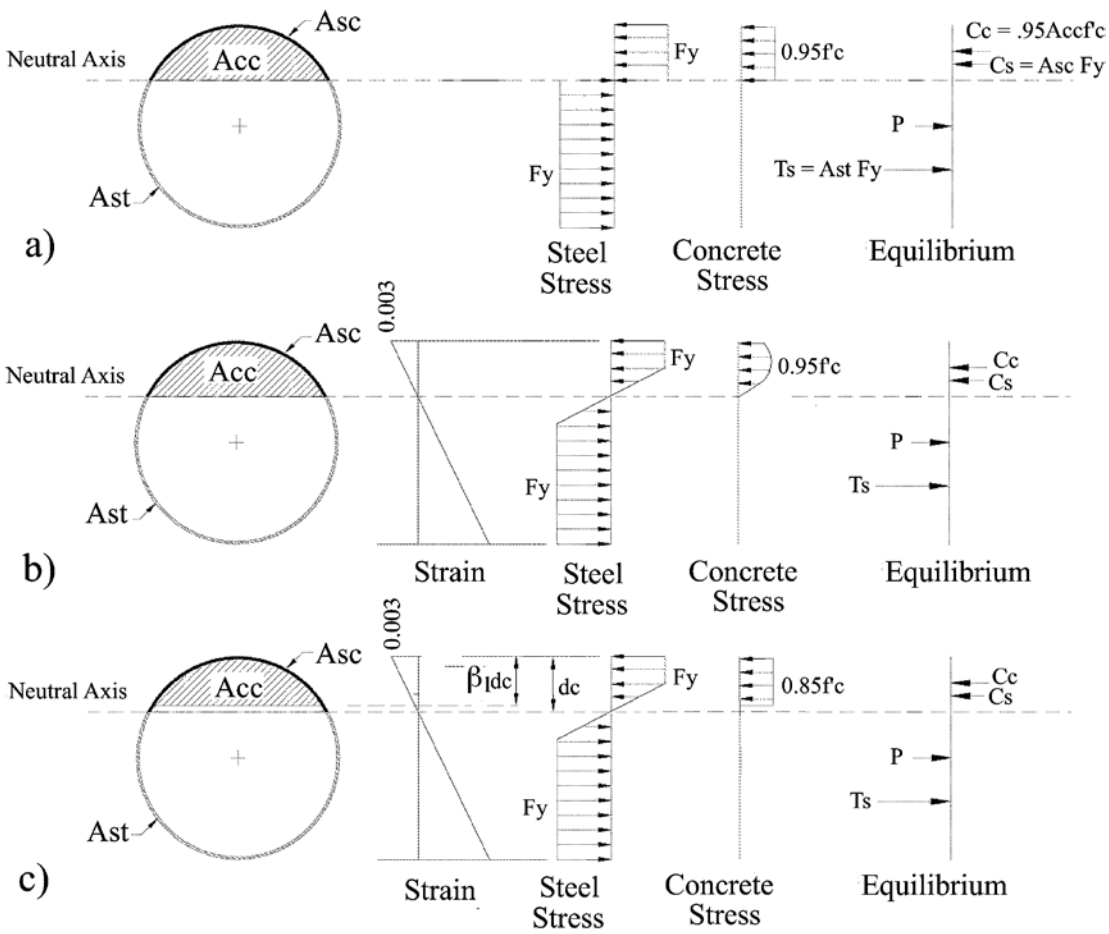

Figure 2-1. Models for Prediction of Resistance of CFT

The AISC strain compatibility method is adapted from a conventional flexural strength calculation used to predict the flexural strength of a reinforced concrete section. It employs a linear strain distribution. The material models include an elastic-perfectly plastic curve to model the steel and a parabolic curve for the concrete. By satisfying the constitutive and equilibrium relations, the flexural strength is determined for a maximum compressive strain in the concrete of 0.003 mm/mm. The ACI design procedure is similar to the AISC strain compatibility method, except that the ACI procedure uses an equivalent rectangular stress block with a compressive stress of $0.85f'_c$ acting over a depth $\beta_1 c$, where β_1 depends on the concrete strength. In the expression, c is the depth from the location of the maximum compressive strain to the neutral axis depth.

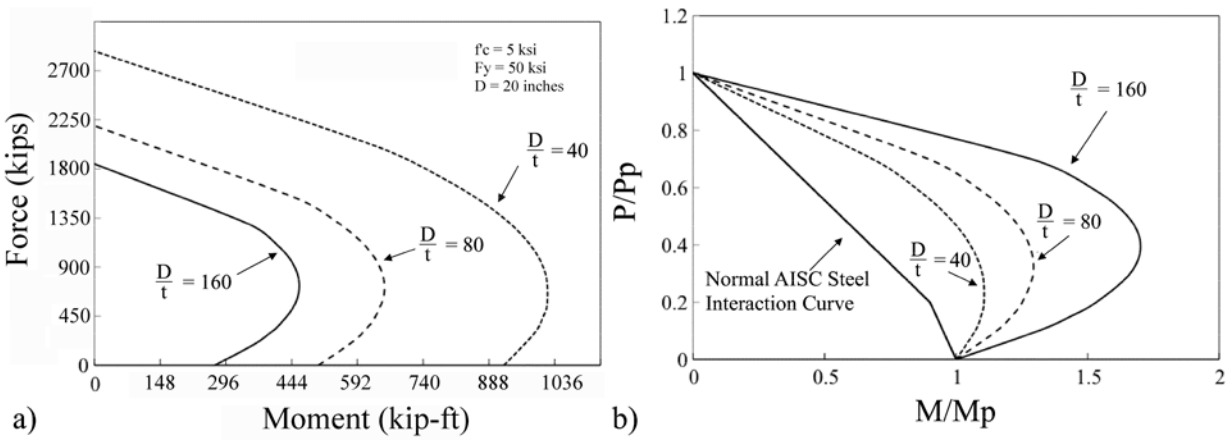

Figure 2-2. Axial Load-Bending Moment Interaction Curves for CFT: (a) Plastic Stress Distribution, (b) Normalized

The AASHTO LRFD (AASHTO 2005) Specifications (Sections 6.9.5 and 6.12.2) address the design of circular CFT, but these provisions are less sophisticated than the AISC or ACI provisions. The pure moment capacity is limited to the plastic bending capacity of only the steel section, and the axial load capacity is controlled by the yield stress of the steel and a uniform concrete stress of $0.85f'_c$. The axial load and bending moment interaction curve is essentially the interaction curve used by AISC for steel wide flange sections, as illustrated in Fig. 2.2b. The AASHTO Guide Specification for LRFD Seismic Bridge Design (Section 7.6) provides a design method that is similar to the AISC plastic stress distribution method.

STABILITY LIMITS

The D/t slenderness limit is employed to limit local buckling of the tube to assure development of the plastic capacity of the member. This limit is larger than the limit for a hollow section since the concrete fill restrains local buckling.

Again there is wide variation in these local slenderness limits among the codes. The following equations show the results from the three codes.

$$\frac{D}{t} \leq 0.15\frac{E}{F_y} \qquad \text{(AISC Provisions)} \qquad \text{(Eq. 1a)}$$

$$\frac{D}{t} \leq \sqrt{\frac{8E}{F_y}} \qquad \text{(ACI Provisions)} \qquad \text{(Eq. 1b)}$$

$$\frac{D}{t} \leq 2\sqrt{\frac{E}{F_y}} \qquad \text{(AASHTO LRFD Provisions)} \qquad \text{(Eq. 1a)}$$

These local stability limits yield very different results. For a circular CFT with a steel yield stress of 50 ksi, the limits are approximately 87, 68, and 48 for the AISC, ACI and AASHTO provisions, respectively.

Column buckling is addressed in the AISC (Section I2-1b) and AASHTO provisions by:

$$P_{cr} = 0.658^{\frac{P_o}{Pe}} P_o \qquad \text{for stocky columns where } P_e < .44P_o \qquad \text{(Eq. 2a)}$$

$$P_{cr} = 0.877 P_e \qquad \text{for slender columns where } P_e > .44P_o \qquad \text{(Eq. 2b)}$$

$$P_o = 0.95 f'_c A_c + F_y A_s \qquad \text{(Eq. 2c)}$$

where P_e is the elastic buckling load by the Euler equation, and A_c and A_s are areas of the concrete and steel, respectively. The resistance factor is 0.75 for circular CFT columns, and hence the provisions would never permit a column with axial load ratio, P/P_o, greater than 0.75 in interaction curves such as Fig. 2.2. ACI does not directly consider column buckling, but a minimum eccentricity and moment magnifier are employed to achieve a similar effect.

EFFECTIVE STIFFNESS

The effective member stiffness, EI_{eff}, of CFT is needed to define buckling capacity and determine deflections, but there is also significant variation in the design specifications:

$$EI_{eff} = E_s I_s + C_3 E_c I_c \qquad \text{by AISC Provisions} \qquad \text{(Eq. 3a)}$$

where

$$C_3 = 0.6 + \left(\frac{A_s}{A_c + A_s}\right) \qquad \text{(Eq. 3b)}$$

$$EI_{eff} = E_s I_s + \frac{.2 E_c I_g}{1 + \beta_d} \qquad \text{by ACI Provisions} \qquad \text{(Eq. 3c)}$$

$$EI_{eff} = E_s I_s + 0.4\left(\frac{E_c A_c}{A_s}\right) I_s \qquad \text{by AASHTO Provisions} \qquad \text{(Eq. 3d)}$$

A, E, and I are the area, elastic modulus, and moment of inertia of the section for the respective materials. The subscripts c, s, and g refer to properties of the concrete, steel and gross concrete sections, respectively. The contribution of internal reinforcement is included in the specification provisions, but the effect is not included in some equations discussed in this chapter, because the

CFT experiments used here do not include internal reinforcement, the effects of additional internal reinforcement. The β_d in Eq. 3c is usually approximately 1.0, and so the AASHTO and AISC provisions predict a larger effective stiffness than the ACI provisions.

2.2 PRIOR EXPERIMENTAL RESULTS ON CFT BEAM-COLUMN COMPONENTS

The first phase of this research program focused on evaluation of design models using prior data. A database of prior CFT experimental studies gathered to evaluate the accuracy and validity of design models. More than 1800 CFT tests were identified. The focus of this study is on circular concrete filled tubes with realistic sizes. This constraint was used to develop criterion to eliminate non-compliant specimens. Specifically, tests that were not included in this study included: (a) rectangular sections, (b) tests subjected to axial load only, (c) tests failing through an irrelevant failure mode such as weld fracture, (d) tests were on tubes of very small (less than 4 in.) diameter, (f) those from reports provided inadequate information to understand the tests or the specimen behavior or (g) the tests were hollow tubes used as control or reference specimens.

The resulting database compiled for this research consisted of 122 circular CFT specimens gathered from 16 test programs and 20 publications as summarized in Table 1. Comprehensive information on each test including the test setup and configuration, material properties of the steel and concrete, and detailed information regarding specimen behavior including strength, stiffness, cyclic behavior, deterioration of resistance, and inelastic deformation capacity were assembled (Bishop 2009).

The tests were divided into four broad categories as shown in Fig. 2.3: (1) CFT foundation connection tests, (2) beam-column tests, (3) eccentrically loaded column tests, and (4) pure bending (flexure only) tests. Flexural and beam-column tests typically had 3- or 4-point loading with or without an axial load, while beam-column tests had a concentrically applied axial load to evaluate combined load resistance and P-δ effects. There were 28 CFT foundation tests, 31, eccentrically loaded tests, 26 beam-column tests, and 37 flexural tests with no axial load. The D/t ratio varied between 27 and 226; the diameter, D, varied between 4 and 20 in. with most test specimens having diameters less than 12 inches. The database included a wide range of concrete and steel strengths.

Table 2.1 Circular CFT Test Data

Source	Diameter (in)	$\frac{D}{t}$	$\frac{P}{P_o}$	$\frac{Kl}{r}$	Number of Specimens	Test Information
Boyd, Cofer & McLean (1995)	8	73-107	10-14%	32-33	5	Foundation Connection
Chronister (2007)	20	80	11-21%	23-24	4	Foundation Connection
Elchalakani et al. (2001)	100-110	40 - 110	0	--	4	Flexural
Elremaily and Azizinamini (2002)	325	34 - 56	20-42%	17-18	6	Beam Column
Fujimoto, et al. (2004)	6-12	34-101	15-80%	9-19	11	Eccentrically Loaded Col.
Furlong (1967)	4-6	36-98	23-63%	21-23	10	Eccentrically Loaded Col.
Han et al. (2006)	100-200	47-105	0	--	18	Flexural
Kingsley (2005)	20	80	9%	23-24	1	Foundation Connection
Marson and Bruneau (2004)	320-405	43-74	19-33%	33-44	4	Foundation Connection
Morino et al. (1997)	9.5	27-53	40-70%	16-25	12	Beam-Column
O'Shea and Bridge (2000)	10.5-11	59-226	78-86%	23-26	6	Flexural
Prion and Boehme (1994)	6	89	15-55% 74-82% 0	21-39 80 --	7 4 5	Beam-Column Eccentrically Loaded Col. Flexural
Thody (2006).	20	80	0	--	6	Flexural Tests
Wheeler and Bridge (2006)	16-18	63-72	0	--	6	Flexural Tests
Williams (2006)	20	80	9%	23-24	2	Foundation Connection
Zhang et al. (2009)	13	57-110	29-59%	28-30	12	Foundation Connection

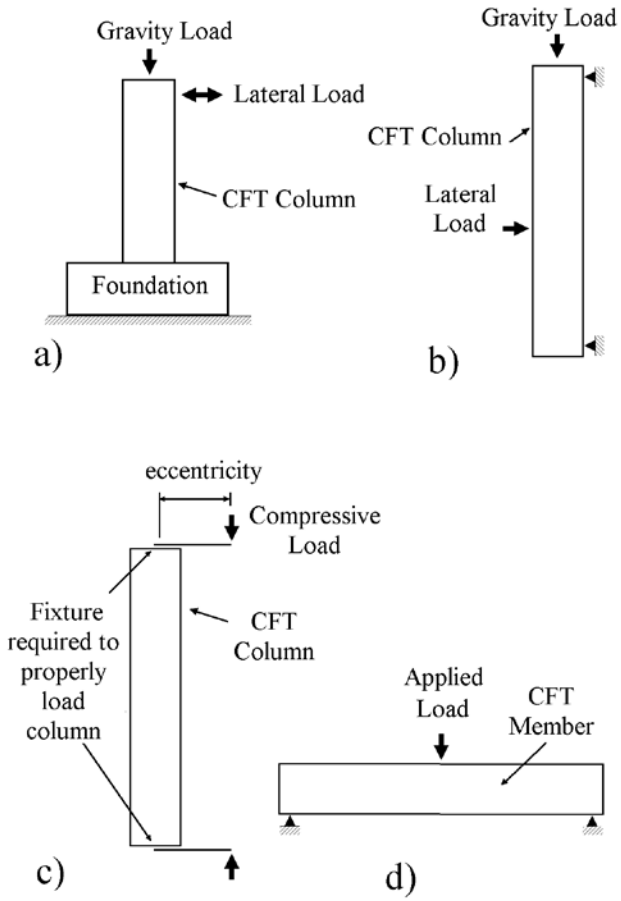

Figure 2-3. Schematic of CFT Test Configurations; a) Connection Test, b) Beam-Column Test, c) Eccentrically Loaded Column Test, d) Flexural Test

This experimental data was used to analyze, compare and evaluate alternate design models. Initial analysis of the 122 tests showed clear consistency between the flexural tests, axially loaded tests, and the beam-column tests. However, there was significant inconsistency and variability within the eccentrically loaded column tests, and between the eccentrically loaded column tests and the other three types of tests. This inconsistency was examined in detail. Figure 4c shows that eccentrically loaded tests must be loaded to provide a uniform bending moment over the column length with the only deviation caused by P-δ effects. However, this is difficult to achieve in practice, because the test apparatus must properly the stresses to both the steel and concrete elements in the proper distribution at each end of the specimen. If this stress distribution is achieved, failure will always occur at mid-height of the column where the maximum moment occurs. If this is not achieved local failure will occur at the end of the column, and some

eccentrically loaded column specimens clearly demonstrated this improper end failure. It was often impossible to separate the eccentrically loaded specimens with improper failure from those with proper end loading. As a result, all eccentrically loaded test specimens were excluded from the database, since some were not consistent indicators of CFT performance. The remaining 91 specimens were used for the continued evaluation of CFT behavior.

2.3 CFT COLUMN-TO-FOUNDATION CONNECTION TESTS

CFT offers many advantages for economical and rapid construction, and the column-to-foundation connection illustrated in Fig. 2.4 offers potential benefits for both CFT bridge piers and deep foundation connections. The connection employs a flange or annular ring, which is welded to the end of the tube with a complete joint penetration (CJP) or full strength fillet weld, as shown in Fig. 2.5c. The hollow ring projects outside and inside the tube by 16 and 8 times the flange thickness, respectively. There are no reinforcing bars in the tube or dowels penetrating from the tube into the foundation.

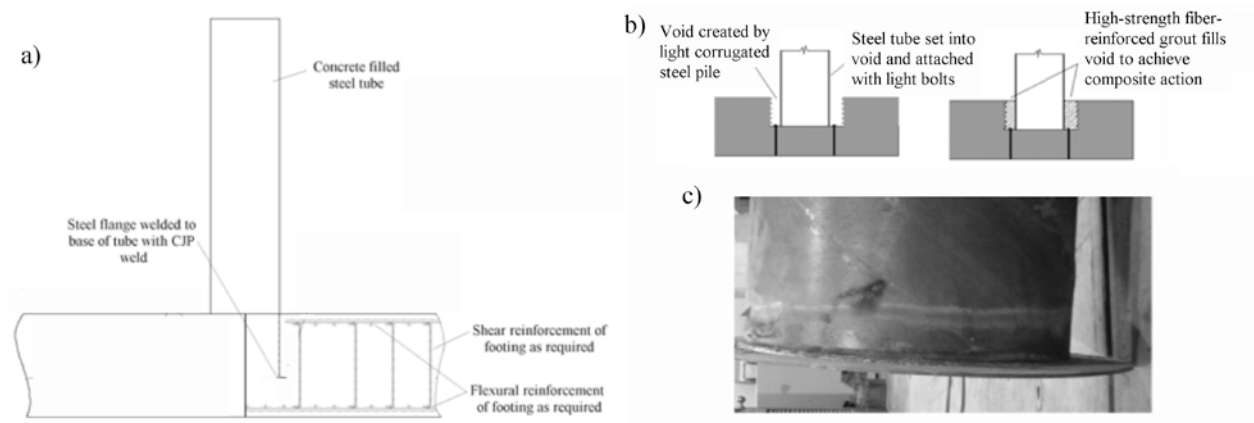

Figure 2-4. Proposed CFT Pier or Column Foundation Connections, a) Embedded connection, b) Recessed connection, c) Welded Annular Ring

The tube is embedded into the foundation in one of two ways as depicted in Fig. 2.5a and 2.5b. The embedded tube is anchored with the annular ring, so sufficient concrete depth is needed to sustain the stresses associate with pullout and push-thru the foundation element. If these are achieved, the tube and the ring primarily contribute to the connection stiffness and resistance. Fig. 2.5a shows a monolithic connection, in which the flange and tube end are embedded directly into the foundation or pile cape with the embedded option. Fig. 2.5b shows

the isolated connection, in which the footing is cast with a recess formed by a corrugated steel pipe. The recess has an inside diameter that is slightly larger than the outside diameter of the annular ring. With this recessed option, the tube is placed in the recess after the foundation concrete has been cast. After placement, the gap between the tube and the corrugated pipe is filled with high-strength low-shrinkage fiber-reinforced grout. For both options, the steel tube is filled with low shrinkage self consolidating concrete to complete the member and connection.

A series of large-scale experiments evaluated the performance of this foundation connection (Kingsley 2005, Williams 2007, Chronister 2008). Figure 2.6 shows the dimensions and geometry of a typical specimen. The embedded depth of the tube, l_e, the shear reinforcement in the foundation, the axial load ratio, and the properties of the steel tube were varied between specimens as shown in Table 2.2, since these were potential design issues and major parameters in the research study.

Table 2.2 Summary of Test Specimens and Results

Spec.	l_e/D	Study Parameter	F_y (MPa)	F_u (MPa)	f'_c (MPa)	Max. Drift	Max. Load (kN)	Failure Mode
1	0.6	Embedded w/light shear reinforcement	520	605	76	8.5%	581	Cone pullout
2	0.6	Embedded w/ significant shear reinforcement	520	605	76	9.5%	599	Cone pullout
3	0.9	Embedded	520	605	69	8.0%	735	Ductile tearing of tube
4	0.6	Recessed	520	605	69	7.8%	618	Partial pullout
5	0.9	Embedded	520	605	78	9.0%	749	Ductile tearing
6	0.75	Recessed	520	605	82	9.6%	770	Ductile tearing
7	0.75	Recessed - punching shear w/225mm depth	520	605	64	NA	3413	Monotonic punching
8	0.75	Recessed - punching shear w/225mm depth	520	605	65	NA	3044	Cyclic punching
9	0.9	Recessed – galvanized	520	605	69	8.5%	770	Ductile tearing
10	0.9	Recessed - galvanized w/near fault cyclic deformation	520	605	67	10.5%	797	Ductile tearing
11	0.9	Recessed - increased axial (2737 kN)	520	605	64	10.4%	743	Ductile tearing
12	0.9	Recessed - Increased axial (3649 kN)	520	605	69	9.5%	788	Ductile tearing

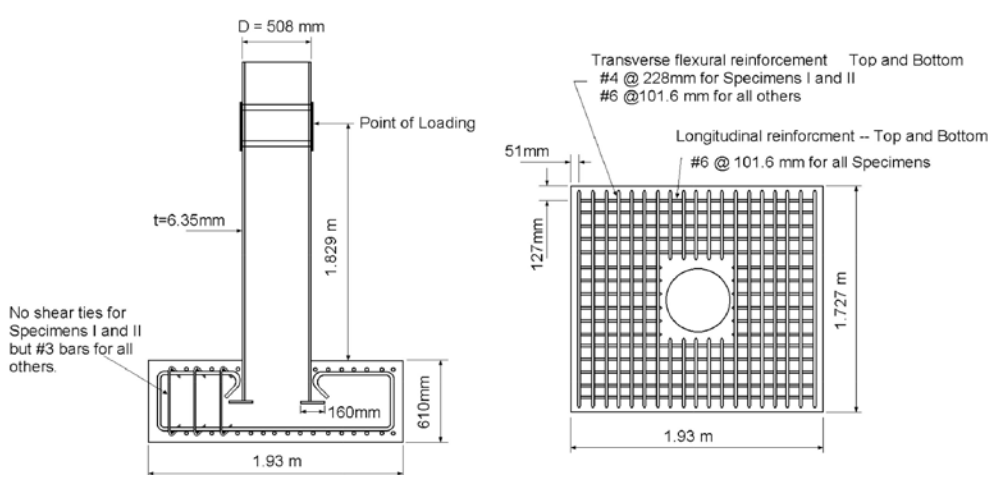

Figure 2-5. Typical Test Specimen

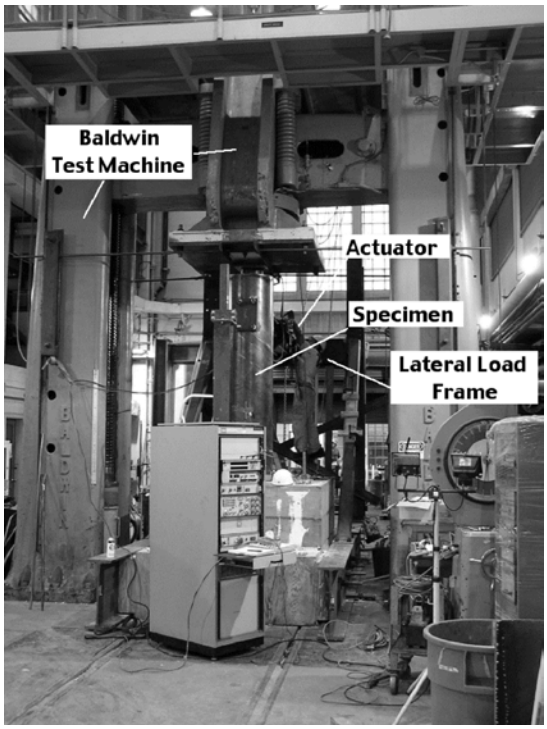

Figure 2-6. Photo of Specimen and Test Setup

Most tests evaluated the connection under axial compression and cyclic lateral load, and the self-reacting test frame was placed under the 2,400 kip Baldwin Universal Testing Machine, as shown in Fig. 2.7. Most specimens had a compressive load of approximately 400 kips, which was approximately 10% of the crushing compressive capacity of the CFT member, P_o, but larger loads were used for a few tests to evaluate punching shear. For a CFT member, the compressive capacity is equal to the crushing capacity,

(Eq. 4)

In the experiments, the compressive load was applied using the Baldwin Test Machine through a dimpled, lubricated Polytetrafluoroethylene (PTFE) sliding surface with a #8 mirror finish stainless steel mating surface. The sliding assembly rested on a spherical bearing to permit end rotation. Therefore, P-δ effects are directly simulated in the test, and the friction is minimized. A 220-kip MTS actuator applied the cyclic lateral loading, and the displacement history was based upon ATC-24 protocol (ATC 1992) or a near fault variation of this cyclic deformation history.

Connections with very shallow embedment, such as Specimen 1, develop relatively poor performance with cone pullout failure as shown in Fig. 2.8. Cracking initiated in the footing at the column-footing interface at very small deformations, and this cracking spread from the column base, parallel and perpendicular to the direction of loading with increasing deformation. This ultimately led to the severe foundation cracking and cone pull out, as shown in Fig. 2.8b. The maximum horizontal load was reached at 2.4% drift and dramatic deterioration of resistance was noted as shown in Fig. 2.8a. The maximum resistance was smaller than the plastic capacity of the composite section but approached the theoretical yield force of the tube.

Most specimens had adequate embedment depth needed to provide excellent ductility and inelastic deformation capacity with virtually no damage to the footing. Specimen III used as an example of this behavior. Very small hairline foundation cracks formed at 0.5% drift, but these foundation cracks remained smaller in width, larger is spacing, and were not widely distributed in comparison to Specimen I. Tensile yielding of the tube of Specimen III was clearly observable at 1.3% drift at a horizontal load of 134 kips. The maximum horizontal load of 165 kips was reached at 2.4% drift. After this drift, it is noted that the shear force decreased, however this decrease was solely a result of the P-δ moments, as shown in Fig. 2.9a. The maximum resistance exceeded the ultimate plastic capacity of the composite CFT member. At 4% drift local buckling of the tube was clearly visible, and ductile tearing initiated at the highly strained region of the buckle at 6% drift. The concrete fill inside the tube at the column base had crushed at this deformation level. The test was terminated at 8% drift due to significant tearing around the perimeter of the steel tube at the local buckled region as shown in Fig. 2.9. The specimen sustained virtually not damage to the footing as can be seen in Fig. 2.9b.

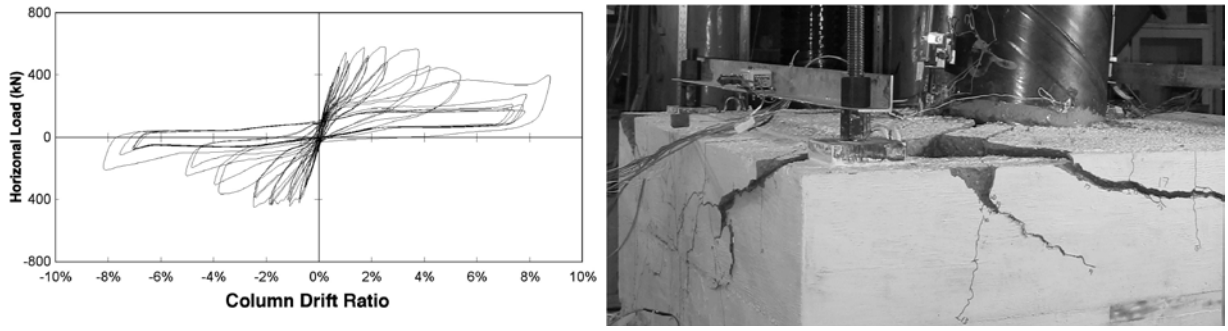

a) b)

Figure 2-7. Specimen-I Performance: a) Force-Deflection Response, b) Photo of Footing Damage at End of the Test

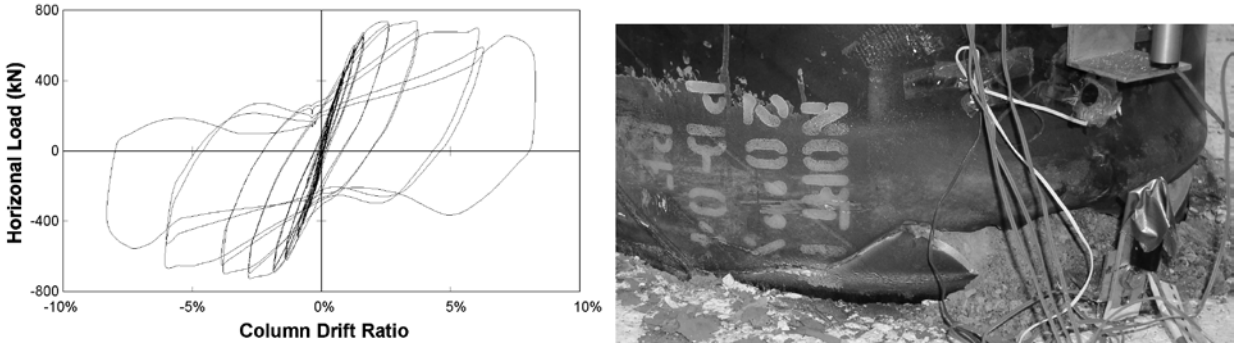

a) b)

Figure 2-8. Specimen-III; a) Force-Deflection Response, b) Ductile Tearing of Tube at the Local Buckle at the End of the Test.

Similar behavior, including the progression of yielding, buckling, and tearing, were noted in other tests. Specimens with inadequate embedment sustained damage to the footing, reduced ductility and inelastic deformation capacity, and deterioration in resistance. Specimens with greater embedment depth developed the full composite resistance and plastic capacity of the CFT member and attained large inelastic deformations prior to connection failure. Local buckling of the thin wall tubes was first observed at 3% to 4% drift, and maximum lateral resistance (including reduction for P-δ effects) occurred at similar drift levels. Degradation in resistance (including P-δ effects) was insignificant until approximately 6% drift. After multiple cycles of severe buckling, deformation tears initiated in the peak of the buckle, and grew around the perimeter of the buckled tube with multiple cycles of increasing deformation. Failure of the tube

was noted at drift levels between 8 and 10.5%. Although similar drift capacities can be achieved with reinforced concrete construction, the seismic performance of CFT columns exceed that of RC components in that at more moderate levels of drift CFT columns sustain damage that does not require post-earthquake repair where RC columns do. Further comparison of the seismic performance of the two systems is provided in Chapter 5.

2.4 ANALYSIS AND EVALUATION OF SIMPLIFIED DESIGN MODELS

The measured resistance values of the 91 circular CFT specimens in the database were compared to the resistance values predicted by the design models shown in Fig. 2.1. The plastic stress distribution method is easier to use and is viewed as providing consistently conservative predictions of resistance (e.g., Marson and Bruneau 2004, Kingsley 2005). As a result, the method was studied in detail.

The moment resistance was computed by applying the measured axial load to the specimen cross section, the measured material properties of the steel and concrete, and the stress distribution illustrated in Fig. 2.1a to determine the bending moment. Figures 2.11a and b show the ratio of measured moment capacity to the predicted moment capacity by the plastic stress distribution method as functions of the axial load ratio (P/P_o) and the local slenderness of the tube, respectively. A ratio greater than 1.0 indicates a conservative prediction.

The mean ratio of measured-to-predicted moment capacity is 1.24 with a standard deviation of 0.18, and there is consistency in the mean and standard deviations for the 3 separate test groups. A few beam-column specimens fall slightly below 1.0, but these specimens all approach the maximum D/t slenderness limit permitted by current design specifications as shown in Fig 2.11b. Further, several of those tests also have large Kl/r values, indicating that their resistance is reduced by column buckling, which must be considered explicitly. Simply applying the plastic stress method for slender components does not meet the code specification. Finally, Fig. 2.11b shows that the AISC local slenderness limit (Eq. 1a) is generally adequate to assure development of the full composite resistance of CFT members, since their full capacity was developed for many CFT members that greatly exceeded the current AISC slenderness limit. This clearly indicates that the ACI and AASHTO D/t slenderness limits are overly conservative for circular CFT.

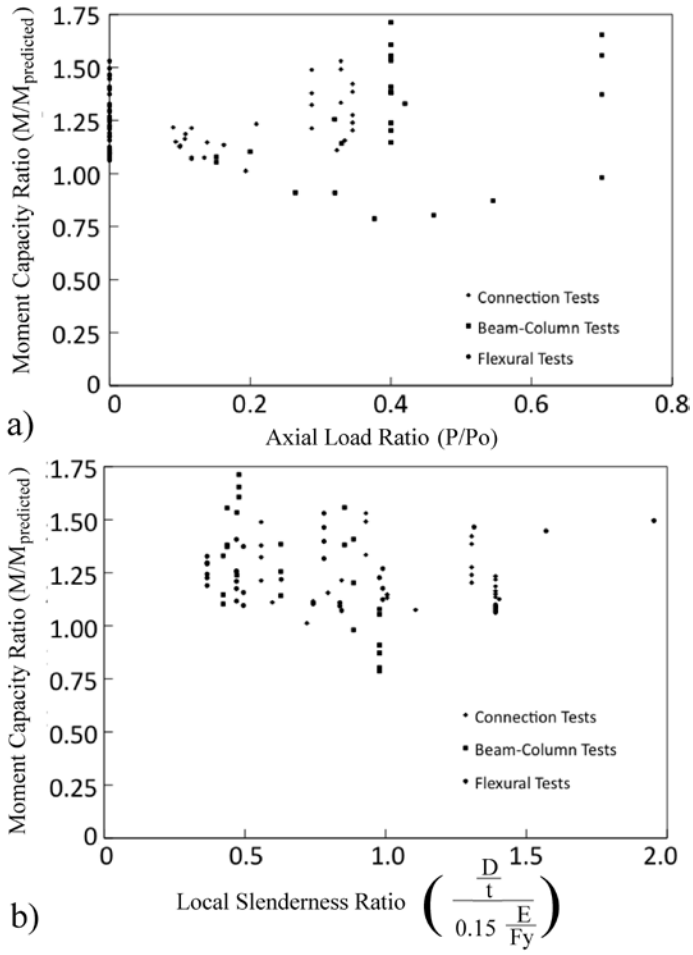

Figure 2-9. Comparison of Measured to Predicted Plastic Stress Distribution Moment Resistance a) As function of $\frac{P}{P_o}$, and b) As a function of $\frac{D}{t}$ of the tube

The ACI and AISC strain-compatibility methods are sectional analysis methods that will be discussed in greater detail in the next section. These analysis methods were significantly less accurate than the plastic stress distribution method, and they were more difficult to use. The mean ratio of the measured-to-predicted moment capacity for the ACI method was 1.65 and the standard deviation was 1.14, and the AISC strain compatibility method had similar variations. The larger standard deviation is caused by the greater scatter in the predictions, since the method slightly overestimated the bending capacity in a few cases, but underestimated the bending capacity by several hundred percent in other cases. The primary reason for the inaccuracy of the ACI strain compatibility method is the 0.003 compressive strain limit. For conventional reinforced concrete, this 0.003 strain limit is provides a lower-bound estimate to spalling of the

concrete cover, but the concrete cover is eliminated with CFT, since all concrete is well confined. The current AASHTO LRFD resistance predictions are even more conservative than the ACI strain-compatibility method.

SIMPLIFIED CLOSED FORM SOLUTION OF PLASTIC STRESS DISTRIBUTION METHOD

The plastic stress distribution method provides a practical solution predicting the resistance of CFT. The method is relatively simple, but it currently involves trial and error assumptions as to the neutral axis location. As a result, a closed-form solution was derived by application of equilibrium of the plastic stress distribution through integration over the cross section, as illustrated in Eq. 4 and Fig. 2.12.

$$r_m = r - \frac{t}{2} \qquad \text{(Eq. 4a)}$$

$$\theta = \sin^{-1}\left(\frac{y}{r_m}\right) \qquad \text{(Eq. 4b)}$$

$$c = r_i \cos\theta \qquad \text{(Eq. 4c)}$$

$$P = F_y t r_m \{(\pi - 2\theta) - (\pi + 2\theta)\} + \frac{0.95 f_c'}{2}\{(\pi - 2\theta) r_i^2 - 2yc\} \qquad \text{(Eq. 4d)}$$

$$M = 0.95 f_c' c\left\{\left(r_i^2 - y^2\right) - \frac{c^2}{3}\right\} + 4 F_y t c \frac{r_m^2}{r_i} \qquad \text{(Eq. 4e)}$$

A positive value of P implies a compressive force, and y and θ are positive with the sign convention shown in Fig. 2.12. The variable y varies between plus and minus r_i, and the P-M curve can be generated by solving the equations for various points over this range.

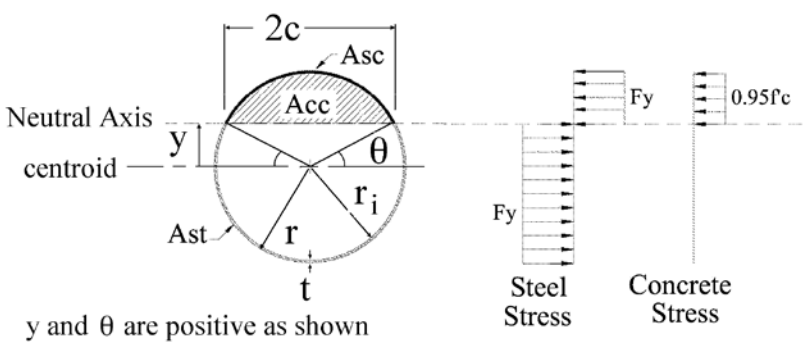

Figure 2-10. Geometry Used for Closed Form Derivation of Stress Distribution Prediction

The interaction curve developed by the plastic stress distribution method does not consider column buckling, and the buckling load must be determined from Eqs. 2a and 2b.

Based upon the effective length of the column, the load effectively truncates the M-P diagram as shown in Fig. 2.2c.

COMPOSITE STIFFNESS

The effective stiffness, EI_{eff}, of circular CFT is also important, because it is used to evaluate deflections, deformations, and buckling capacity Equations 3 show the AISC, ACI, and AASHTO models used to estimate EI_{eff} for CFT. Comparison of these equations shows that the AISC provisions predict a larger value of EI_{eff} than ACI, and AASHTO stiffness is always larger than the AISC stiffness with the difference depending upon the D/t of the tube. Fifty circular CFT tests that provided the force-deflection, moment-curvature, or moment-rotation response data needed to experimentally determine were identified, and the EI_{eff} determined from the experiments were compared to the design models of Eq. 3a through 3d.

The average ratio of the measured to predicted flexural stiffness was 0.57 and 0.95 for flexural tests and 0.87 and 1.36 for combined compression and flexural tests with the AISC and ACI provisions, respectively. This indicates that the ACI provisions provide a relatively good prediction of flexural stiffness for flexural members, but significantly underestimate the stiffness for members with combined bending and compression. The AISC expression overestimates the flexural stiffness but provides increasing accuracy on CFT members with significant compressive axial load. These observations are logical, because beam-columns with increasing axial load engage more of the concrete in compression, which should increase EI_{eff}.

PROPOSED SIMPLIFIED AND IMPROVED STIFFNESS MODEL FOR CFT

All of the current stiffness models can be expressed as:

$$EI_{eff} = E_s I_s + C' E_C I_C \qquad \text{(Eq. 5a)}$$

where C' is a different value but less than 1.0 in each design provision, and it is used to represent the contribution of the concrete fill to the CFT stiffness. The test data shows that C' should be larger for increased compressive load.

Using these results as a guide, the data was revisited to develop a more accurate and representative equation. A number of simple functions were considered, and Eq. 5b was ultimately developed as the best fit to the experimental data:

$$C' = 0.15 + \frac{P}{P_0} + \frac{A_S}{A_S + A_C} < 0.9 \qquad \text{(Eq. 5b)}$$

This expression is more consistently accurate and has a smaller standard deviation than all other current models, and on average it provides a conservative (lower) estimate to the secant stiffness that is achieved in experimental results at 90% of the ultimate load. This conservatism is important, increased stiffness provides increased estimates of buckling load. Figure 2.13 compares the measured stiffness to the stiffness predicted by Equation 5. The ratio is significantly closer to 1.0 than obtained for comparisons of the measured to predicted stiffness by the AISC and ACI equations. The scatter remains significant, but is much smaller than noted with the AISC, ACI, or AASHTO provisions.

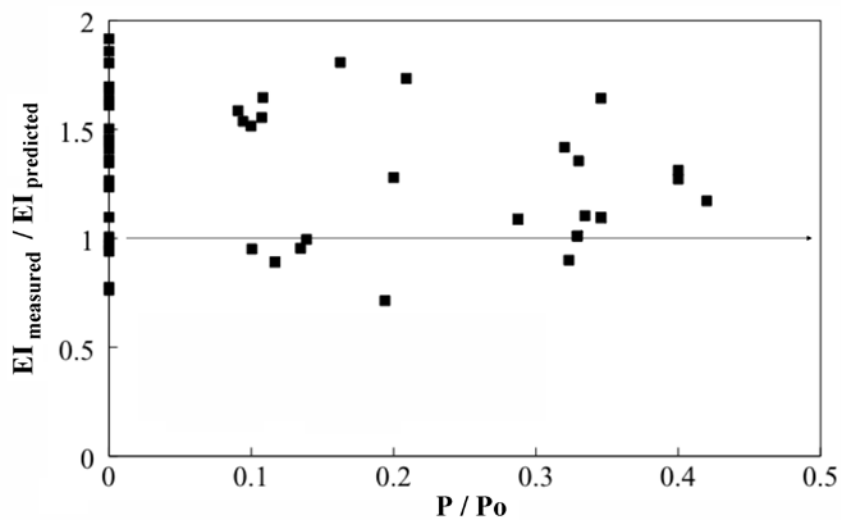

Figure 2-11. Comparison of Proposed Stiffness Models to Measured Stiffness

SECTION AND FIBER-BASED MODELS FOR FLEXURAL STRENGTH

Section and fiber-based cross section analyses models (including the strain compatibility methods) are commonly used for reinforced concrete bridge piers, and these methods were also evaluated. Multiple methods including XSECTION (a cross section developed by Caltrans) were evaluated, but the OpenSees platform was utilized for the bulk of the work, since it clearly duplicated the results from other analytical tools and permitted greater versatility in the analysis (Mazzoni et al. 2005). Sectional analysis methods typically consider the confinement of concrete and strain hardening of steel, which are not directly considered in the plastic stress distribution method. However, the moment resistance is a function of the strain or curvature, and so the flexural resistance defined by these methods requires a realistic and reliable failure limit state, such as the 0.003 in/in compressive strain limit.

To study the effectiveness of the fiber or sectional analysis methods, a wide range of analyses were performed (Bishop 2009) with kinematic strain hardening ratios of the steel between 0.4 and 1.5% along with different models for simulating the confined concrete stress strain response (Thody 2005, Mander et al. 1988, Inai et al. 2004), and different strain, curvature or deformation limits. The Thody model (2005) is based on several specific CFT test results (Kingsley 2005, Williams 2007). The Inai model (2004) was empirically developed from a wider range of past CFT experiments, and the Mander model (1988) is a commonly used model for reinforced concrete with limited applicability to CFT.

Figure 2.14 provides a comparison of the models with the measured moment-curvature response for a typical flexural specimen. The Thody empirical model for CFT provided the best theoretical approximation of the measured behavior for this test, but the Inai model for CFT more consistently predicted the response for most CFT specimens. However, the Inai model does not capture the maximum moment at the measured curvature in the experiments, because it fails to simulate deteriorate resulting from severe local buckling of the CFT specimen. Strength deterioration in CFT is a result of large local buckling of the tube and tube tearing rather than spalling or cracking of the concrete, and local buckling is not captured with sectional analysis methods. The Mander confinement concrete model did not provide a good representation of either the moment-curvature behavior or the increased resistance of CFT members. It frequently predicts early deterioration of resistance because of spalling that cannot occur in CFT members.

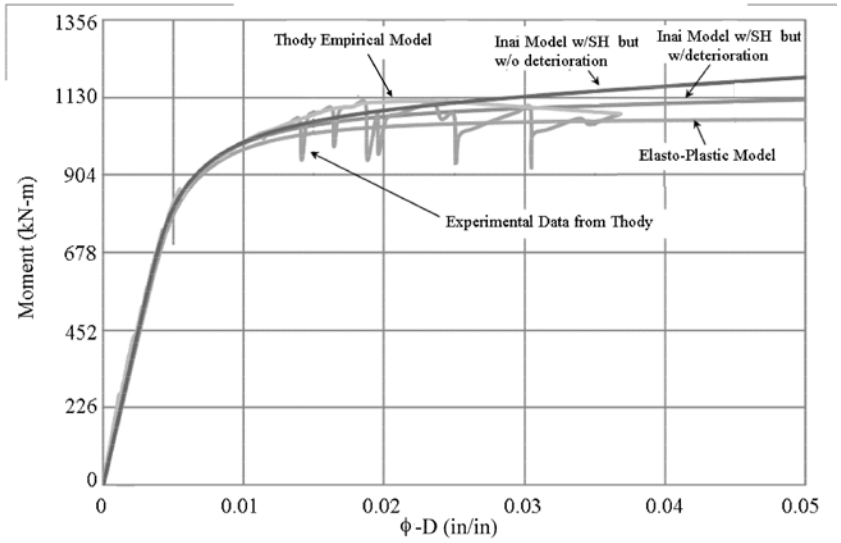

Figure 2-12. Measured vs. Predicted Moment-Curvature Behavior using Different Concrete Models in a Fiber-Based Cross Section Analysis

The maximum resistance predicted with fiber-based cross section analysis depends upon the constitutive model and the limiting strain, curvature or deformation. A wide range of limits including tensile and compressive strain in steel (ε_{st} and ε_{sc}), compressive strain in the concrete (ε_{cc}), curvature (ϕ), dimensionless form of curvature consisting of the product of the curvature and the diameter of the tube (ϕ*D), and combinations of the above were evaluated.

Figure 2.15 illustrates the average dependence of the moment strength ratio on the curvature for all 91 specimens for several of these evaluations with the best available CFT sectional model (the Inai model) with bilinear steel behavior used with (Fig. 2.15a) and without strength deterioration (Fig. 2.15b). The figure shows the mean maximum moment strength ratio as a function of the dimensionless curvature for each of the test setup categories in the three test categories. The figure shows that the accuracy of the predicted maximum resistance improves for larger curvatures, and on average the strength is underestimated by the most accurate sectional analysis method. The Inai model without strength deterioration provides improved accuracy for the predicted resistance (Fig. 2.15b), but the accurate prediction occurred at an average ϕ*D of 0.077. At this large deformation, the flexural capacity was predicted within 3%, with a standard deviation of 0.14, but no single test specimen in the data base came close to actually achieving this large ϕ*D limit. While the predicted resistance is accurate, the deformation behavior

associated with this prediction is totally unrealistic. This was a common failing of all sectional analysis methods, and Inai model perform consistently better than other methods. Loss of compressive capacity of CFT occurs only after severe local buckling, but sectional analysis methods cannot capture local buckling.

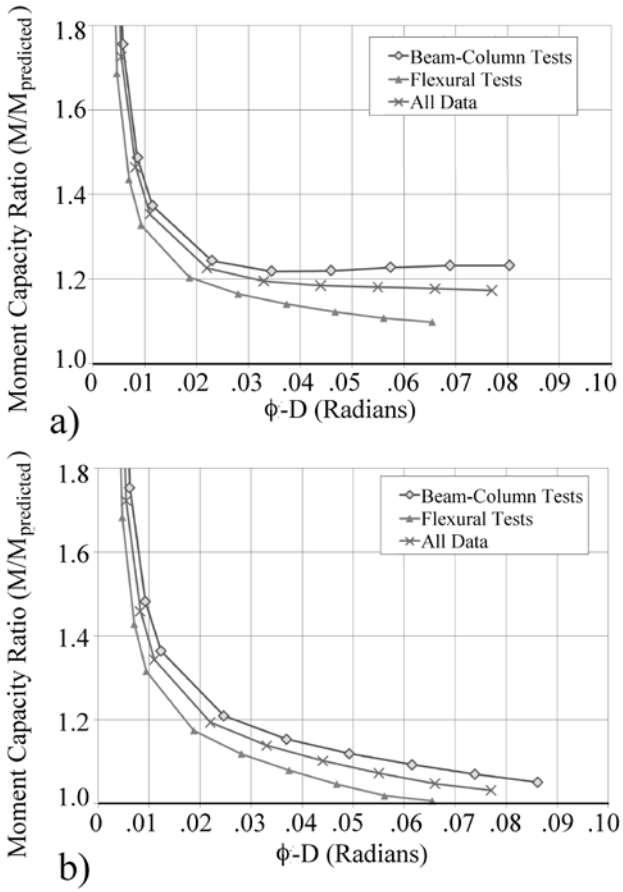

Figure 2-13. Evaluation of Fiber-Based Cross Section Model Moment Prediction using Inai Concrete Constitutive Model; a) with Deterioration, and b) without Strength Deterioration

The Inai model without strength deterioration is the most accurate cross sectional analysis model; Table 2.3 shows the relative accuracy of various failure limits with this model. The 0.003 compressive strain limit for the concrete fill greatly underestimates the strength of circular CFT. The experiments indicate that buckling and tearing of the steel tube contributed to strength deterioration, therefore strains in the steel tube were used a potential limit states. A compressive steel strain of $5\varepsilon_y$ and a tensile steel strain of $10\varepsilon_y$ resulted in a mean strength ratio of 1.12 and 1.13, respectively with the same standard deviations of 0.15. Similar results were found using

ϕ*D of 0.03 (mean ratio of 1.12 and standard deviation of 0.14). However, none of these limits provide good comparison with the strains coinciding with actual deterioration of resistance in the experiments

Table 2.3 Comparison of Calculated Moment Strength Ratios for Fiber-Based Sectional Analysis

Limit State	Measured-to-Predicted Flexural Strength Ratio			
	Mean	Min	Max	Std. Dev.
ϕ*D = 0.03	1.12	0.72	1.55	0.14
ε_{cc} = 0.003 mm/mm	1.64	0.97	9.18	1.17
$\varepsilon_{sc}/\varepsilon_y$ – 5	1.12	0.76	1.55	0.15
$\varepsilon_{st}/\varepsilon_y$ = 10	1.13	0.68	1.48	0.15

2.5 CONTINUUM (FEM) ANALYSIS METHODS

Finite element analyses of selected experiments were conducted. While sectional analysis did not provide a good prediction of the experimental behavior, nonlinear continuum analysis models provided very good correlation but at great cost in time and complexity (Moon et al. 2010). The analyses were conducted using the analysis program ABAQUS (2005). The 4-node shell element with reduced integration (S4R) and 8-node solid element (C3D8R) were used to construct the finite element model for CFT shown in Fig. 2.16. Critical modeling aspects of CFT include concrete confinement and bond stress between the steel shell and concrete fill, and these issues were addressed with GAP elements simulating the interface between steel tube and concrete infill. These GAP elements:

- Permit separation between the steel and concrete surfaces under tensile stress,
- Prevent penetration of the concrete into the steel, and
- Provide bond stress between the concrete by combining the confining contact stress with a coefficient friction to develop shear stresses at the interfaces.

CFT bond stress is primarily transferred through friction (Roeder et al. 2010). The GAP element available in ABAQUS is ideal to simulate the transfer mechanism. Parametric analyses were conducted to evaluate variation in the coefficient of friction. Evaluation of the experimental result indicated that a coefficient of friction of 0.47 provided the most accurate estimate over the full range of CFT performance.

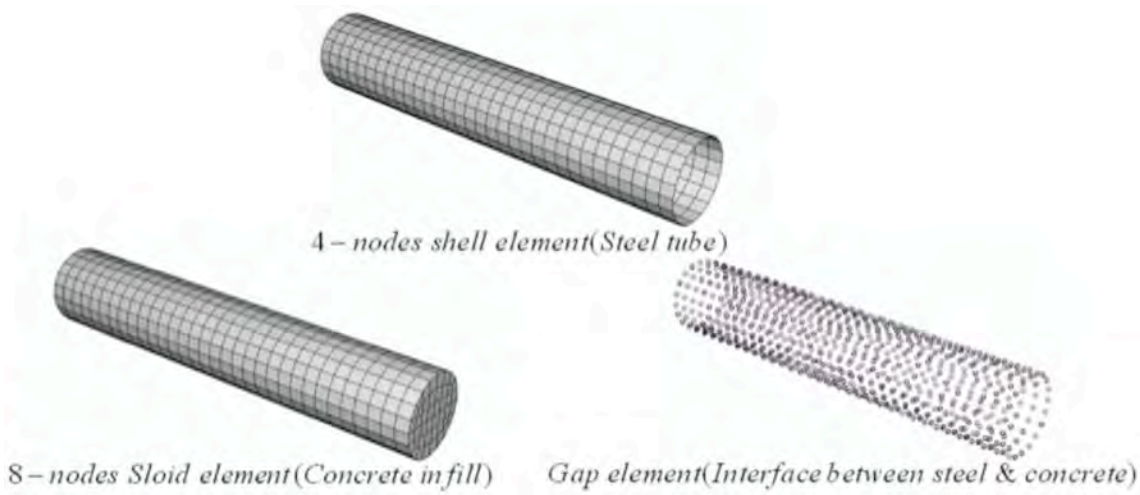

Figure 2-14. ABAQUS Finite Element Mesh and Model

The constitutive models were calibrated to the measured properties for each CFT experiment. The ABAQUS concrete damaged plasticity model was employed, and the tri-linear stress-strain relationship with isotropic strain hardening was employed for steel. The concrete damaged plasticity model results in a non-symmetric material stiffness matrix, because the nonlinear behavior does not use an associated flow rule. The stress-strain relationship (see Fig. 2.17a) for unconfined concrete model was used, because the confinement is generated by the compressive stress transferred through the gap element. This provides a more rational and realistic measure of true confinement. The dilation angle of the material, ψ, is an important parameter with the concrete damaged plasticity model, and ψ is selected as 20° based upon calibration analyses performed in the study.

An example of the steel model is illustrated in Fig. 2.17b. The solution method was selected to obtain an acceptable rate of convergence, and the STABILIZE option provided by ABAQUS with the asymmetric matrix storage and solution scheme was employed.

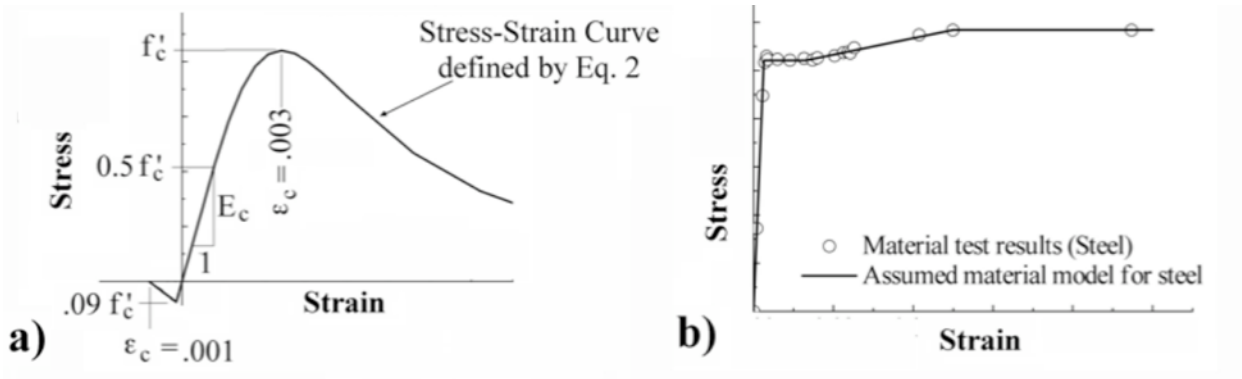

Figure 2-15. Typical Material Models for Analysis; a) Concrete, b) Steel

A mesh refinement study was completed to assure convergence of the nonlinear analyses. Analyses with a finite element mesh scaled to have 8, 12, 16 and 20 elements around the perimeter of the tube were performed, and changes were insignificant between the 16 and 20 element mesh. As a result, a 20-element mesh was selected for this analytical study.

Theoretical predictions of the nonlinear finite element models were compared to test specimens under axial load, shear and flexure, and combined axial and bending. Figure 2.18 shows typical comparisons of the computed behavior to the measured axially loaded experimental behavior. Figure 2.19 shows typical comparison of the continuum analysis for tests with fixed axial load is fixed, monotonically increasing bending moment associated and P-δ moments. The continuum model provides conservative but reasonably accurate estimates of the maximum resistance in all cases. It captures deterioration of resistance, because the model accurately simulates both global and local buckling, and it provides a realistic estimate of the strain or deformation at the maximum load capacity.

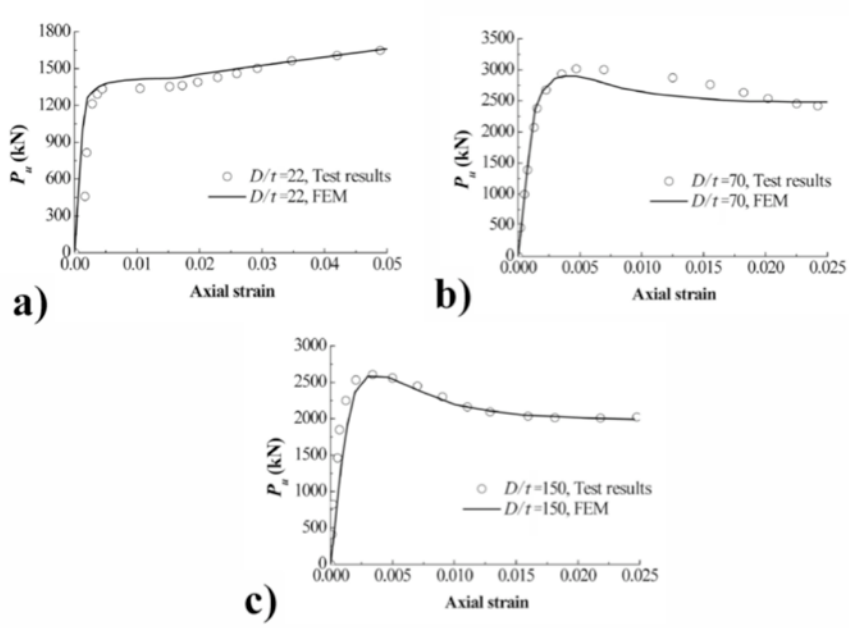

Figure 2-16. Comparison with Compression Test Results of Schneider (1998); (a) D/t=22; (b) D/t =70; and (c) D/t =150

These evaluations were completed for many of the 91 specimens included in the database. The continuum finite element model was documented as very accurate and reliable model for CFT. The ABAQUS continuum finite element model (FEM) on average slightly underestimated the moment capacity of the tubes for all conditions, but the estimate was more accurate than the plastic stress distribution method. Earlier it was noted that the plastic stress distribution method underestimated the maximum flexural resistance of beam-columns by an average of approximately 24%. Strain compatibility and section or fiber methods resulted in larger average errors and much larger scatter in the predicted results. The FEM analysis also results in conservative predictions of the flexural capacity of beam-columns with and without axial load, but the error and scatter are smaller than that resulting from the plastic stress distribution method. The plastic stress distribution method underestimates the capacity predicted by the continuum finite element analysis by an average of approximately 10.4%. Therefore, the continuum model underestimated the measured flexural capacity by an average of approximately 12.3%.

The FEM accurately predicted the initiation of local buckling in the tube, and it accurately predicted crack development in the concrete within the tube. The accuracy was

verified by comparison with experimental results for multiple specimens. Figure 2.20 shows the predicted concrete crushing cracking and the observed concrete damage in one specimen. The FEM analysis illustrates these damaged areas by the inability to transfer stress through the crushed and cracked zone. The continuum model also showed the deterioration of resistance noted in the test specimens after severe buckling occurred. Finally, the ABAQUS analysis provided a basis for estimating the ultimate failure deformation of CFT elements, but the comparison with experimental results was clearly much weaker for this case. While the continuum analysis is accurate, it is very costly in time and computation and is not suitable for most typical bridge foundation projects. Hence, the plastic stress distribution method offers great attraction.

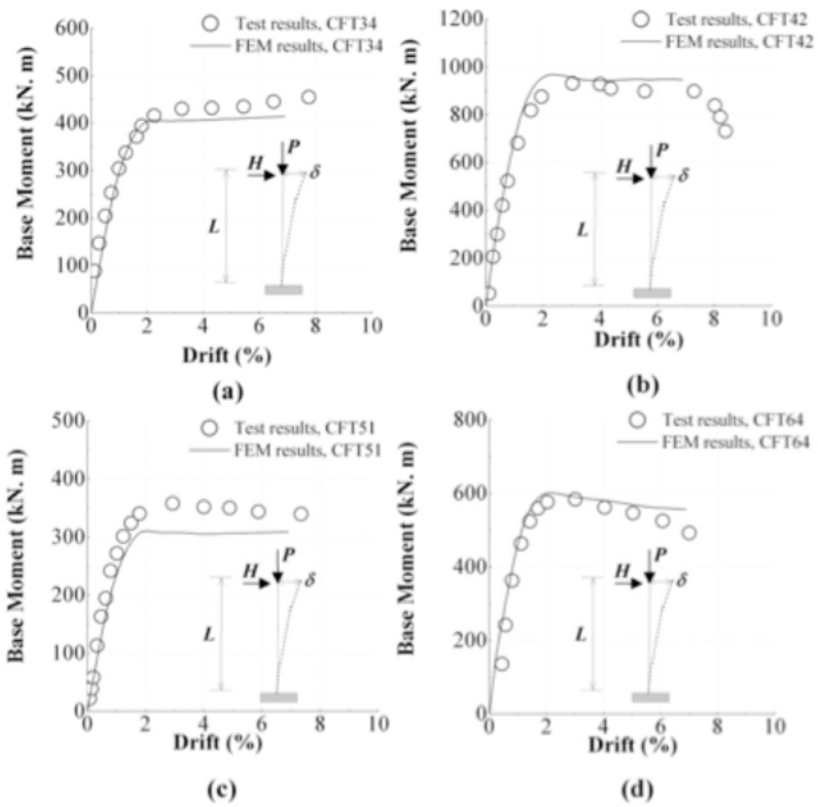

Figure 2-17. Verification of the FE Model for CFT under Combined Loading (Tests by Marson and Bruneau (2004)

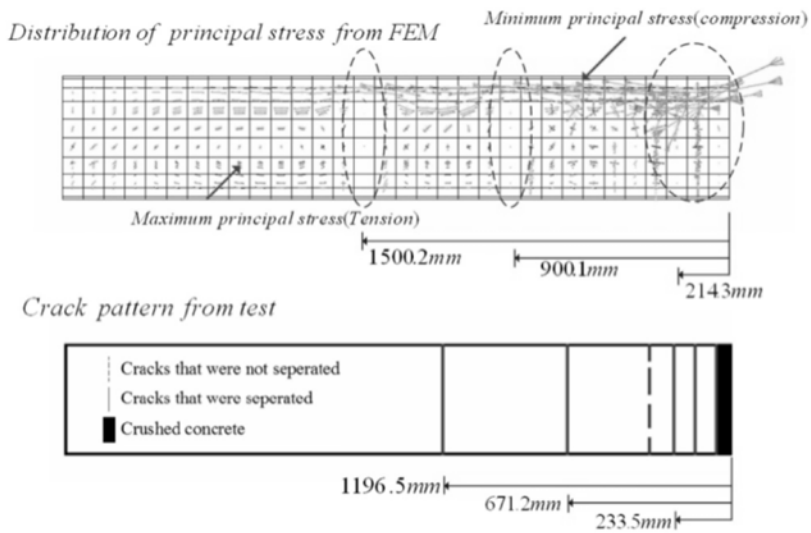

Figure 2-18. Verification of Crack Development Predictions

Chapter 3

Experimental Program

CFT construction represents a practical and efficient construction method for bridge piers and columns. However, robust connections are required for structural integrity especially under extreme loading. This study focused on the pier column-to-foundation connection, which is critical in ensuring good system performance.

Chapter 2 summarized a simple CFT column-to-foundation connection. The study focused on high strength materials. However, the connection can be adopted to use with conventional material strengths, which is the focus of the current study. The connection consists of a flange or annular ring welded to the base of the tube and embedded into the foundation. Two options are available for the embedded connection. The tube may be directly embedded or a recessed, grouted connection detail, which permits placement of the tube after the concrete footing is cast. In this prior research, cross-sectionally slender (D/t = 80) spiral welded tube manufactured using a high-strength (480 MPa or 70 ksi nominal yield), vanadium-alloy steel was used, and the tube was filled with a low-shrinkage, self-consolidating, high-strength (8 ksi (55 MPa) and greater) concrete. The tube diameter and wall thickness were 500 mm and 6.4 mm (20 and 0.25 inches), respectively. The tube slenderness and yield strength are larger than currently permitted by the current design provisions.

Twelve moderately large-scale CFT foundation connections were tested for a range of different connection design details and loading conditions to evaluate the two connection options. The embedment depths varied between 300 and 450 mm (12 and 18 inches or 0.6D and 0.9D). Specimen with the short (0.6D) embedment depths had significant foundation damage with cone pullout failures. Specimens with more significant embedment depth 0.75D to 0.9D developed the full composite resistance of the CFT member and attained large inelastic deformations prior to ductile connection failure. Local buckling of the thin wall tubes was typically visible at drift levels of 3% to 4%. The maximum lateral resistance of the connection (included reduction for P-δ effects) occurred at drift levels slightly smaller that the level where buckling was observed. However, the degradation in resistance was insignificant until a

deformation level of approximately 6% drift. After multiple cycles of severe buckling deformation tears initiated in the peak of the buckle, and this tear initiation normally occurred at drift levels larger than 6%. The tear grew around the perimeter of the buckled tube with multiple cycles of increasing deformation, and ultimate failure of the tube was noted at drift levels between 8 and 10.5%. These drift levels at failure are significantly larger than those observed from similar size reinforced concrete piers and pier-foundation connections of similar size and geometry.

The footing or pile caps were reinforced to simulate typical CALTRANS seismic design standards. Shear reinforcement was varied in these shallow embedded tests, but the specimen without any shear reinforcement and lighter flexural reinforcement had similar failure modes and deformation capacity and only slightly smaller resistance than the specimen with significant amounts of vertical shear reinforcement.

The test results indicate that the proposed annular-ring embedded connection is effective and practical. Specimens with the longer embedment depth are capable of achieving drift capacities far in excess of the maximum seismic design drifts without degradation of the system and minimal damage to the footing. Therefore, this connection is an appropriate detail for high seismic zones and other extreme loading conditions.

However, the prior research was a limited study that did not consider all parameters that affect the CFT foundation connection performance. In particular, the prior work utilized only one tube size where the tube was manufactured by spiral welding with only one grade of high strength steel. Bridge engineers commonly use 345 MPa (50 ksi) steel, and steel tubes may be manufactured by other methods including straight seam welding. Bridge piers have large diameter, and effect of changes in the diameter of the tube and D/t ratio of the tube require investigation. The embedment depth of the connection is clearly an important design consideration since deeper embedment results in ductile performance of the CFT pier, while overly shallow embedment results in dramatic brittle failures within the footing. As a result, the research must define appropriate limits for the embedment depth to insure good inelastic performance of the CFT pier and pier-to-foundation connection without requiring excessive

embedment depth. This embedment is likely to be a function of the diameter and thickness of the steel tube, the yield stress and tensile strength of the steel, and the concrete strength. Further, the axial load ratio and the deformation of the footing can influence the force-transfer mechanism and resulting damage pattern. Experimental and analytical research also is needed to develop design expressions for CFT columns and their foundation connections. This CALTRANS research program was initiated to address these questions; to define the performance of the CFT pier-to-foundation connection with both the embedded and grouted connection design options; and to develop rational design procedures for insuring development of the full design criteria for the connection including the relationship between the D/t ratio, the steel strength (F_y) and the required embedment depth ratio, l_e/D.

The research includes both experimental and analytical research and uses and builds on the prior research summarized in Chapter 2.

3.1. **TEST MATRIX**

Seven large-scale connection experiments were performed as part of this research study. Table 3-1 summarizes the seven (7) tests. The test specimens were similar to those illustrated in Figs. 2-9 and 2-10. The test series was develop to study specific objectives including:

- The type of tube, including straight seam and spiral weld.
- Embedment depth
- Connection type, monolithic or grouted
  Column diameter
- Column diameter (D) to steel tube thickness (t) ratio

Specimens C-1 and C-2 had identical specimen dimensions to Specimens C-4 and C-3. Specimens C-1 and C-2 were fabricated as straight seam tubes of API 5LB PSL1 steel with approximately 345 MPa (50 ksi) tensile yield strength, while Specimens C-3 and C-4 used ASTM A1018-07 SS steel with similar yield strength. Comparison of these tests demonstrate the differences in behavior expected with straight seam and spirally welded tubes, and comparison to

the prior test program demonstrates the effect of material properties on the CFT and foundation connection. The yield stress for the first four specimens was similar, but Specimens C-1 and C-2 had somewhat smaller Charpy V-Notch (CVN) toughness (86 ft-lbs vs 74 ft-lbs at room temperature) than C-3 and C-4. However, the CVN toughness exceeded 20 ft-lbs at -20^{0}F for all of the prior and CALTRANS tubes.

Specimens 3, 5, and 9 of the prior research were embedded connections with similar embedment depths to that used for Specimens C-1 and C-4. Specimen 6 of the prior research was a grouted specimen with similar embedment as used for specimens C-2 and C-3. Thus comparison of these specimens with the prior tests permit direct comparison and evaluation of the effect of different steel yield stress and tube manufacturing methods on the CFT connection and member performance.

Table 3.1 Test Matrix

Specimen	Information	l_e/D	Test Date	Steel		Concrete Compressive Strength (ksi)		Grout Compressive Strength (ksi)
				Fy (ksi)	Fu (ksi)	Footing	Column	Grouted Connection
CT-1	20"x0.25" Straight Seam	0.8	9/10/2009	49	60	11	8.7	n/a
CT-2	20"x0.25" Straight Seam	0.775	10/29/2009			11.4	9.3	10.5
CT-3	20"x0.25" Spiral Weld	0.775	01/04/2010	51	78	9.3	7.7	7.1
CT-4	20"x0.25" Spiral Weld	0.8	01/14/2010			10.8	8.6	n/a
CT-5	20"x0.25" Spiral Weld	0.7	06/11/2010			11.6	9.8	9
CT-6	20"x0.25" Spiral Weld	0.6	07/01/2010			11.7	10.1	9.6
CT-7	30"x0.25" Spiral Weld	0.6	06/25 to 07/08/2011	54*	76*	11.1	8.5	10.6
* From Mill Certifications								

Embedment depth is a critical design parameter and is in some ways analogous to the development length for an anchored connection in a reinforced concrete bridge column. A primary goal of this research was to establish limiting values for the embedment depth needed to

assure good performance of the CFT pier and connection. Specimens C-3, C-5 and C-6 were grouted connections with the same spirally welded tube steel (although higher than the prior specimens), but they have varied embedment depth to better evaluate the effect of this design parameter on connection performance. They are also directly comparable to several prior specimens (Specimens 4, 6, and 9) for evaluation of the relationship between material properties and the embedment depth.

A critical aspect of the specimen response is the diameter and the D/t ratio. The final specimen is unique in that it is one of the largest CFT diameters tested to date with a large D/t ratio. Where Specimens C-1 through C-6 and all prior specimens were 400 mm by 6.4 mm (20in by 0.25in) tubes, and Specimen C-7 used a 750 mm by 6.4 mm (30 in by 0.25in) tube with spiral welds to evaluate the performance of larger diameter specimens with larger D/t ratios.

3.2. **SPECIMEN LAYOUT AND DESIGN**

The design and layout for Specimens C-1 through C-7 was that used for the prior tests summarized in Chapter 2. The footing for Specimens C-1 through C-6 had the same basic dimensions as used for the prior tests and shown in Fig. 2-10. The reinforcement and dimensions of the footing are shown in Fig. 3-1a, and it can be seen that the dimensions and reinforcement of the footing are nearly identical to the earlier specimens. Specimen C-7 had a considerably larger CFT pier column, and as a result, a somewhat larger footing with greater reinforcement was required as shown in Fig. 3-1b. It should be noted that the footing of the specimens was constrained by the dimensions of the test frame, while developing the required overturning of the test specimen and without interfering with punching shear and cone pullout.

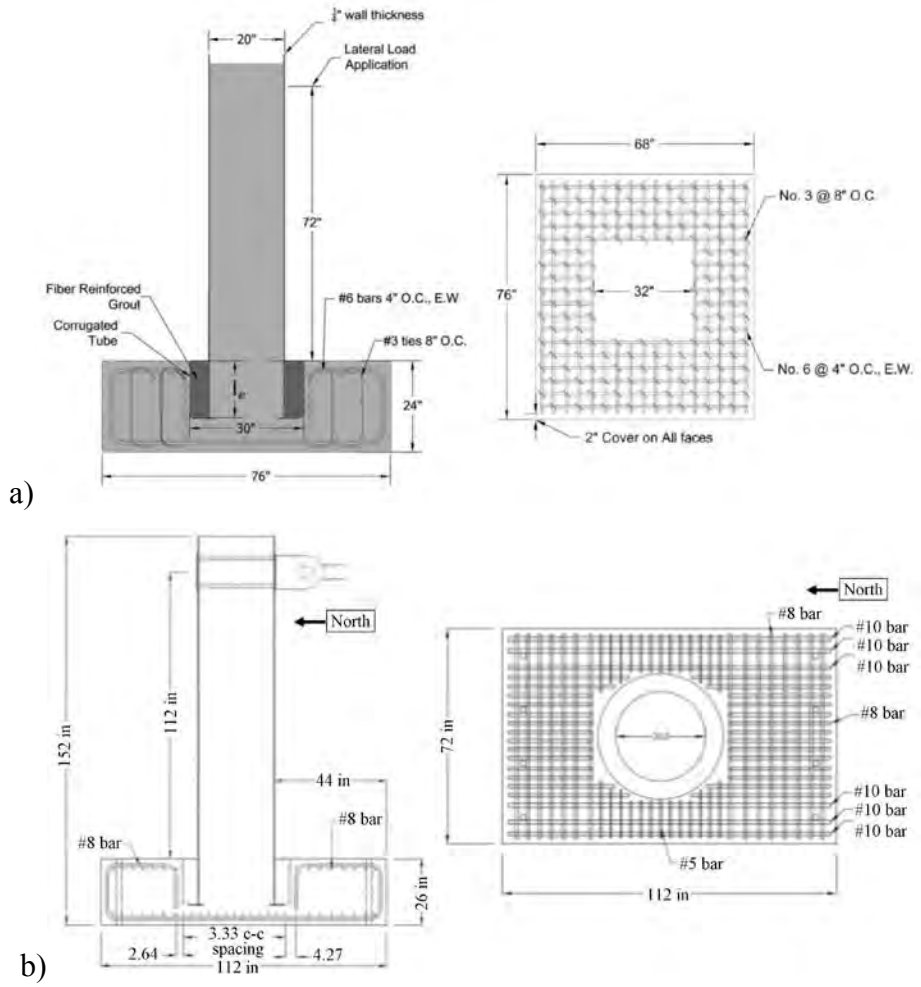

Figure 3-1. Geometry and Footing Reinforcement; a) Specimens C-1 to C-6, b) Specimen C-7

3.3. **EXPERIMENTAL SETUP**

The test setup also utilized the basic test apparatus developed in the prior research study, which is illustrated in Fig. 2-9. However, significant frame deformation was noted in the early stages of the prior test program. These frame deformations limited the maximum deformations that could be applied to the test specimen, and diagonal braces were added to stiffen the frame for Specimens C-1 through C-6 as shown in Fig. 3-2a. Specimen C-7 was stiffer and stronger than all other specimens, and the lateral loads were applied higher on the load frame. Therefore further stiffening of the test frame was applied as shown in the photo of the test setup in Fig. 3-2b.

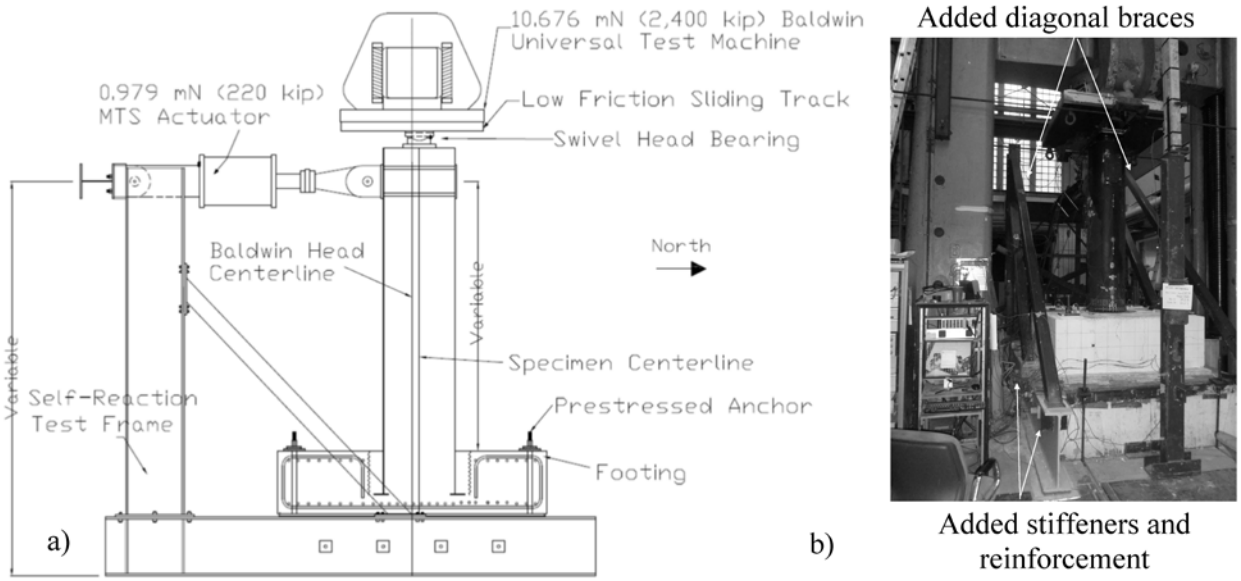

Figure 3-2. Test Setup: a) Initial stiffened setup and b) Added braces to test setup for Specimen C-7

The rig was centered underneath a Baldwin Universal Testing machine with a compressive capacity of 10.67 MN (2400 kips). Each specimen was leveled, and grouted into place with Hydrostone, and the specimen was anchored and post-tensioned to the base of the test apparatus with 4-1 $^1/_4$ inch Williams Form Engineering All-Thread high-strength steel bars post-tensioned to 534 kN (120 kips) for Specimens C-1 through C-6, but 8 post-tensioned bars were needed for Specimen C-7 because of its higher strength and larger lateral loads. These anchor rods were placed at a position to minimize confinement of the concrete or providing additional resistance to the foundation in the area where cone pullout failure of the foundation could occur.

The actuator was clamped to the CFT column by a pair of machined blocks, which conformed to the outside diameter of the tube, and also were pretensioned to the tube by 4-1 $^1/_4$" Williams All Thread bars Williams to prevent all slip and movement during loading. The actuator had a pin swivel connection at each end, to prevent development of moment in the actuator or the specimen.

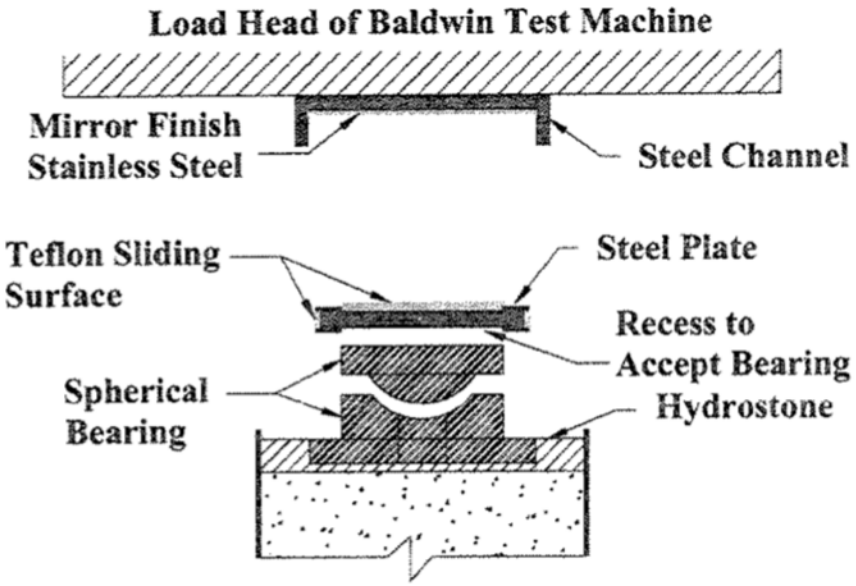

Figure 3-3. Spherical Bearing and Low Friction Sliding Surface

Due to the large lateral movement and high axial loads at the top of the column, special attention was paid to the bearing surface between the Baldwin crosshead and the column as shown in Figs. 3-2a and 3-3. A spherical bearing rested on a bearing plate, which was grouted to the concrete of the top of the column to permit uniform distribution of lateral and gravity loads, and minimize transfer of moments into the UTM crosshead and the top of the column. Gravity loads were applied through the spherical bearing to the concrete only, and these gravity loads were distributed to the steel tube through bond stress required to develop composite action. A guided low-friction sliding surface rested on the spherical bearing as illustrated in Fig. 3-3. The low-friction sliding surface was guided to permit movement only in the direction of actuator movement and to assure stability of the column against out-of-plane effects. The low-friction sliding surface employed a thin sheet of dimpled lubricated Polytetrafluoroethylene (PTFE), which was epoxied to the top and sides of a bearing plate that rested on the spherical bearing. A channel was fixed to the center of the Baldwin crosshead, and served as directional guide for the PTFE sliding surface. A #8 mirror finish stainless steel was placed inside the channel on all sides to serve as a mating surface to the PTFE. A silicone lubricant was placed in dimples on the PTFE surfaces to assure minimal friction of the low friction surface. Research (Campbell and

Kong 1988) has shown that this combination will have a coefficient of friction that is well below 0.01 (Cambell & Kong, 1988).

For most specimens the applied gravity load was 10% of the gross crush capacity P_o (A_sF_y+0.95$A_cf'_c$) of the column. However this percentage was reduced to 5% for Specimen C-7 in view of the larger size of the specimen, and the need to assure that the actuator had adequate lateral load capacity to fully evaluate the specimen. The axial load was applied before the horizontal loading protocol began and was held constant for the duration of the experiment. The horizontal load was displacement controlled using an internal linear variable differential transducer (LVDT) in the actuator. The lateral load protocol used was based on the ATC-24 protocol (ATC 1992), and was directly comparable to the deformation histories used in the previous tests described in Chapter 2. The low amplitude cycles were based on the yield displacement of the tube. Post yield cycles were applied with increasing amplitude with repeated cycles to evaluate deterioration of stiffness and resistance as required in the ATC protocol. The protocol used for testing Specimens C-1 through C-6 is shown in Fig. 3.4. The protocol for Specimen C-7 was scaled to account for the larger specimen size. It should be noted that the figure provides the target deformation of the specimen. However, the test is displacement controlled through the internal LVDT of the actuator. Elastic deformations of the actuator and the test rig itself may be quite significant, and these deformations are also a part of the actuator LVDT measurement. As a result, the actual deformation applied in each cycle included the target deformation plus the predicted deformation of the rig and the actuator. The test specimens had varying stiffness and resistance, and so the actual applied specimen deformation for each cycle varies slightly from test to test. The lateral load was oriented in the north-south direction of laboratory, and the south force and deformation were considered to be positive.

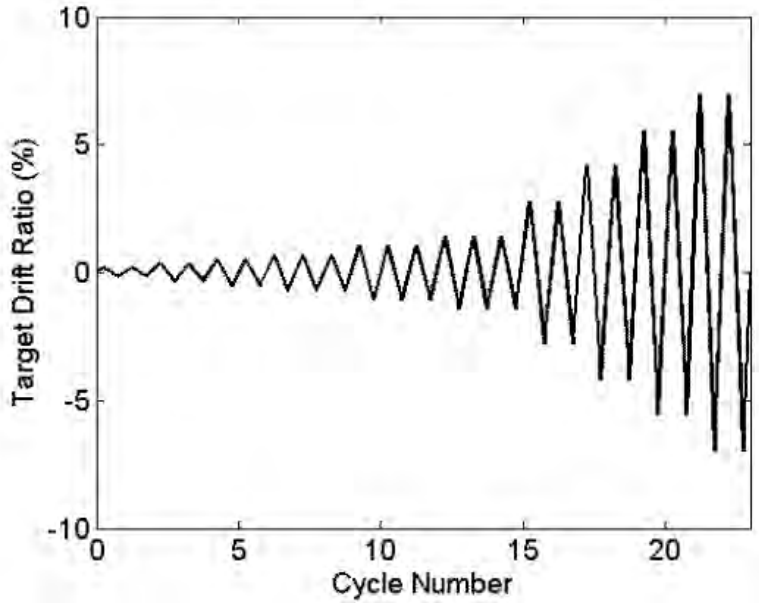

Figure 3-4. Typical Lateral Deformation Test Protocol

The test setup directly applied P-δ moments to the specimen. These effects could be directly measured, and no correction to the data was required for these geometric effects.

3.4. **INSTRUMENTATION**

Extensive instrumentation was applied to all specimens, with some improvement in instrumentation as knowledge was gained during testing. The instruments were electronically recorded by a computer controlled data acquisition system. Most importantly, a new OPTOTRAK optical acquisition system was purchased midway through the research program. This system allowed the monitoring of local deformation mechanisms, including buckling as well as rotations, in a manner that is more accurate than conventional instrumentation.

The applied gravity and lateral loads were directly measured by load cells, which were calibrated prior to testing for all tests. Strain gauges were attached to all specimens as illustrated in Fig. 3-5, and they were used primarily to measure elastic strains in the steel tube for evaluation of elastic curvature, elastic bending moments, and the plastic strain distribution in the critical regions of the embedded depth. In addition, strain gauges were attached to the rebar in the footing of Specimen C-7 as shown in Fig. 3-6 to measure the distribution of stress and strain

in the footing and the participation of various reinforcing bars in development of the connection resistance.

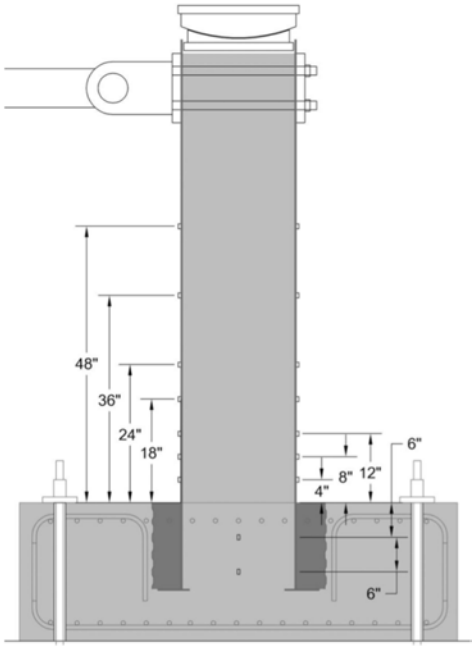

Figure 3-5. Typical Strain Gauge Placement

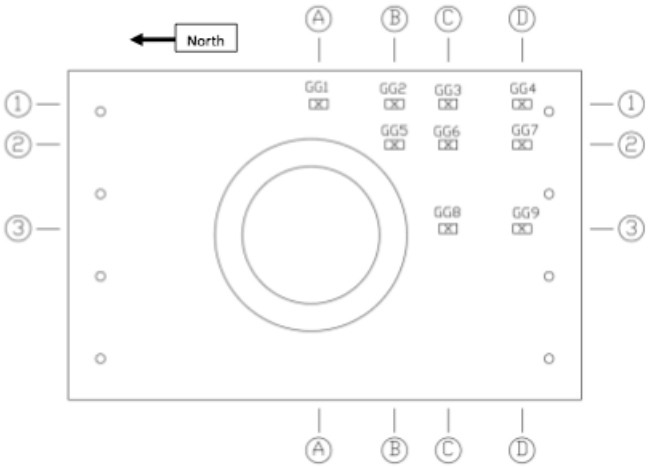

Figure 3-6. Strain Gauge Placement on Footing Reinforcement of Specimen C-7

Displacements and movements were measured by LVDTs, string potentiometers, and short stroke Duncan potentiometers. String potentiometers have a large movement range

(typically 10 to 20 inches) and they were used to measure the actual top displacement of the tube was measured with a string potentiometer as shown in Fig. 3-7a, and horizontal displacements of the tube at 6 additional locations as illustrated in Fig. 3-7b. These later 6 measurements were important in the interpretation of curvature data developed with the LVDTs, as illustrated in Fig. 3-7b. Small stroke Duncan potentiometers were placed at locations were small movements were expected as illustrated in Fig. 3-7a. In particular they measured any slip or uplift of the specimen and the test rig.

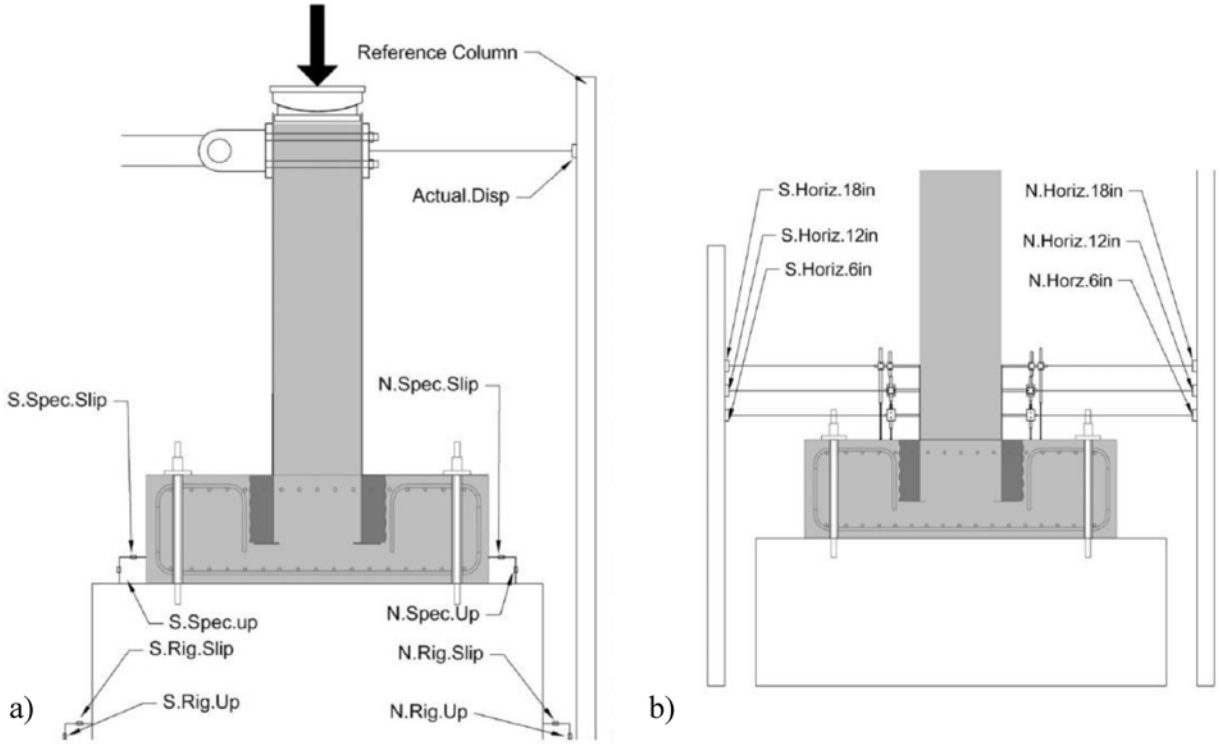

Figure 3-7. Typical Potentiometer Locations; a) Global response, b) Rotation and Curvature

Determination of the distribution of inelastic deformation of the tube and the connection and the inelastic elongation and rotation were primary measurements for all test specimens. For Specimens C-1 through C-4, 8 LVDTs were used in pairs to measure these local behaviors as illustrated in Fig. 3-7b and more clearly shown in Fig. 3-8. These LVDTs experience large geometric changes at large deflections of the CFT pier column, and hence geometric corrections

are required to address the large geometry change issues. The horizontal string potentiometers also illustrated in Fig. 3-7b were used to aid in that data correction.

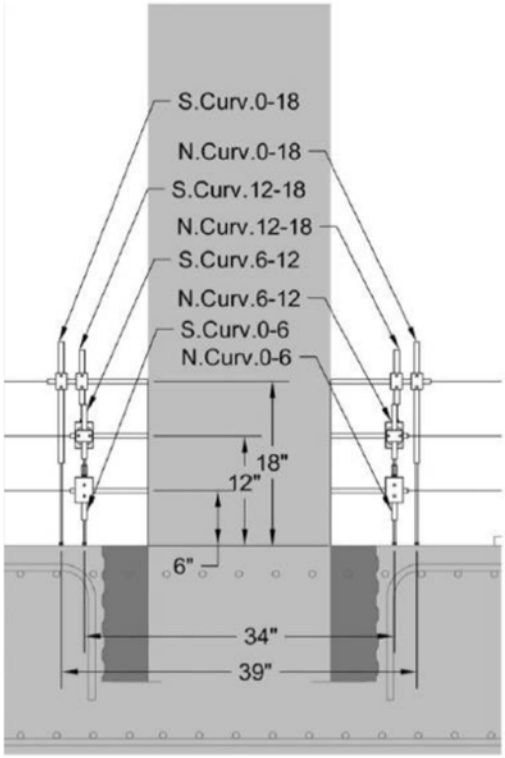

Figure 3-8. Typical LVDT Placement

LVDTs normally provide higher resolution measurements and greater accuracy than potentiometers, but the large geometric changes during testing, and the data corrections required because of those geometry changes limited the accuracy of those measurements. As a result, inclinometers were attached to all specimens in pairs at locations such as illustrated in Fig. 3-9. Inclinometers are potentiometers, which measure slope or rotation. The inclinometers were used in pairs placed on opposing sides (East and West) at the center of the tube. These provided redundant rotation measures, which could be used as a check of the LVDT data. They directly provide inelastic rotation at critical locations, and they can be used to determine average curvature in the critical regions of the tube and the connection. It should be noted that all LVDTs, potentiometers, and inclinometers were calibrated prior to testing, and the calibration of each instrument was rechecked immediately prior to each test.

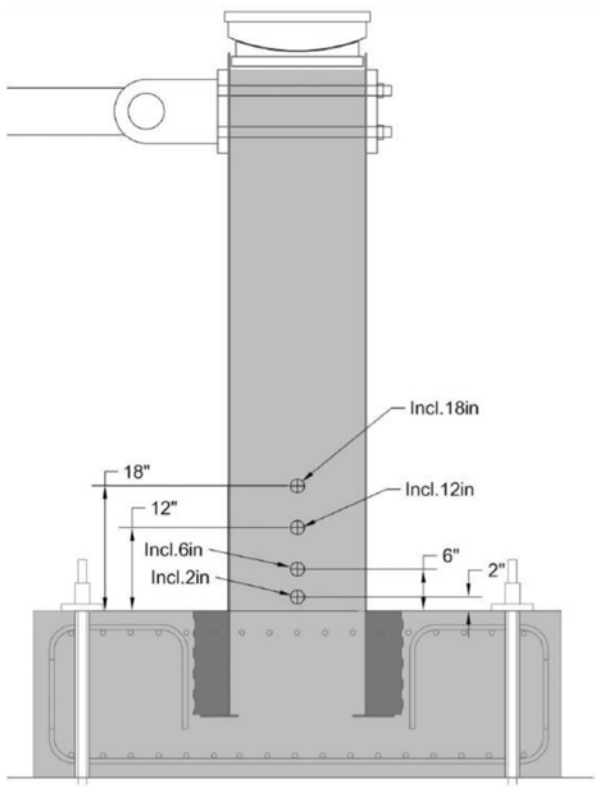

Figure 3-9. Typical Inclinometer Placement

The inclinometers were more consistently accurate in predicting column and connection rotation than the LVDT pairs described earlier. However evaluation of the instrumentation suggests that there were still unresolved issues in using this system. An Optotrak Certus motion capture system was purchased on an NSF equipment grant during the course of this research program. The system consists of a 3-dimensional optical sensor and a series of LED markers, which were attached to the specimen with adhesive foam pads and emit an electronic signal that is photographed by the optical sensors. The optical sensor consists of 3 precision cameras, which locate the position of each LED marker in 3 dimensional space by triangulation of the relative positions noted by each camera. This system was used to capture the buckled shape, inelastic rotation and deformation of the tube for Specimens L-3 through L-7. Only partial information was available for Specimens L-3 and L-4, because only one set of 3 optical camera was available for these tests, and only a portion of the critical area could be observed. However, two sets of 3 optical cameras were available for Specimens L-5 through L-7. As a result, these measurements

were compared to the LVDT and inclinometer data, and the Optotrak data clearly provided the most accurate and most consistent measurements of the inelastic performance of the system. The data provided by these measurements clearly provided the distribution of inelastic deformation, inelastic rotation and elongation obtained with the other measurements, but they also provide more accurate measurements of buckling bulge deformation and the initiation of buckling. Figure 3-10 provides photographs of the optical cameras and the placement of the LED markers on one of the test specimens.

a) b)

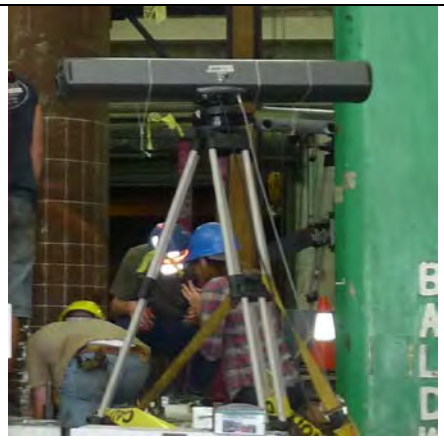

(a) (b)

Figure 3-10. Optotrak Measuring System; a) Optical sensor, b) Typical LED emitter placement

Chapter 4

CALTRANS Connection Experimental Results

A primary focus of the research was the experimental testing of seven CFT column-to-foundation connection specimens. The specimens investigate the impact of several design parameters on the response including type of tube, material properties, type of connection, and embedment length. The tests were completed during the period between September 10, 2009 and July 8, 2011. The specimens were designed built and instrumented as summarized in Chapter 3. The individual test results are reviewed and summarized here. Chapter 5 provides comparisons and further evaluation of the test results.

4.1 OVERVIEW OF TEST MATRIX

Table 3-1 provides and overview of the seven (7) test specimens. Table 4-1 summarizes as the general test results.

Table 4.1 Experimental Parameters and Test Results

Spec.	l_e/D	Specific Goals	Max. Drift %	Load @ Max Drift	Rotation @ Max. Load	Max. Load (kN)	Failure Mode
CT-1	0.8	Embedded - straight seam tube	11.6%	356	3.1%	538	DT
CT-2	0.775	Recessed - straight seam tube	10.4%	365	3.2%	530	DT
CT-3	0.775	Embedded - evaluation of le	7.5%	467	2.8%	512	DT
CT-4	0.8	Recessed - evaluation of le	7.3%	454	-3.1%	521	DT
CT-5	0.7	Recessed - evaluation of le	7.4%	476	-3.4%	601	DT w/ limited cracking
CT-6	0.6	Recessed - evaluation of le	7.4%	525	3.2%	587	DT w/ Cracking
CT-7	0.62	Recessed – 762 mm tube – 1486 kN axial	7.6%	801	3.0%	837	DT w/ very limited cracking

DT = Ductile tearing of the tube

The maximum drift in this table is the drift corresponding to significant loss of lateral resistance. In some cases, this is referred to as the specimen rotation, where the rotation is

expressed in percentage rather than radians. In a CFT member, the majority of the deformation occurs in the connection and therefore the drift is approximately equal to the rotation.

The maximum lateral load typically is associated with observable local buckling of the tube. While the maximum lateral load occurred at this deformation, the maximum moment occurred at larger deformations, because the moments increased with increasing deformations despite the still decrease in lateral loads. The following sections summarize the experimental observations and measurements of the test specimens.

4.2. SUMMARY OF INDIVIDUAL TEST RESULTS

SPECIMEN CT-1 (STRAIGHT SEAM TUBE WITH EMBEDDED CONNECTION)

Specimen CT-1 used a straight seam welded tube with the monolithic connection. The embedment depth was 400 mm (16 in. or 0.8D). Figure 4-1 shows the measured moment-rotation response.

There was no observable damage at smaller deformations, up to 0.5% drift or connection rotation. A thin crack formed between the tube and concrete footing at 0.8% drift on the tension side of the column in each direction, and hairline cracks in the footing were also observed propagating radially from the tube in East and West directions. Inelastic action (yielding) in the tube clearly exceeded the yield strain at 0.9 connection rotation. At 3.2% rotation, several new hairline cracks formed on the surface of the footing as shown in Fig. 4-2a, but footing cracking did not propagate at connection rotations beyond 3.2%. A shallow footing spall, which was less than 12 mm (0.5 in.) deep, occurred at 4.5% drift on the North side of the specimen as illustrated in Fig. 4-2b.

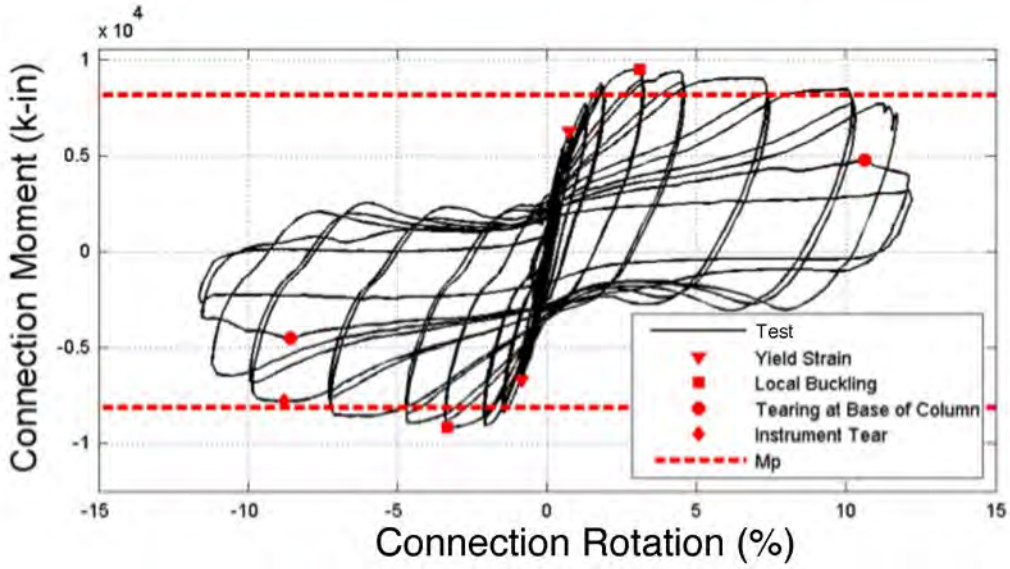

Figure 4-1. Moment-Rotation Behavior of Specimen CT-1

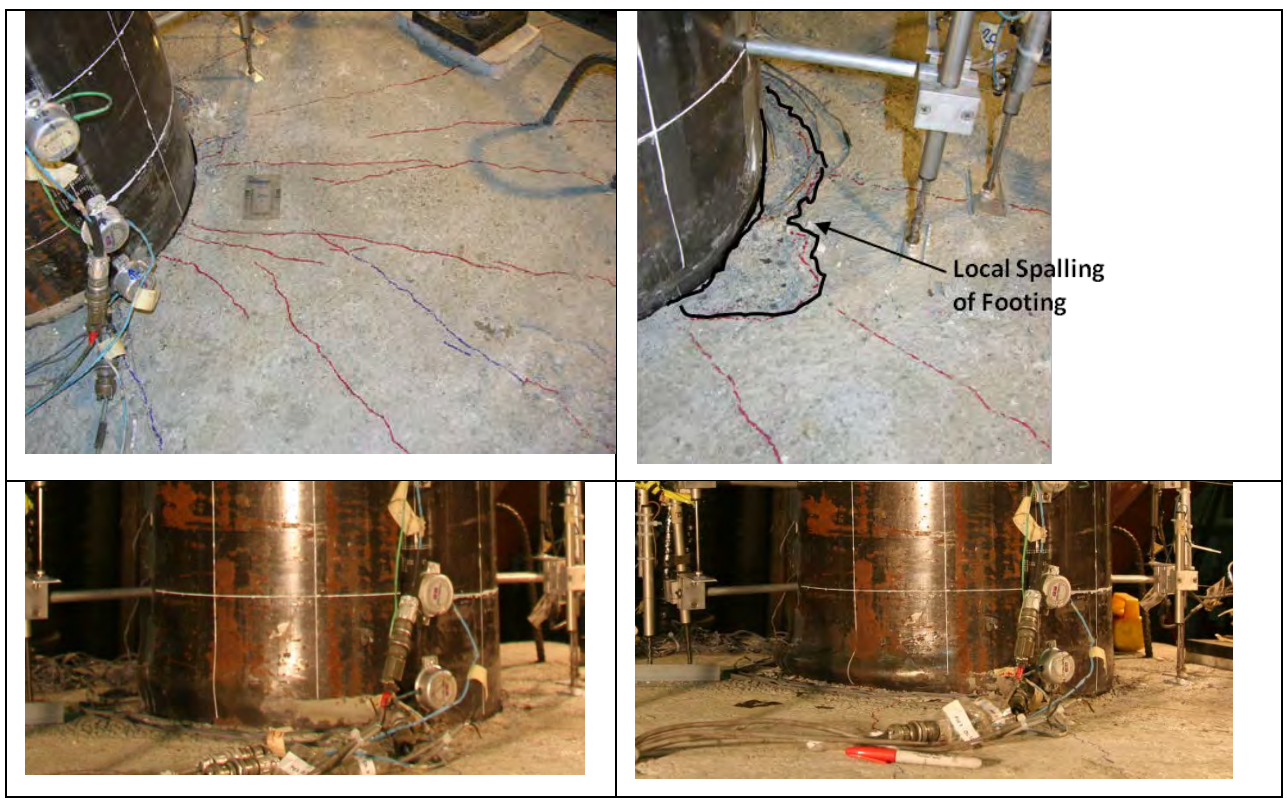

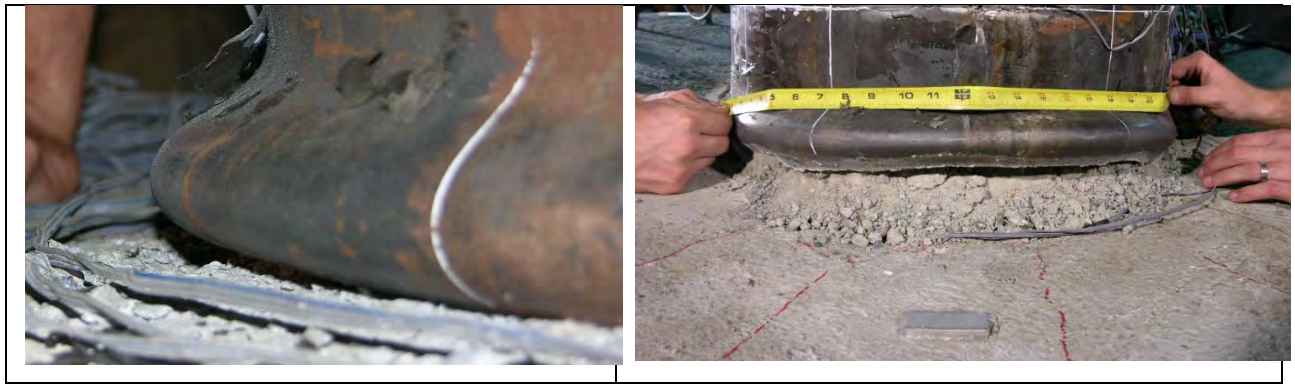

Figure 4-2. Photos of Specimen CT-1; a) Radial cracks at 3.2%, b) Local spalling at 5.5%, c) Local buckling at 3.2%, d) Local buckling at 7.5%, e) Local buckling at 10%, f) Torn tube at 11.6%

Local buckling was observed on both sides of the tube at the 3.2% drift, with the apex of the buckled region located approximately 50 mm (2 in.) above the footing surface. The out-of-plane displacement from local buckling increased with successive cycles as shown in Figs. 4.2c and d for 4.5% and 7.5% connection rotation, respectively. The aspect ratio of the buckled shape changed as the buckling increased. The buckled region was 50 mm (2 in.) in length at 10% rotation (see Fig. 4.2e). A 62 mm (2.5 in.) tear initiated on South side of specimen six in. above the footing surface a connection rotation of 9.8%. The tear initiated on both sides of the specimen and grew longer with continued cyclic deformation.

At 11.6% connection rotation, the tear was 425 mm (17 in.) long on the North side of tube as shown in Fig. 4-2f. At completion of the 11.6% cycles, approximately 63% of the circumference of the tube was torn, but approximately 30% to 40% of the moment capacity remained. The tearing generally occurred in the severely deformed region with local buckling of the tube. One tear initiated for drilled hole placed for instrumentation, and hence this crack development may have been premature and influenced by the test setup. The maximum and minimum moments in the CFT column at the top of the footing were 107.4 kN-m and -103.8 kN-m (9508 k-in and -9191 k-in), respectively.

SPECIMEN CT-2 (STRAIGHT SEAM TUBE WITH GROUTED CONNECTION)

Specimen CT-2 had a straight seam welded tube and was grouted 382 mm (15.5 in. or 0.775D) into the footing. Figure 4-3 shows the moment-rotation behavior of the specimen. There was no observable damage at deformations up to 0.5% connection rotation. A considerable amount of water bled to the surface during setting of the grout, and many shrinkage cracks and reinforcing fibers were at the surface of the grout as shown in Fig. 4-4a before starting the test. This complicated crack identification in the grout, but very limited growth in these shrinkage cracks was noted during the small deformation cycles of the test.

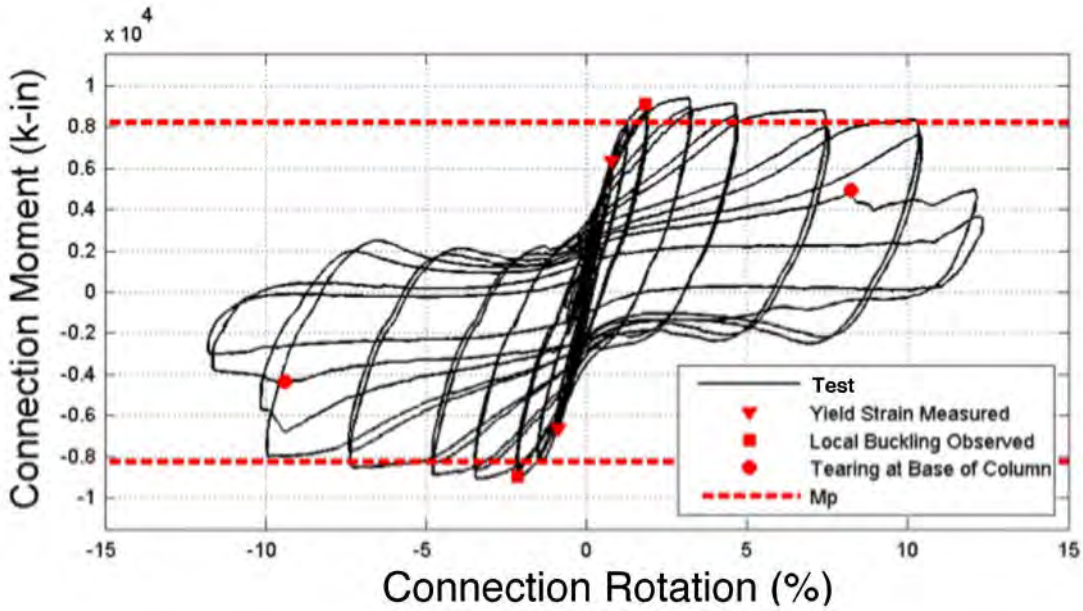

Figure 4-3. Moment-Rotation Behavior of Specimen CT-2

Apparent yielding of the steel tube occurred at a connection rotation of 0.9%. Hairline cracks formed in the footing at approximately 1.5% connection rotation, but the extent of this cracking remained stable throughout the remainder of the test. Local buckling was first observed on the north side of tube at 2.2% connection rotation. The bulge of the local buckling grew larger with increasing deformation as seen in Figs. 4.4b, c, and d. The maximum height of the bulge was approximately 9.5mm (3/8 in.) over a 82 mm (3.5 in.) length at 3.3% rotation and approximately 25 mm (1 in.) amplitude over 50mm (2 in.) length at 10% rotation.

Tearing initiated in the highly strained region near the peak of the bulge of the buckled area during the 3rd cycle with more than 10% connection rotation. Figure 4.4e is a photograph

of local striations, which preceded tearing in this and most other specimens. The tearing progressed rapidly with increasing deformation and a large portion of the perimeter was torn at 11.6% rotation as shown in the photo of Fig. 4-4f. The maximum drift achieved prior to failure was 10.3% and the minimum drift was -9.9%. The maximum and minimum moments in the CFT column at the top of the footing were 106.2 kN-m and -102.2 (9394 k-in and -9043 k-in), respectively. The surface of the grout appeared to remain level throughout the test, but slight differential movement (less than 3 mm or 1/8 in.) between the surface of the grout and corrugated pipe interface was seen during a review of the photographs following the test.

Figure 4-4. Photos of Specimen CT-2; a) Original condition of grout, b) Local buckling at 3.2%, c) Local buckling at 7.5%, d) Local buckling at 10.4%, e) Striations noted prior to tearing, f) Tearing around much of the perimeter of the tube at 11.6% rotation

SPECIMEN CT-3 (SPIRALLY WELDED TUBE WITH GROUTED CONNECTION)

Specimen CT-3 was a spirally welded tube, which was grouted 382 mm (15.5 in. or 0.775D) into the footing. Figure 4-5 shows the moment-rotation behavior of the specimen. Two hairline cracks occurred in the grout during the first cycle of the test, and several more hairline cracks formed in the grout with during subsequent cycles. Additional cracks formed cracks formed in the concrete footing at the grout-corrugated pipe interface at 0.2% drift. Figure 4-6 illustrates the location and extent of this early cracking, and, all cracks remained small and little additional cracking developed during the subsequent testing. Yielding of the steel tube was clearly noted at 0.8% connection rotation. Local buckling was observed at 1.5% drift and on the south side at 1.9% drift, and no additional cracking was noted after visual identification of local buckling in the tube.

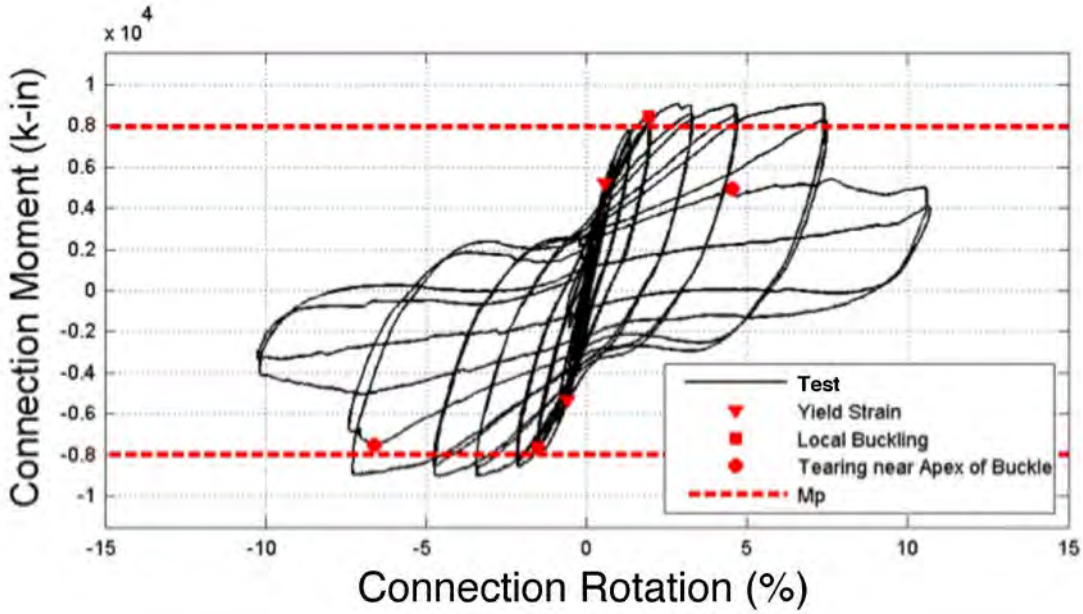

Figure 4-5. Moment-Rotation Behavior of Specimen CT-3

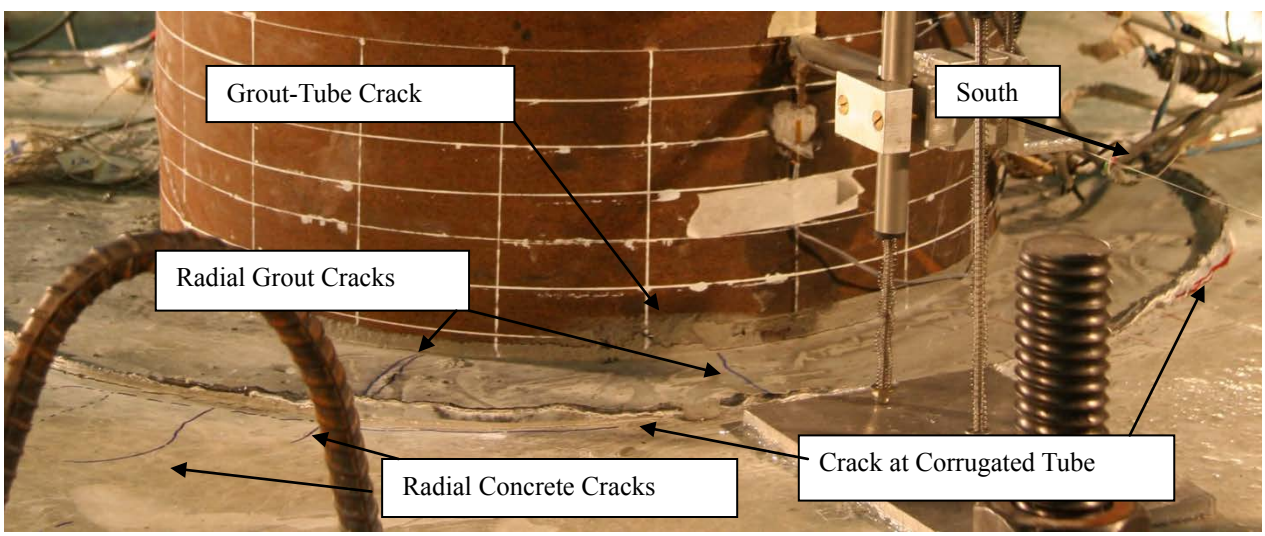

Figure 4-6. Crack Formations on South Side of Specimens (0.6% drift)

As with Specimens CT-1 and CT-2, the inelastic performance of the CFT pier was dominated by yielding and local buckling of the tube. The height of the bulge of the buckle increased with increasing connection rotation. The initiation of buckling and the buckling deformation were more accurately assessed for this and subsequent test specimens with the NDI Optotrak instrumentation seen on Fig. 4-7a.

Tearing initiated at the buckle and progressed around the perimeter of the tube with increasing deformation demand, as in Fig. 4-7b. During the second cycle at 7.3% connection rotation, a tear of approximately 10% of tube circumference occurred on the south side of tube 38 mm (2.5 in.) above the footing. A larger tear on the north side of the tube, which ultimately extended around 37% of the perimeter, initiated in the first cycle to 10.6% drift (see Fig. 4-7b) The maximum and minimum drift achieved prior to failure was 7.45% and –7.25%, respectively. The maximum and minimum moments of the CFT column at the top of the footing were 102.6 kN-m and -101.7 kN-m (9081 k-in and -8998 k-in), respectively. More than 50% of the maximum moment capacity was retained for connection rotations greater than 10%.

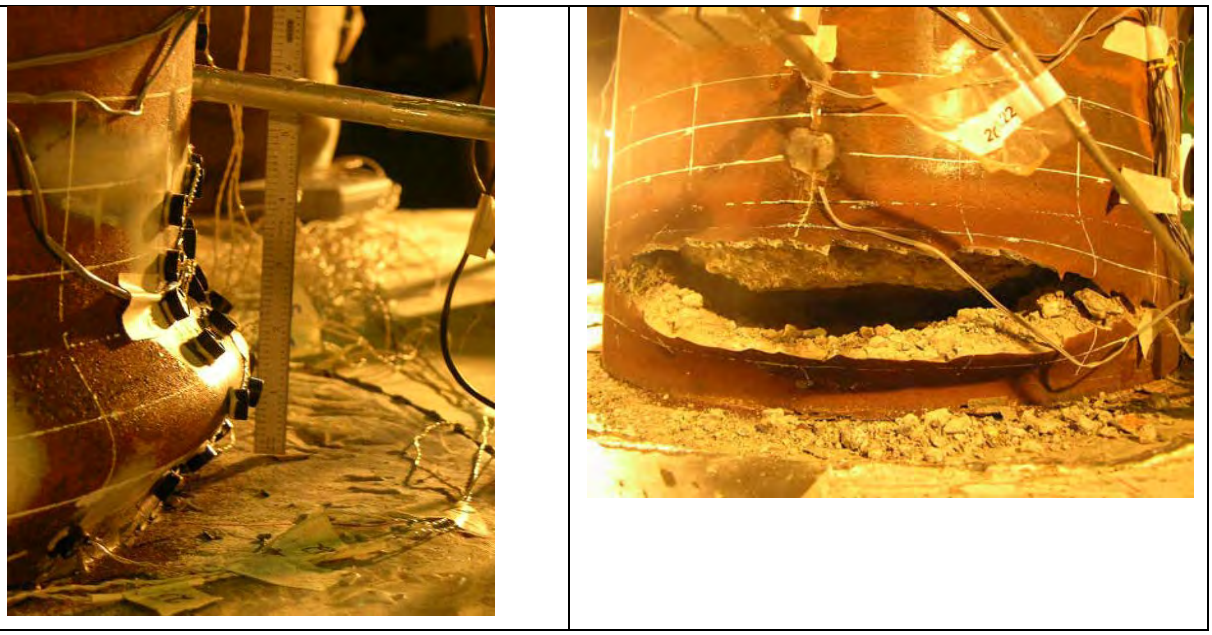

Figure 4-7. Photos of Specimen CT-3; a) Severe local buckling. b) Tearing at 7.3%

SPECIMEN CT-4 (SPIRALLY WELDED TUBE WITH EMBEDDED CONNECTION)

Specimen CT-4 was a spirally welded tube, which was grouted 350 mm (18 in. or 0.9D) into the reinforced concrete footing. Figure 4-8 shows the moment-rotation behavior of Specimen CT-4. There was no observable damage at deformations up to 0.5% connection rotation. Cracking was not observed footing at connection rotations less than 0.7%. A slight separation between the tube and the concrete on the tension face occurred at 0.3% rotation as

illustrated in Fig. 4-9a. As with prior specimens, this separation increased in size as the rotation increased.

Yielding of the steel tube was detected at 0.8% rotation. Two footing cracks propagated radially away from the tube in the East and West direction at 0.8% drift. Two vertical cracks appear on the North side of footing at 1.2% drift and hairline cracks formed radially outward from tube on the surface of footing at 2% drift. Buckling was observed on the South side of the tube at 1.8% drift. Shallow spalling occurred at the concrete-tube interface on both the East and West side initiated from the first surface cracks on the specimen at 4.5% drift, but no visible footing damage cracks remained small and remained stable beyond this point.

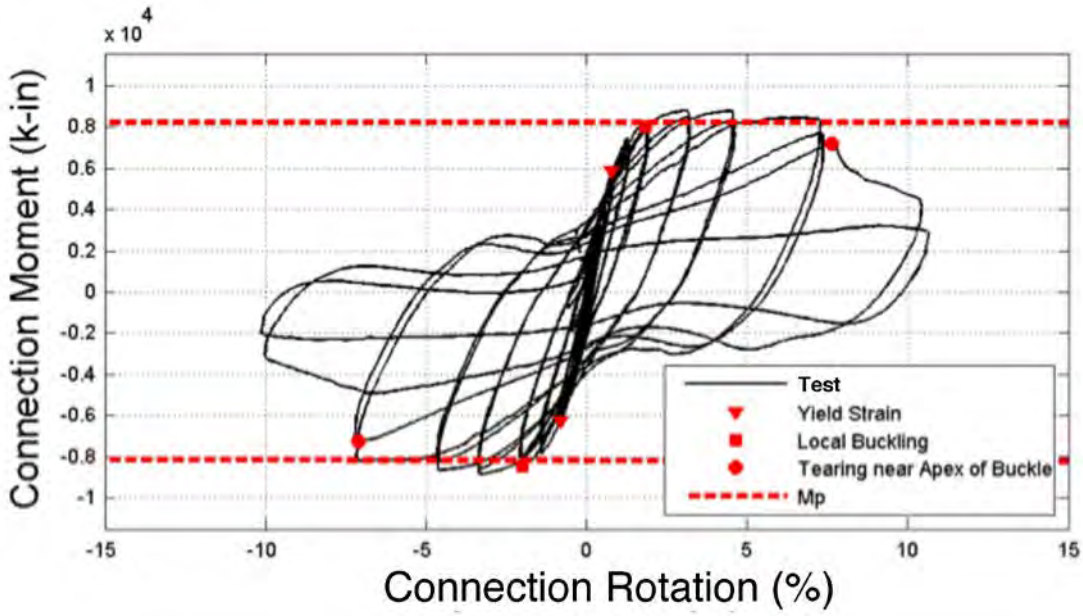

Figure 4-8. Moment-Rotation Behavior of Specimen CT-4

As with prior tests, the amplitude of the bulge of the buckle increased with increasing deformation as shown in Fig. 4-9b, c, and d. At 7.3% drift a tear occurred near the apex of the buckled region on the south side of tube along the spiral weld line as shown in Fig. 4.9e. The tear initiated in the base metal in the heat-affected zone of the weld, and it ultimately branched into tear through the highly strained region of the local buckle as shown in Fig. 4-9f. The maximum drift prior to failure was 7.13% and the minimum drift was -7.21%. The maximum

and minimum moments in the CFT at the top of the footing were 99.5 kN-m and -99.6 (8806 k-in and -8817 k-in), respectively.

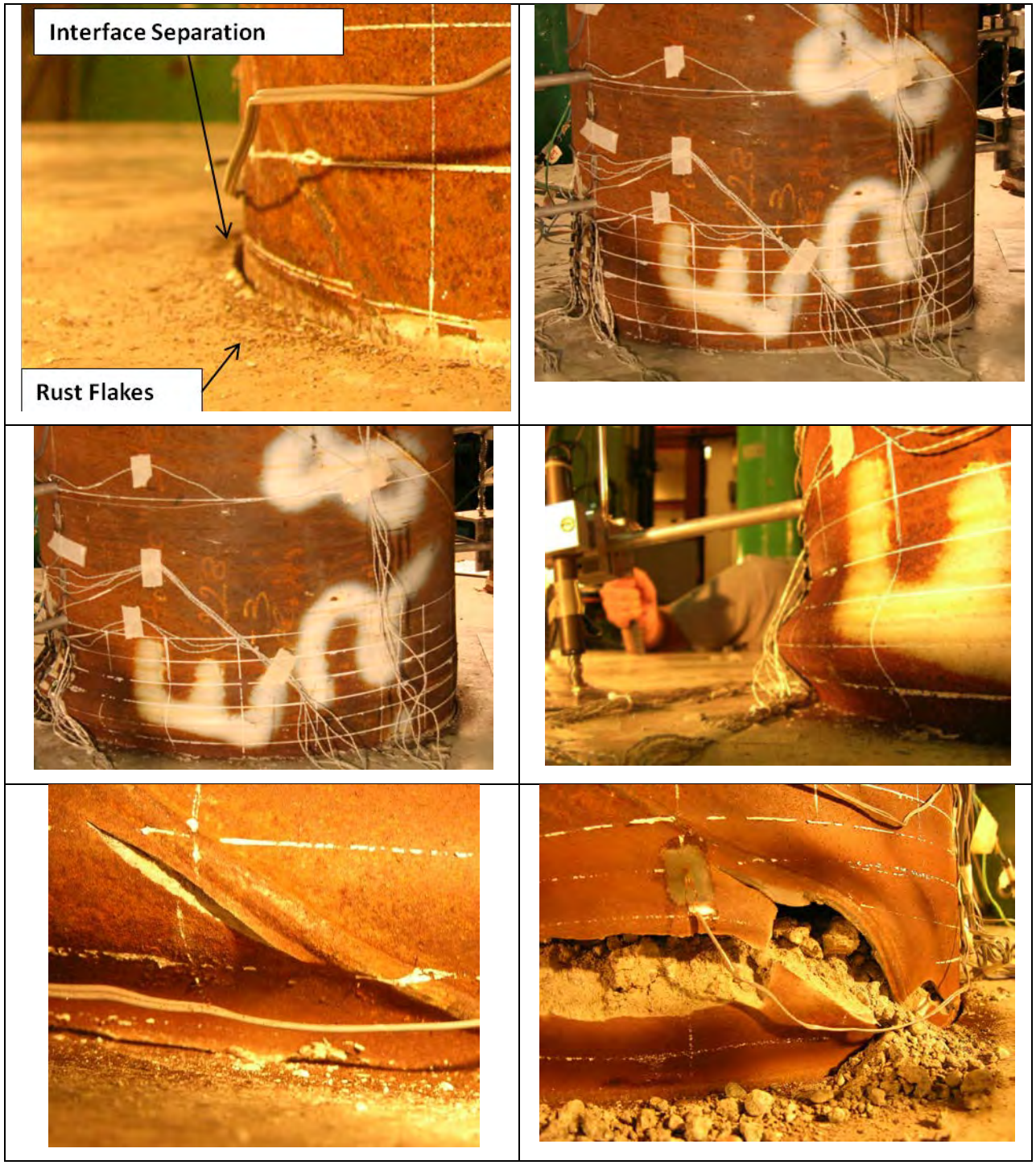

Figure 4-9. Photos of Specimen CT-4; a) Interface separation at 2.2%, b) Local buckle at 3.1%, c) Local buckle at 4.5%, d) Local buckle at 7.3%, e) Initiation of tearing in spiral weld, f) Final tear through local buckle

SPECIMEN CT-5 (SPIRALLY WELDED TUBE WITH GROUTED CONNECTION)

Specimen CT-5 used a spirally welded tube, which was grouted 350 mm (14 in. or 0.7D) into the reinforced concrete footing. Figure 4-10 shows the moment-rotation behavior of Specimen CT-5. This specimen had a smaller embedment depth than prior specimens to evaluate the impact of an embedment depth that sustains some footing damage. Prior specimens had minimal footing damage, and this specimen focused upon establishing the minimum embedment depth required for ductile connection performance.

The first cracking occurred in the grout and footing were noted at 0.6% and 0.8% connection rotation, respectively. Yielding in the steel tube was noted at 0.8% connection rotation. Extensive cracking east and west of the corrugated tube occurred between 1 to 2% connection rotation with new cracks forming during each cycle. Cracking was much more extensive in Specimen CT-5 than noted for the earlier specimens as shown in Figs. 4-11a and b. Concrete cracking generally increased until about 3.2% connection rotation, where local buckling was clearly observed. At this point no further footing damage was noted and the ultimate failure mode was similar to that noted for other specimens.

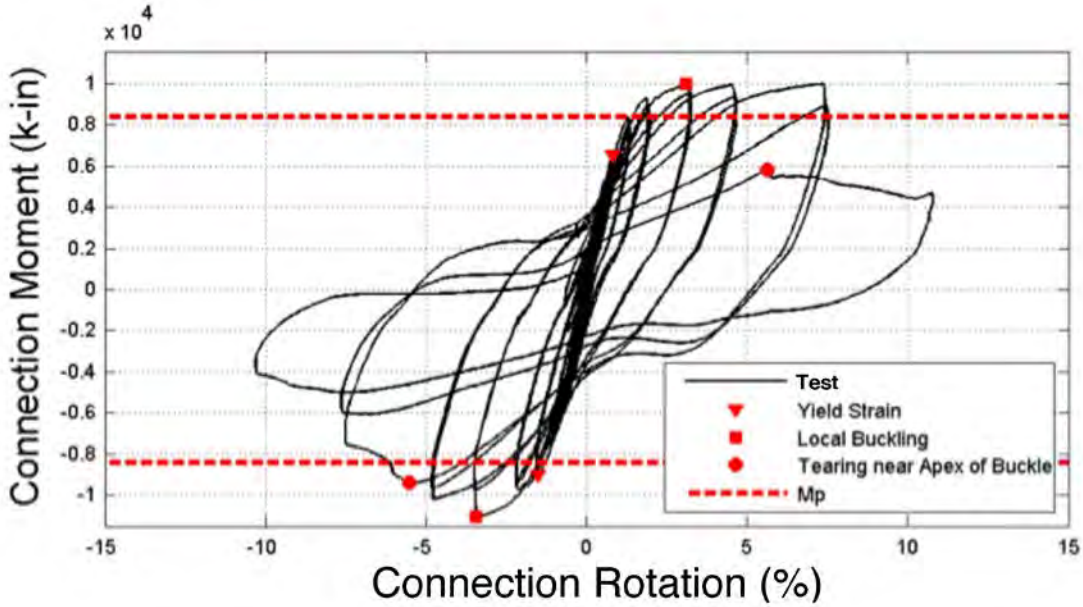

Figure 4-10. Moment-Rotation Behavior of Specimen CT-5

Figure 4-11. Photos of Specimen CT-5; a) Foundation cracking at 0.8% b) Foundation cracking at 3.2%, c) Local buckling at 4.8%, d) Tearing at south side at 7.4%, and e) Ultimate failure

Tearing initiated during the first 7.4 % drift cycle on the south side of the specimen. The tear initiated 25 mm (1 in.) above the footing surface where the weld met the surface of the footing and slowly propagated along the weld for approximately 425 mm (13 in.). The tear eventually was perpendicular to the axis of the column, as shown in Fig. 4-11d. The tear on the North side of the column occurred at 10.7 % connection rotation. It initiated near the apex of the bulge of the buckle, and was perpendicular to the axis of the CFT member as shown in Fig. 4-11e.

The maximum and minimum connection rotations achieved prior to failure were 7.41% and –4.81%, respectively. This is clearly smaller than more deeply embedded specimens such as

Specimen CT-3, and it should be emphasized that tearing initiated in one direction at a smaller deformation than the other direction. The maximum and minimum moments in the CFT column at the top of the foundation were 112.7 kN-m and -124.8 kN-m (9970 k-in and -11048 k-in), respectively.

SPECIMEN CT-6 (SPIRALLY WELDED TUBE WITH GROUTED CONNECTION)

Specimen CT-6 used a spirally welded tube, which was grouted 300 mm (12 in. or 0.6D) into the reinforced concrete footing. Figure 4-12 shows the moment-rotation behavior of Specimen CT-6. This specimen had the smallest embedment depth of those testing in this series.

As with Specimen CT-5, footing cracking developed early in this test, and progressed significantly in subsequent cycles. However, as noted with Specimen CT-5, there was no evidence of cone pullout failure and the ultimate failure was ductile tearing of the tube in the severely deformed sections of the member. Figure 4-13a and b illustrate cracking during the early cycles of testing.

As with CT-5, local buckling of the tube was noted at approximate 3.2% connection rotation. After local buckling of the tube, the growth of foundation cracking was limited, and the damage occurred in the highly yielded portions of the tube. Fig. 4-13c shows the local buckle at 7.5% connection rotation. This buckling is quite comparable to other specimens in the series. Tearing initiated at the weld approximately 50 mm (2 in.) above the footing surface on the North Side of the Footing at 7.5% drift. The tear followed the weld toward the east and was parallel to the footing toward the west as illustrated in Fig. 4-13d. The south side of the tube tore during the following cycle to 10.2% drift and was parallel to the footing, but propagated diagonally upward on the southwest side with a total length of 31% of the circumference as illustrated in Fig. 4-13e. After the final cycle to 10% drift was complete nearly 80% of the tube was torn.

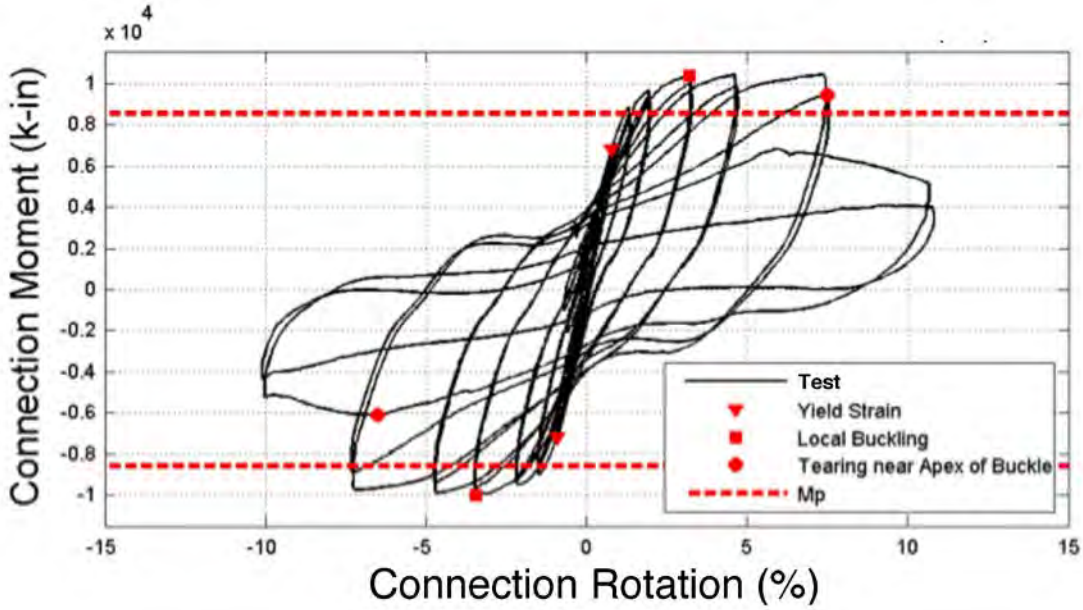

Figure 4-12. Moment-Rotation Behavior of Specimen CT-6

Figure 4-13b shows the final damage state in the footing just prior to initial tearing of the tube. Cracks formed on all sides of the footing totaling 25 cracks of 150 mm (6 in.) in length. The cracks were spaced approximately 15° apart around the center of the column. The maximum and minimum connection rotations achieved prior to failure were 7.43% and -7.25%, respectively. The maximum minimum moments of the CFT column at the top of the foundation were 118.1 kN-m and -113.1 kN-m (10449 k-in and -10013 k-in), respectively.

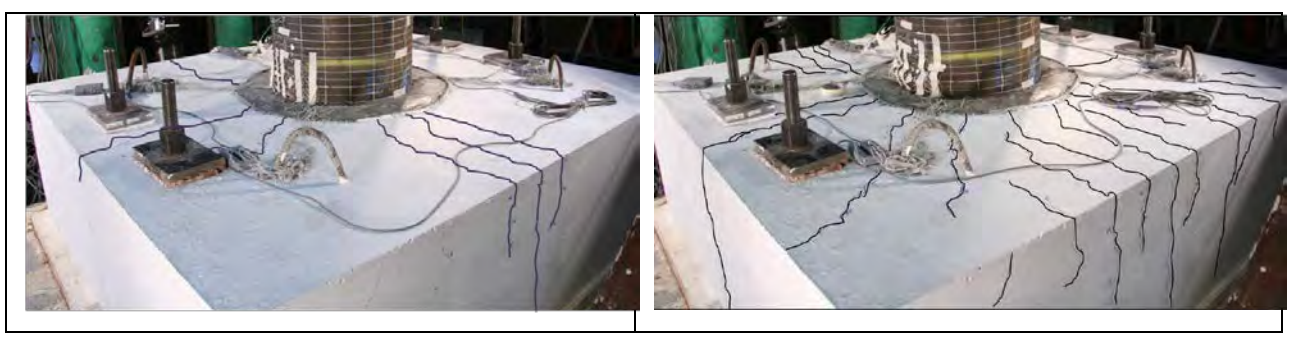

Figure 4-13. Photos of Specimen CT-6, a) Footing cracking at 1.2%, b) Footing cracking at 3.2%, c) Local buckling at 7.5%, d) Tearing of tube on north side, e) Tearing on south side

SPECIMEN CT-7 (SPIRALLY WELDED TUBE WITH GROUTED CONNECTION)

Specimen CT-7 was a 750 mm (30 in.) diameter spirally welded tube, which was grouted 450 mm (18 in. or 0.6D) into the concrete footing. This specimen had multiple test goals of evaluating relatively shallow embedment depth and large diameter and slenderness ratio ($D/t = 120$). The specimen was loaded with constant axial load equal to 5% of the gross axial capacity or 1485 kN (333.6 kips). However, prior to start of the test, an inadvertent compressive load of 9.64 MN (2166 kips or approximately 33% of the crushing load) was applied to the specimen. The specimen was carefully examined after this initial overload, and local damage to the concrete immediately below the spherical bearing was observed as shown in Fig. 4-14a. However, no other damage to the specimen was noted.

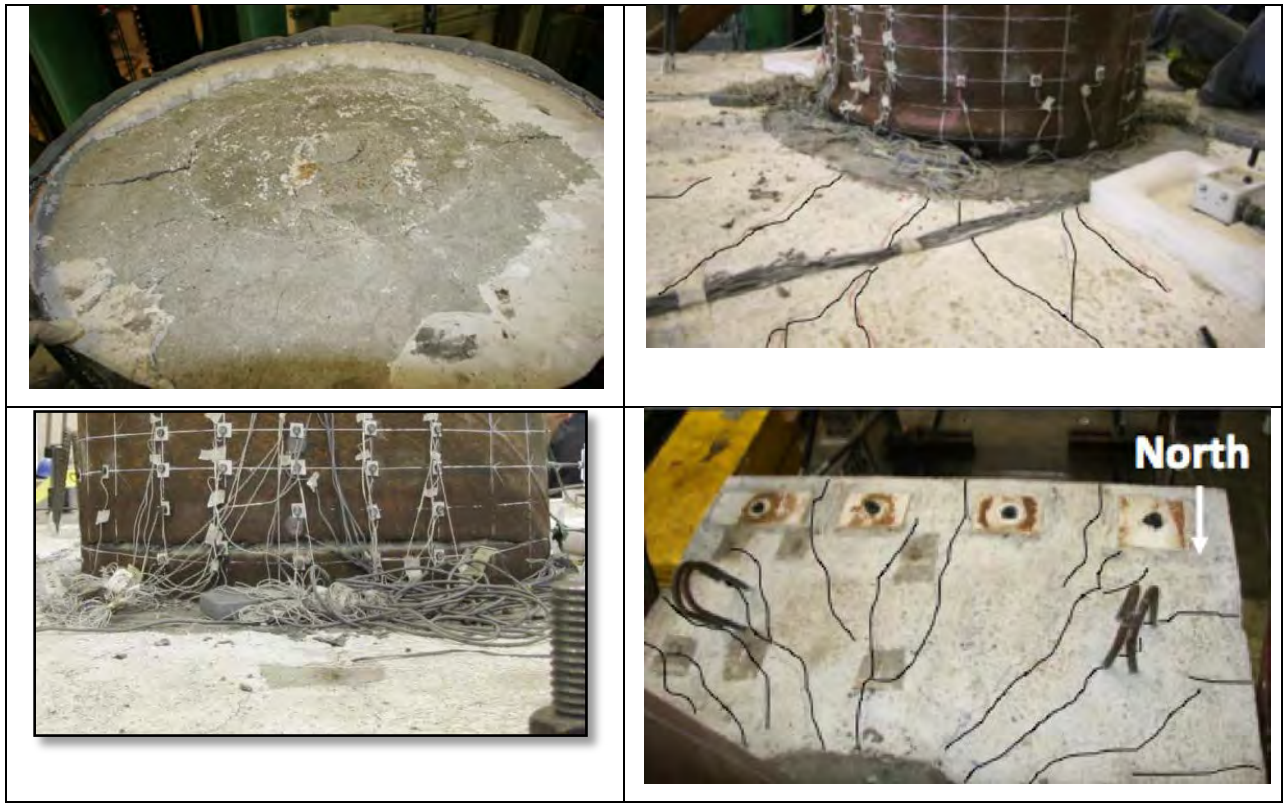

Figure 4-14. Photos of Specimen CT-7; a) Local damage to concrete at the top of the column due to initial overload, b) Foundation cracking and local buckling at 6.5% rotation, c) Tear in steel tube at 8.1%, and d) Foundation cracking at end of the test

Figure 4-15 shows the moment-connection rotation plot for this specimen. Hairline surface cracking in the grout occurred during the initial cycles of -0.21% connection rotation. New cracks and crack propagation continued to occur in the footing in subsequent cycles and increased deformation levels as illustrated in Figs 4-14b and d. Initial yielding of the steel tube was noted at 0.76% connection rotation. There was approximately 7 mm (1/4 in.) of relative slip between the corrugated pipe relative and the foundation at 1.0% connection rotation, but no increase of this slip was noted during the remainder of the test. This was the biggest specimen tested with the self-reacting load frame illustrated in Fig. 3-3 and described in Section 3-3, and the test was interrupted at this deformation for stiffening and strengthening this load frame as noted in the prior discussion. This interruption had not impact on the performance of the specimen.

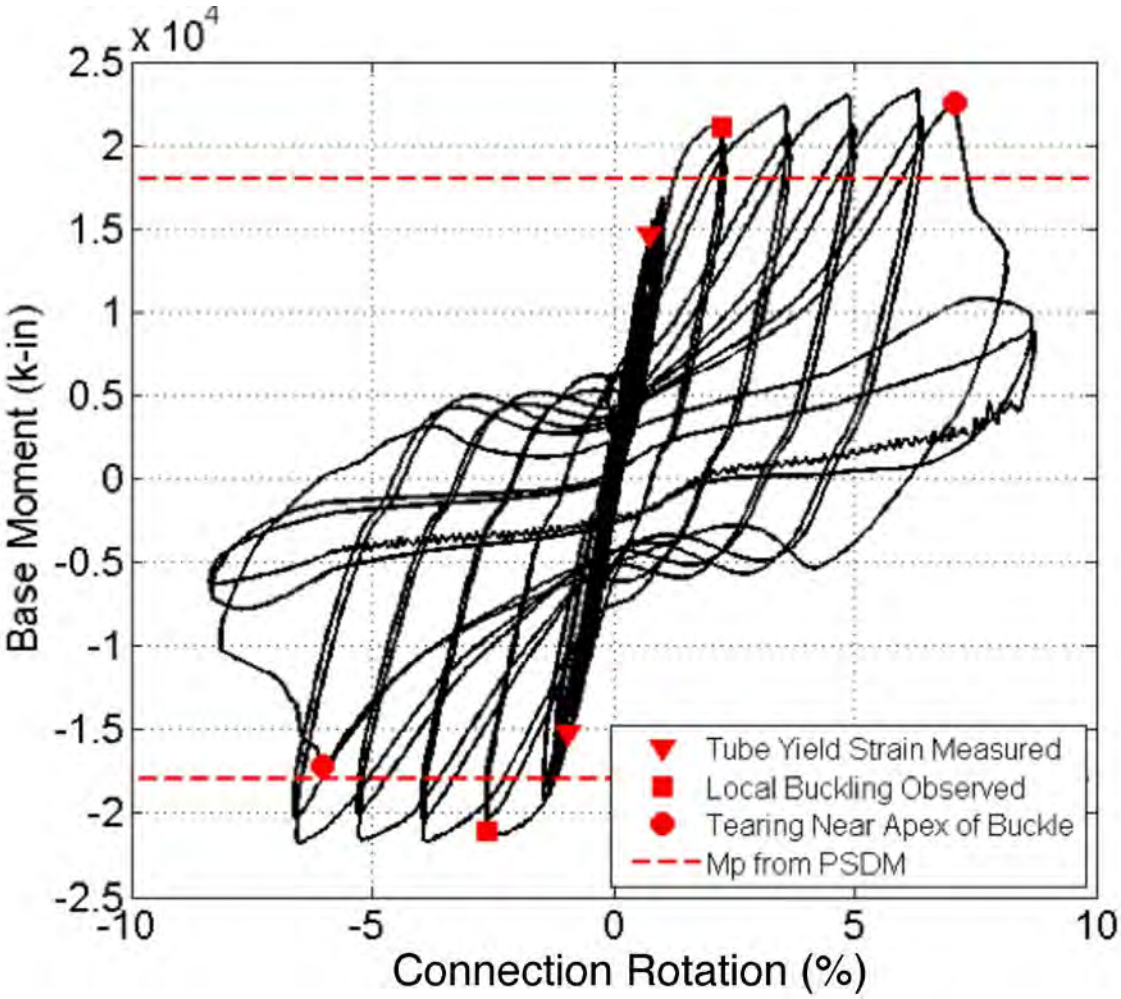

Figure 4-15. Moment-Rotation Curve of Specimen CT-7

Testing was resumed 11 days later, and local buckling was observed at 2.24%. The apex of the bulge of the buckle was approximately 62 mm (2.5 in.) above the surface of the footing. The amplitude of the bulge of the buckle and extent of foundation cracking increased with increasing deformation as shown in Fig. 4-15c. Tearing of the tube initiated at 7.06% connection rotation on the north side of the tube and 8.13% on the south side of the tube. The maximum and minimum moments in the CFT column at the top footing observed throughout the test was (23,231 k-in and -21,735 k-in) occurring at 6.30% and -6.49% connection rotation, respectively.

4.3. SUMMARY COMMENTS AND FURTHER ANALYSIS

This has provided a brief summary of the seven connection tests performed on this research program. The results of these tests will be combined with the results of prior work to provide additional analysis and evaluation of the behavior and the development of initial design recommendations in Chapter 5.

Several issues are worthy of note from these seven (7) tests. All specimens provided good inelastic performance with ductile failure modes. However, the depth of embedment clearly affects the deformation capacity and failure mode of the connection, since the shallow embedded specimens (CT-5, CT-6, and CT-7) had significantly more footing damage and prior specimens C-1 and C-2 had brittle failures with limited inelastic deformation capacity. The impact of the embedment was considered in more detail with respect to the study parameters of type of tube, embedment depth, and type of connection.

The inelastic deformation capacity of Specimens CT-1 and CT-2 was significantly larger than that achieved with Specimens CT-4, CT-5, CT-6 and CT-7. Specimens CT-1 and CT-2 used straight seam welded tube, which had a different grade of steel, and somewhat deeper embedment and different grades of steel. The steel used in the straight-seam tube for Specimens CT-1 and CT-2 was somewhat more ductile with greater CVN toughness, increasing the deformation capacity of Specimens CT-1 and CT-2.

Spiral welding had a minor impact performance, with tearing initiated and partially propagated along the spiral in Specimens CT-5 and CT-6. The steel tube was cut away from all specimens after completion of testing, and examination of the specimens show that extremely good bond was achieved in the spirally welded tubes, since the spiral welds are raised slightly about the inside of the tube and provide some interlock with the concrete. This interlock is advantageous for columns with light compressive loads or tensile axial load (that might result from overturning in an earthquake). While bond stress is highly desirable, this greater bond stress may have reduced the inelastic deformation capacity of the spirally welded specimens. This is evident in reinforced concrete construction for which the deformation capacity is increased with intentionally debonded reinforcing steel.

Further, it must be recognized that the deformation capacity achieved with these slender specimens is much greater than would normally be expected. The research clearly demonstrates the reason for this behavior. The NDI Optitrak measurements clearly show that 40% to 60% of the plastic rotation is contributed by yielding of the steel embedded within the footing (Lee 2011). This steel is totally encased in concrete and is unaffected by local buckling. Hence, it contributes large inelastic deformations, and larger embedment depth may offer the potential for somewhat greater connection rotation. This observation may explain variations in performance noted in Specimens CT-4, CT-5 and CT-6.

Specimen CT-7 had strain gauges attached to the reinforcing bars in the footing, and these gauges provide insight as to the stress distribution in the reinforcing steel. The measurements showed that longitudinal reinforcing bars that pass immediately outside the embedded tube carry significant bending stress as assumed in the design calculations. Longitudinal reinforcing bars that are interrupted by the tube carry very little stress in the vicinity of the tube as assumed in the design. Finally shear reinforcement in the cone-pullout region of the connection carry significant stress and they play a significant role in developing connection ductility.

Chapter 5
Design Expressions for CFT Columns and Fully Restrained Footing and Cap-Beam Connections

5.1. **INTRODUCTION**

CFTs have engineering properties that offer strength and stiffness beyond a conventional reinforced concrete member. The research reported herein was undertaken to investigate the possibility of using CFT piers in bridge construction. The research has shown that (1) CFT columns can sustain multiple cyclic drifts to large levels with minimal damage and (2) the fully restrained connections tested and simulated as part of this research program provide the expected strength and stiffness of the column.

The research has studied two types fully restrained connections for CFT pier columns, as illustrated in Figs. 5-1 and 5-2. Both options employ a flange or annular ring, as shown in Fig. 5-3. This annular ring is attached to the bottom of the concrete filled tube, which is then partially embedded in the adjacent component (shown as a foundation element in Figure 5-1 and 5-2). This anchored connection resists flexural loading from the column through strutting action to the top of the foundation (resulting from the portion tube of the CFT column that is in tension) and the bottom of the foundation (resulting from the portion of tube of the CFT column that in compression). The tests show this connection is both simple to construct and fully effective in transferring the flexural strength of the CFT column.

Two connections were studied as part of this research program. The first uses monolithic construction, as illustrated in Fig. 5-1. The tube and annular ring are temporarily anchored and cast into the reinforced concrete footing or pile cap. The second connection isolated the tube from the foundation during construction (Fig. 5-2), and is termed the grouted connection. The footing or pile cap is cast with a recess formed by light gauge corrugated metal pipe for later placement of the tube and annular ring as depicted in Fig. 5-2. High-strength, fiber reinforced grout is placed between the corrugated metal duct and the CFT column. The concrete fill is cast.

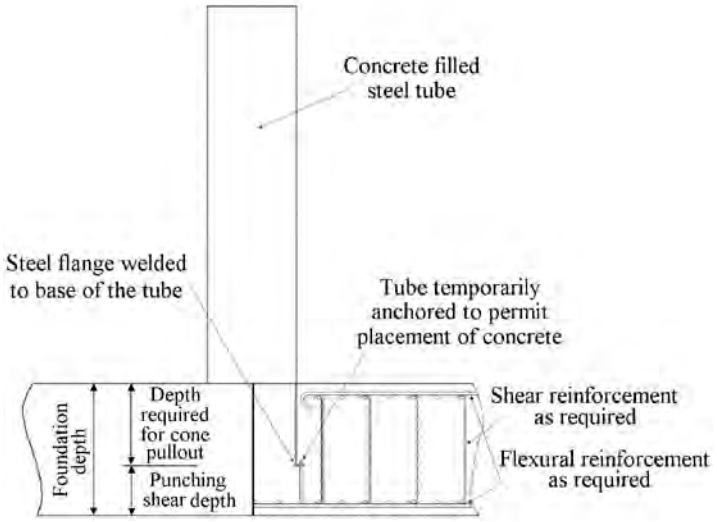

Figure 5-1. Monolithic foundation connection

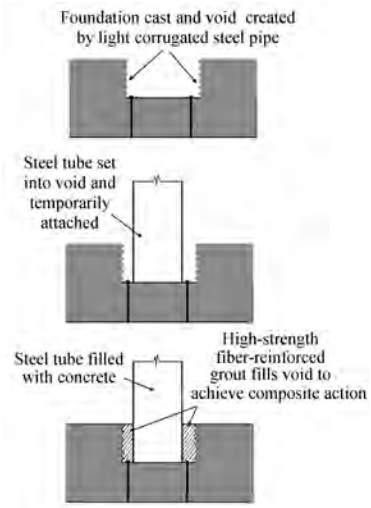

Figure 5-2. Grouted foundation connection

Figure 5-3. Welded annular ring

Although CFT columns have been studied by prior researchers, the tubes were typically small (6 inches or less in diameter) and few researchers have studied connections for bridge construction. Therefore the experimental portion of this research study is critical to the implementation of CFT columns in bridge construction. It is true that CFT components are permitted by codes, there is little community consensus on their design. The design expressions vary significantly among codes as shown in the discussion of Chapter 2, Section 2.2.

The objective of this chapter is to present validated design expression for a CFT bridge columns and fully restrained connections. The design expressions were validated using the test results describe herein as well as the extensive database gathered as part of this project.

5.2. DESIGN OF CFT BRIDGE COLUMNS

Design of CFT bridge columns requires:

1. Demands established from an appropriate model of the bridge. An elastic demand analysis will require stiffness values for the bridge column.
2. A nonlinear analysis of the bridge system will require a moment-rotation relations or plastic hinge length parameters. In the first case, the connection to be implemented as a concentrated rotational spring at the base of the connection; this is described in the section below on nonlinear analysis modeling. In the latter case, a lumped plasticity model, similar to models currently used for RC columns, is employed. This latter case was not included as part of this research study and will be investigated as future research.
3. Material properties for the concrete fill, steel tube, and fiber-reinforced grout.
4. Flexural strength of the column, including axial load (P) - moment (M) interaction.
5. Geometric limits for the tube, in particular limits on the diameter (D) to thickness (t) ratio.
6. Requirements for the concrete fill, steel tube, and grout.

This section summarizes validated expressions for each of these requirements.

MATERIAL PROPERTIES

CFT columns and their connections require four types of materials, including the concrete fill, the steel tube, the reinforcing steel (in the foundation or cap beam element), and a high-strength fiber reinforced grout. None of the materials are proprietary.

The concrete fill for the CFT member used in the testing is a low-shrinkage, self-consolidating concrete. In the testing, the concrete strength nominal strengths were 42 MPa and 70 MPa (6 ksi and 10 ksi). This is a structural concrete, and the minimum strength is 28 MPa (4 ksi), with an expected strength 25 to 50% larger. The concrete mix must specify a low-shrinkage admixture. Low shrinkage concrete is required to ensure the concrete does not shrink relative to the steel tube; a conventional concrete results in an amount of shrinkage that eliminates composite action, thereby comprising the stiffness of the component. A sample concrete mix is provided in Table 5-1.

Table 5.1 Concrete mix used in test specimens

AASHTO #8 (3/8") Aggregate	1460 lb.
Fine Aggregate	1538 lb.
Type I/II Cement	536 lb.
Type F H.R.W.R.	74.25 oz.
Type A Water Reducer	33.00 oz.
Slag (GGBFS)	289 lb.
Water	270 lb.

As indicated in the table, two admixtures were used: a high-range water reducer (Type F), also called a super plasticizer, to provide the properties required of an SCC mix and a Type A water reducer. In this case, the Type F H.R.W.R. is sold under the name ADVA 170 and the Type A water reducer is sold as WRDA64. Both are manufactured by Grace Construction Products.

Two different steel tubes have been tested. The steel tubes may either be straight seam or spiral welded tubes. Spiral welded tubes offer reduced cost, greater versatility and more rapid fabrication with large diameter tubes, since they can be formed to any diameter from a more limited inventory of materials. Spiral welded tubes are formed from coil steel, which has different material designations (AISI designations) than commonly used in AASHTO. It is recommended that that a low carbon, low alloy steel with a minimum yield stress of 350 MPa (50 ksi) and minimum elongation at break of 15% be employed. The spiral welds must be formed by the double submerged arc process, and the weld must be matching metal and meet the minimum toughness requirements of AISC Demand Critical welds (AISC 2005).

The reinforcing steel used in the foundation or cap-beam element is to be the same type of reinforcing steel used in current Caltrans construction (typically A 706).

For the grouted, isolated connections, a high strength grout, which contains an appropriate amount of fiber reinforcing, is used between the steel tube and the foundation, over the embedment depth of the connection. For the test specimens, a high-strength (70 MPa or 10 ksi) grout was obtained from Mason Supply (or equivalent) and met ASTM C-1107. The grout was mixed according the instructions provided by the supplier. A structural fiber (not shrinkage) was used to provide superior crack resistance and bounding characteristics between the tube and the corrugated metal duct. The grout was reinforced with a structural polypropylene fiber, which was supplied by Stoneway Concrete, and was designated as Strux 85/50. The fiber volume was

approximately 0.2%. The Caltrans specification for grout (Section 51-1.02G) should be followed. The use of alternative fibers, including steel fibers, will be explored in the future research study.

STIFFNESS MODELS FOR CFT COLUMNS

To size the CFT pier column it is necessary to establish the design forces on the column, which must include appropriate factored loads for all appropriate load combinations. The factored design moments for the CFT members should included secondary moments defined by the ACI side sway (ACI 318, Section 10.13) or AISC Standard 341 Chapter C design procedures.

The effective stiffness, EI_{eff}, of circular CFT is important, because it is used to evaluate deflections, deformations, buckling capacity, and moment magnification. The prior evaluation of the AISC, ACI, and AASHTO models indicate that none reliably predict the stiffness. A new expression that accounts for the impact of the axial load and effective reinforcing area on the concrete stiffness was developed; this effective stiffness factor is termed C'. The expression was verified using the compiled database. A total of 50 circular CFT tests that provided the force-deflection, moment-curvature, or moment-rotation response data were used to calibrate the equation. Eq. 5-1 gives the resulting expression.

$$EI_{eff} = E_s I_s + C' E_c I_c \qquad \text{(Eq. 5-1a)}$$

$$C' = 0.15 + \frac{P}{P_0} + \frac{A_s}{A_s + A_c} < 0.9 \qquad \text{(Eq. 5-1b)}$$

The subscripts s and c refer to the steel, concrete section, respectively. The variables E and I are the elastic modulus and moment of inertia.

The expression was calibrated to provide an estimate of the secant CFT stiffness corresponding to 90% of the ultimate bending moment for the given axial load. This level of stiffness is appropriate to estimate a lower-bound global column buckling capacity and for seismic evaluation. This value is used also for the moment-rotation expression provided below. Fig. 5-4 compares the measured stiffness to the stiffness predicted by Eq. 5-1a and b.

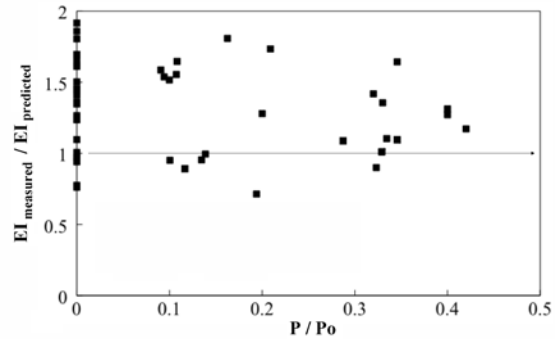

Figure 5-4. Comparison of Proposed Stiffness Models to Measured Stiffness

FLEXURAL STRENGTH

The flexural strength of a CFT member is determined using the plastic stress distribution method (PSDM) described in Section 2.2. The PSDM method is equilibrium based and uses uniformly distributed stresses in tension (steel) and compression (steel and concrete) to approximate the actual stress distribution, as shown in Fig. 5-5. The magnitude of the stresses depends on the material properties, specifically the full yield stress is used in the steel (both tension and compression) and a uniform compressive stress of 0.95 times the compressive strength of the concrete, f'_{ct}. It is noted that the 0.95 coefficient is larger than the 0.85 typically used for the Whitney stress block calculation (ACI 318), to simulate the confinement provided by circular tubes. The neutral axis depth is determined by solving the equilibrium condition such that the summation of the resulting forces of the steel in tension and compression as well as the concrete in compression, equal the axial force applied to the members. That resulting geometry is used to determine the moment associated with that axial load.

This method can be used to generate a full P-M interaction curve, as shown in Figure 5-5b. For each neutral axis depth, pairs of axial and bending resistances can be determined. A result is shown as a dimensionless interaction curve in Fig. 5-5b, for which the values on the moment (x axis) and axial load (y axis) are normalized to the flexural strength without axial load (M_o) and the axial crush load without moment (P_o) of the member, respectively. Smaller D/t values result in larger resistance, because the area of steel is larger. Larger D/t ratios result in

significantly increased bending moment for modest compressive loads, because of the increased contribution of concrete fill as shown in Fig. 5-5b.

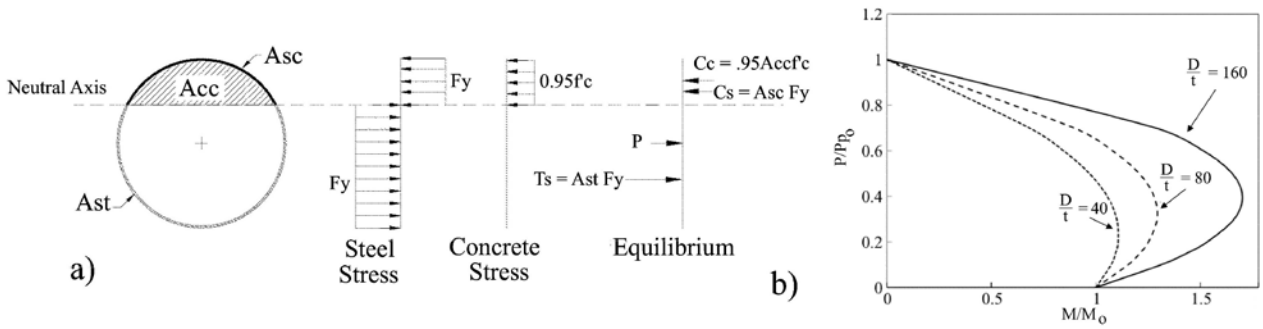

Figure 5-5. Strength Determination; a) Plastic stress distribution method, b) Material-based interaction curves (no buckling)

This interaction curve is based on cross-section equilibrium and material properties, and is sometimes termed a material interaction curve or a theoretical interaction curve. A closed-form solution has been derived based upon the geometry described in Fig. 5-6 and is expressed in Equations 5-2.

$$r_m = r - \frac{t}{2} \qquad \text{(Eq. 5-2a)}$$

$$\theta = \sin^{-1}\left(\frac{y}{r_m}\right) \qquad \text{(Eq. 5-2b)}$$

$$c = r_i \cos\theta \qquad \text{(Eq. 5-2c)}$$

$$P = F_y t\, r_m \left\{(\pi - 2\theta) - (\pi + 2\theta)\right\} + \frac{0.95 f'_{cd}}{2}\left\{(\pi - 2\theta) r_i^2 - 2yc\right\} \qquad \text{(Eq. 5-2d)}$$

$$M = 0.95 f'_{cd} c\left\{\left(r_i^2 - y^2\right) - \frac{c^2}{3}\right\} + 4F_y tc\frac{r_m^2}{r_i} \qquad \text{(Eq. 5-2e)}$$

A positive value of P implies a compressive force, and y and q are positive with the sign convention shown in Fig. 5-6. The variable y varies between plus and minus r_i. Solving the equations for selected points in this range and connecting the points generate the P-M interaction

curve. This formulation can be readily programmed into a spreadsheet to form the interaction curves for specific tubes, as illustrated in Fig. 5-5b.

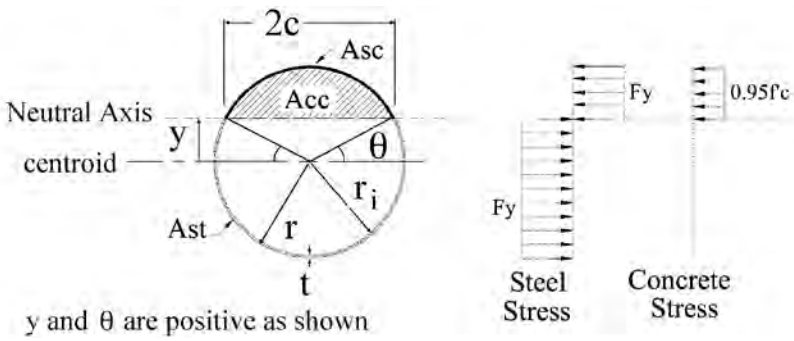

Figure 5-6. Geometry Used for Closed Form Derivation of Stress Distribution Prediction

Analysis of prior test data suggests that the method provides an accurate yet conservative prediction of the flexural strength for a wide range of axial load ratios and tube geometries. It is noted that some of the points fall below the measured-to-predicted strength ratio of 1.0, however the strength prediction ratio for the majority of these tests is 1 or larger. The data suggests that the ultimate flexural strength can be predicted by multiplying the strength determined from the PSDM by a factor of 1.25. This ultimate strength is not expected to be used in strength design but could be used in a capacity-based design method to design the adjacent components (see section on nonlinear analysis below). The data suggest that there is some impact of the tube geometry (D/t ratio) and axial load ratio (P/P_o). The following two sections address appropriate limits and methods to account for these factors.

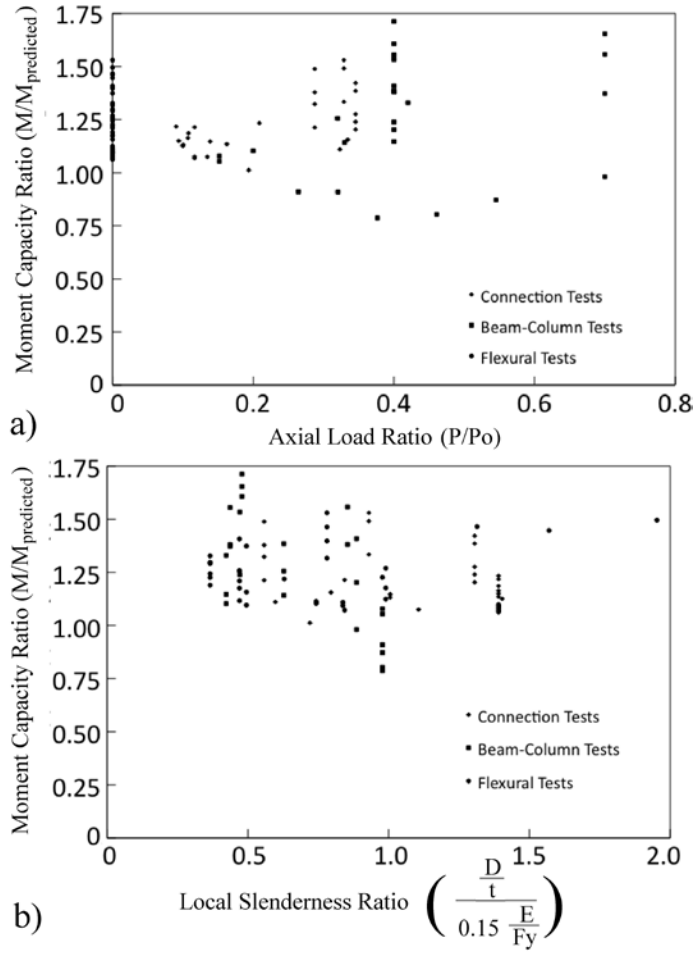

Figure 5-7. Comparison of Measured to Predicted PSDM Resistance a) As function of P/P_o, and b) As a function of D/t of the tube

GEOMETRIC LIMIT FOR TUBES

To develop the full plastic capacity of CFT member, it is necessary to ensure local buckling does not occur prior to development of the strength of the tube. This is accomplished by providing an upper limit on the D/t ratio of the tube. Chapter 4 has shown that CFT with the foundation connection achieve greater ductility with increased inelastic deformation capacity, because much of the inelastic deformation is contributed by yielding of the encased steel in the embedded connection. For typical CFT applications with 50 ksi steel and structural concrete (4 ksi or above), the recommended slenderness limit is:

$$\frac{D}{t} \leq 0.22 \frac{E}{F_y} \qquad \text{(Eq. 5-3a)}$$

IMPACT OF COLUMN BUCKLING ON P-M INTERACTION CURVE

Typical bridge piers are relatively stocky and usually are not strongly affected by P-Δ moment or other secondary effects. However, because of their inherent strength and stiffness, CFT columns may be significantly lighter and more slender than reinforced concrete piers. As a result, it is necessary to adjust the material interaction curve shown in Fig. 5-5b to account for stability and slenderness effects. To do this, it is necessary to employ the flexural stiffness, EI_{eff}, of the CFT pier, provided in Eq. 5-1.

Global column buckling is determined by the equations provided in AISC and repeated here for clarity (Eq. 5-4):

$$P_{cr} = 0.658^{\frac{P_o}{P_e}} P_o \qquad \text{for stocky columns,} \qquad \text{(Eq. 5-4a)}$$

$$P_{cr} = 0.877 P_e \qquad \text{for slender columns, and} \qquad \text{(Eq. 5-4b)}$$

$$P_o = 0.95 f'_c A_c + F_y A_s \qquad \text{(Eq. 5-4c)}$$

where P_e is the elastic buckling load by the Euler equation ($\pi^2 EI / (KL^2)$, and A_c and A_s are areas of the concrete and steel, respectively.

The interaction curve including stability effects is a modified version of the material interaction curve (Fig. 5-5b), which forms its basis. A series of points are joined to form the plot. The points are as defined as follows:

- Points *A* and *B* are the axial and flexural capacity of the CFT by the PSDM.
- Point *C* corresponds to the location on the PSDM interaction curve that results in the same moment capacity as point *B* but with axial load.
- Points *A'* and *C'* are obtained by multiplying the axial load associated with points *A* and *C* by the ratio, $P_{cr}/P_{o,AISC}$.

- Point *D* is located on the PSDM interaction curve and corresponds to one half of axial load which is determined for point *C'*.
- Point *A"* is the intersection of PSDM *P-M* interaction and line parallel with *5*-axis through the point *A'*.

The resulting curve accounts for global buckling of the tube and an example is shown in Figure 5-8. The axial strength is limited to point *A'* (or the AISC buckling capacity). The stability based *P-M* interaction curve is then constructed by connecting points *A'*, *A"*, *D*, and *B,* as shown in the figure. This interaction curve should then be used for strength design of the CFT member for all load conditions. Seismic design requires that less ductile elements be designed for the expected maximum plastic capacity of the ductile members. Given a specified axial load, the expected maximum bending moment of the CFT will be 125% of the moment obtained from the interaction curve and this is the demand that should be used to design any less-ductile connecting elements.

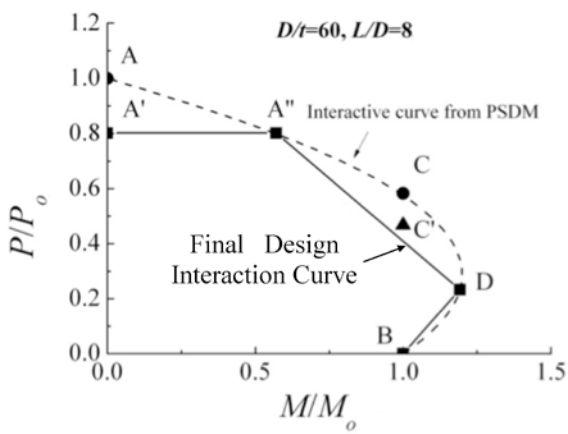

Figure 5-8. Construction of the Stability-Based Interaction Curve

5.3. **FOUNDATION (OR CAP-BEAM) CONNECTION DESIGN**

The foundation connection design for the CFT must consider several different factors. A central part of this research study is the design and detailing of the connecting portion of the CFT to the foundation or cap-beam. The connection design should include:

1. Detailing/sizing of the annular ring
2. Determination of the embedment depth
3. Punching shear evaluation
4. General design (flexure and shear) of the connecting (foundation or cap-beam) element to sustain the CFT column demands.

DETAILING OF ANNULAR RING

An annular ring is welded to the end of the tube to provide anchorage and stress distribution, as illustrated in Fig. 5-3. The ring is made of steel of the same thickness and yield stress as the steel tube. The ring extends outside the tube 16 times the thickness of the tube and projects inside the tube 8 times the thickness of the tube. This gives a width of the ring of 25 times the thickness of the tube, as shown in Fig. 5-9.

The ring is welded to the tube with complete joint penetration (CJP) welds of matching metal or fillet welds on the both the inside and outside of the tube. The fillet welds must be capable of developing the full tensile capacity of the tube, and for this purpose the minimum weld size, w, of the fillets can be defined by Equation 5-5.

$$w \geq (F_u\, t)/(0.75\ (2)\ 1.2\ (0.6)\ F_{EXX}\,(.707)) = 1.31 F_u\, t/F_{EXX} \qquad \text{(Eq. 5–5)}$$

where F_{EXX} and F_u are the minimum tensile strength of the weld metal and tube steel, respectively. The CJP or fillet welds should as a minimum satisfy the AISC Demand Critical Weld toughness criteria (AISC 2005).

The tube and the annular ring are embedded into the reinforced concrete footing with an embedment depth, l_e, needed to assure ductile behavior of the connection as depicted in Fig. 5-9. This minimum embedment length is defined as:

$$l_e \geq \sqrt{\frac{D_o^2}{4} + \frac{DtF_u}{6\sqrt{f'_{cf}}}} - \frac{D_o}{2} \qquad \text{(Eq. 5-6)}$$

The footing concrete will have a minimum compressive strength, f'_{cf}, in units of psi. The variable D_o is the outside diameter of the annular ring for the embedded connection as shown in the figure, and F_u is the minimum specified tensile strength of the steel. For the grouted connection, D_o is the diameter of the corrugated metal form surrounding the ring, which is typically 50 to 100 mm (2 to 4 in.) larger than the diameter of the annular ring.

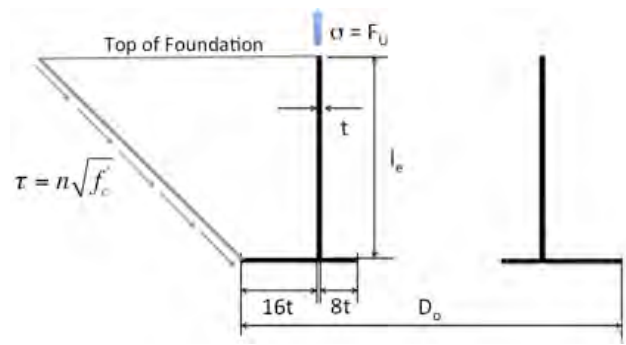

Figure 5-9. Cone Pullout Requirements for the Embedded Connection

The tube must have adequate concrete depth, *h*, below the concrete filled tube to avoid punching through the base of the footing. Several methods may be used for punching shear evaluation, but the current ACI procedure for single shear (ACI 318 2011 is recommended as a conservative approach. In compression, the column carries the axial force (P_u) and the compression force from the moment couple from the same load case. However, unlike the tension case, the data show that a portion of the compressive force is distributed to the foundation through bond. This is similar to the force transfer mechanism for a reinforced concrete column. In compression, the column carries the axial force (P_u) and the compression force from the moment couple from the same load case. However, unlike the tension case, the data show that a portion of the compressive force is distributed to the foundation through bond. This is similar to the force transfer mechanism for a reinforced concrete column.

$$C_{max} = C_s + C_c \qquad \text{(Eq. 5-7a)}$$

$$l_e \geq \sqrt{\frac{D^2}{4} + \frac{C_{max}}{4\sqrt{f'_{cf}}}} - \frac{D}{2} \qquad \text{(Eq. 5-7b)}$$

Where C_c and C_s are the compression forces in the concrete and the steel due to the combined bending and axial load as computed by the PSDM for the most extreme combined load case. Using the ACI expression for gives the required total depth of the footing, d_f.

FOOTING OR PILE CAP DESIGN

The footing must follow conventional design practice and must be adequate to sustain the foundation design loads. As a result, the concrete, reinforcement and footing thickness usually will be identical to that required by normal footing design for most cases. However, the total concrete footing thickness, d_f, must be large enough to control punching shear and cone pullout of the CFT column. The width and length of the footing, b_f, must be large enough to accommodate the concrete struts of 60 degrees from the vertical originating at the base of the ring, as indicated in Eq. 5-8.

$$b_f \geq D_o + 3.5 l_e \qquad \text{(Eq. 5-8)}$$

The shear and flexural reinforcement in the footing must be designed for the normal shear and flexural loadings based upon the bridge loads, the soil conditions, and the expected capacity of the CFT pier. The longitudinal and transverse flexural reinforcement should be spaced uniformly across the length and width of the footing, but the top layer of flexural reinforcement will be interrupted by the concrete tube. The longitudinal bars that are not interrupted by the tube must be designed with adequate capacity to develop the required foundation resistance. The interrupted bars are needed, but these bars do not contribute to the flexural strength of the footing. Figure 5-10 shows the configuration of the longitudinal reinforcing bars that do not penetrate the tube but are placed within the tube diameter. Each of the bars was hooked using the provisions in ACI 318-08 Chapter 12. The hooked length is equal to $12d_b$, where d_b is the diameter of the longitudinal bar. The hook radius depends on the bar size. Using this detailing for the longitudinal bar permit development of the full yield strength.

The shear reinforcement in the footing must be designed to meet the shear demand. The vertical reinforcement used to resist the shear must meet an additional constraint within the anchorage region of the embedded tube, such that at least two (2) vertical bars intersect the cone depicted in Fig. 5-9. Figure 5-10 show a typical vertical reinforcement layout. Therefore vertical

ties spaced no greater than s in the region within $1.5l_e$ of the outside of the tube, as defined by Eq. 5-9.

$$s \leq \frac{l_e}{2.5} \qquad \text{(Eq. 5-9)}$$

In addition, it is noted that the required embedment results in a shear stress in the critical area surrounding the tube (Figure 5-9) of $6\sqrt{f'_c}$(psi). Assuming the concrete is capable of resisting a shear demand of $2\sqrt{f'_c}$(psi), the vertical reinforcement required by Equation 5-9 should be designed to resist $4\sqrt{f'_c}$(psi).

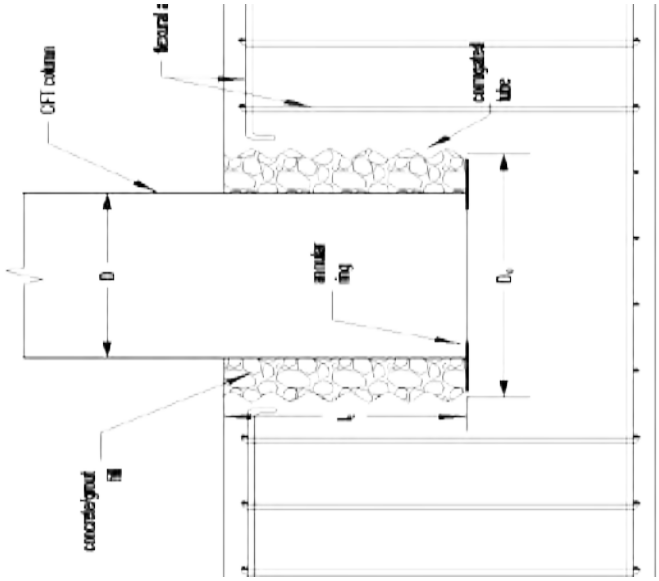

Figure 5-10. Detailing of Reinforcement Adjacent to the Tube

5.4. **NONLINEAR CONNECTION MODEL**

Analysis of a CFT bridge subjected to seismic loading can require nonlinear models of the components. The models can be used to conduct a pushover analysis to establish the deformation capacity of the system or to conduct a nonlinear response history analysis. In a CFT system, the majority of the inelastic action results from the base of the column and the connection. In RC systems, it is common to use a plastic hinge length modeling approach. This approach can also be use for a CFT system, however it was outside the scope of this research

project. Instead, the research focused on the use of an elastic perfectly plastic moment rotation curve is recommended, as shown in Fig. 5-11a. The model requires:

- An estimate of the flexural strength (moment capacity)
- An estimate of the elastic stiffness
- An estimate of the rotational capacity.

The first two properties have been discussed previously. The moment capacity is determined from the stability P-M interaction curve, which includes the PSDM. Since nonlinear seismic analysis is commonly based upon expected inelastic behavior, the ultimate moment capacity as determined from the interaction curve should be increased by a factor of 1.25 to account for overstrength effects. The elastic stiffness of the moment-rotation curve can be defined by the stiffness equations provided previously.

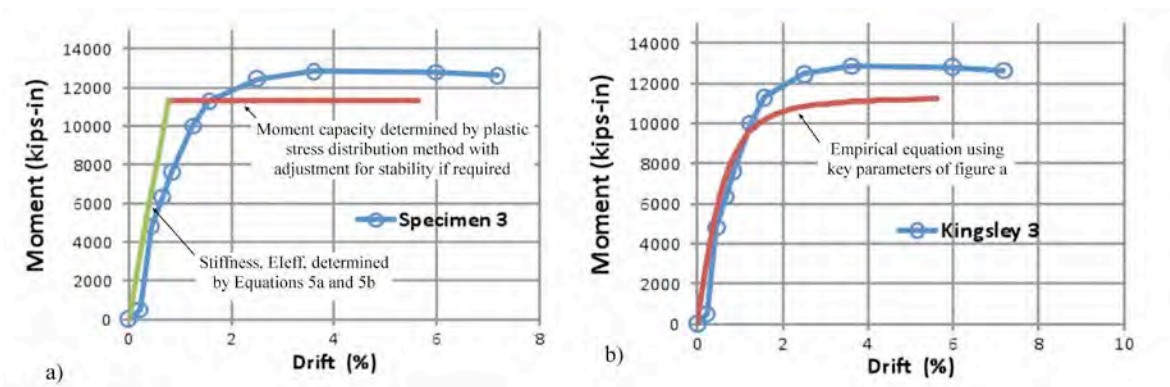

Figure 5-11. Proposed Models for Nonlinear Deformation of CFT Piers

The nonlinear flexural response can be considered as a concentrated end rotation with little loss of accuracy in performance. This simple elasto-plastic model has a sharp transition between elastic and plastic behavior, which is different than commonly used with fiber or section models.

CFT have a gradual transition to full nonlinearity, because of the progression of yielding of the steel around the circumference of the tube and the nonlinear normal response of the concrete. Hence, an alternate model with a smooth transition between elastic and plastic behavior is proposed and illustrated in Fig. 5-11b, and is based on the Giuffre and Pinto model.

This second model also uses the moment resistance obtained from the P-M interaction curve methods and the elastic stiffness model described earlier. The moment-rotation behavior is defined by an empirical curve:

$$M = \left[\theta \Big/ \left(1+\theta^{R}\right)^{1/R} \right] M_u \qquad \text{(Eq. 5-10a)}$$

where

$$\theta = \frac{\Delta}{\Delta_p} \qquad \text{(Eq. 5-10b)}$$

$$\Delta_p = M_u / K \qquad \text{(Eq. 5-10c)}$$

In the expressions, K is the elastic stiffness of the deflection parameter, Δ, and it depends on EI_{eff}, the boundary conditions, and mechanics of the application. The variable R is an empirical term calibrated to the experimental results; $R=4$ is recommended based upon comparison to past CFT experiments and simulations. Both models are simple to employ and they result in better accuracy than that achieved by sectional analysis.

The deformation limits depend upon the performance objectives. The proposed limits are conservatively based on the 19 connection tests completed (including 7 completed as part of this research program). The connection rotation, θ, is defined as the ratio of the deflection at the inflection point of the column, Δ, and the length of the tube, L_t, from the top of the footing to the inflection point.

$$\theta = \frac{\Delta}{L_t} \qquad \text{(Eq. 5-11)}$$

To avoid initiation of tearing of the tube, θ should be limited to:

$$\theta \leq \frac{0.065\left(l_e + 16t\right)}{D} \qquad \text{(Eq. 5-12)}$$

Where l_e is the embedment depth required by Eq. 5-6. At this rotation limit, there will be very little deterioration in resistance. It must be emphasized that these limits are not for general CFT applications but for the specific proposed CFT pier and foundation connection, because of the distribution of yielding occurring in this connection.

5.5. **EXPECTED SEISMIC PERFORMANCE**

CFT construction is a practical, efficient, and effective construction method for a wide-range of structural applications including bridges. However, the connection of piers and columns to the foundation is critical in ensuring good system performance and only limit study of these connections has been conducted.

The results of this research project indicate that CFT bridge columns are capable of achieving large strength, stiffness, and displacements with proper detailing of the connection. However, the benefits of the proposed CFT column and connection extend beyond these properties. The inelastic performance and deformation capacity of the circular CFT pier and foundation studied as part of this research program is significantly better than that achieved with reinforced concrete piers.

A comparison of the seismic performance of CFT and RC bridge columns is offered in Fig. 5-12. The figure shows the moment-drift angle behavior of a CFT and comparable reinforced concrete (RC) bridge pier. The CFT pier was tested as part of this research study, and the RC pier is of nearly identical length and diameter and meets the provisions of Caltrans Seismic Design Manual (Pang et al. 2008). The two piers were both 20 in. (505 mm) in diameter and had nearly identical length, weight and quantity of concrete. The RC pier has approximately 2.2% of volume of 60 ksi (420 MPa) reinforcing steel for combined shear and flexure. The CFT pier has approximately twice that volume of 50 ksi (350 MPa) steel. Both columns were loaded to approximately 11% of their gross axial capacity of the concrete. The total moment capacity of the CFT column is more than double that of the RC column, as shown in the figure. Therefore, for the same size, the CFT column offers strength well beyond the RC column.

However, the differences extend beyond the strength; there are pronounced differences in the seismic performance. At approximately 3% drift, the RC column sustained significant cracking with severe spalling of the concrete cover, however the CFT column has sustained only limited yielding; slight buckling of the tube has initiated, as shown in the photos. At 5.5% drift, the CFT column has significant local buckling, but the resistance has not deteriorated as shown in the figure. As this same drift level, the concrete cover of the RC column has spalled and the spiral reinforcing is exposed, which requires post-earthquake repair.

	CFT Pier and Foundation Connection - Specimen 14	RC Pier and Foundation Connection (Pang et al. 2008)
Moment-Drift Behavior	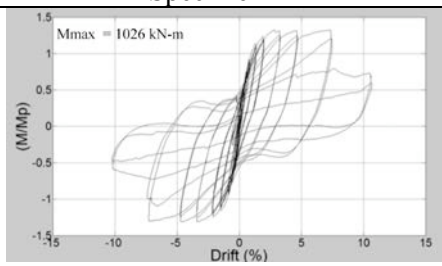	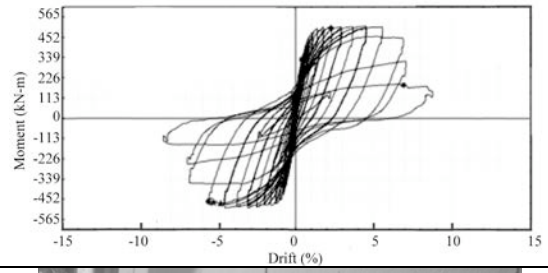
Photos at 3% Drift		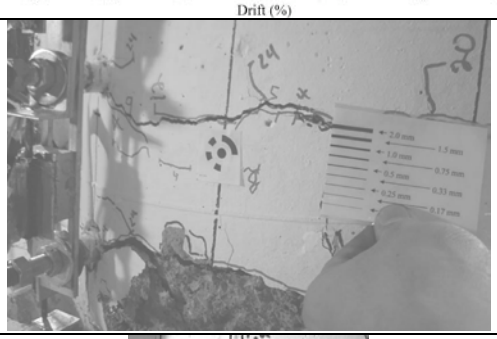
Photos at 5.5% Drift	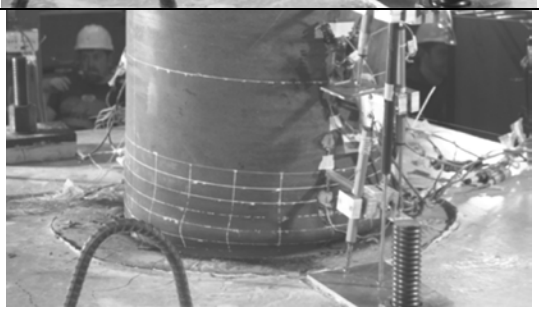	
Photos at 8.8% Drift	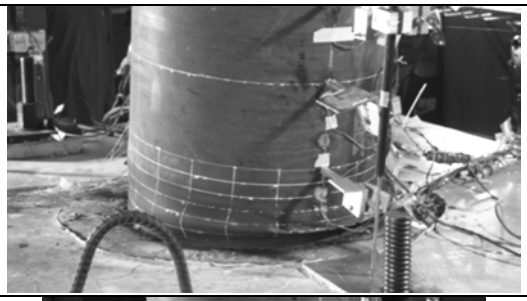	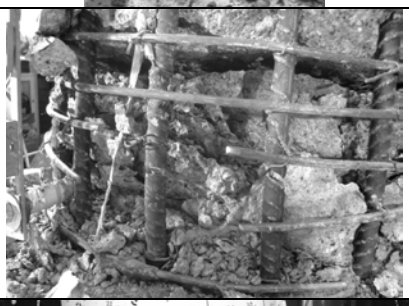
Photos at 10% Drift for CFT and 8.9% for RC	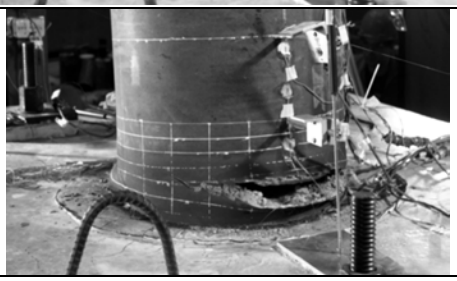	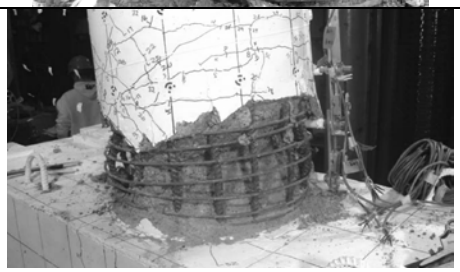

Figure 5-12. Comparison of RC and CFT Pier Performance

Additional deformation results in bar buckling, core concrete damage and deterioration of the RC column. At approximately 7% drift, the RC pier retains only 20 to 30% of its maximum moment resistance, while the CFT pier has not sustained any significant deterioration. At approximately 7.5% drift, deterioration in resistance is first noted for the CFT member. At 8.8% drift, the RC column has sustained fracture of both the flexural and spiral reinforcement and the specimen has lost all moment resistance. At this same deformation, initiation of tearing is noted at the local buckle of the tube due to repeated cyclic inelastic deformation, but 30 to 40% of the maximum moment resistance remains. The CFT pier continues to retain quantifiable resistance until and drift of approximately 10%, when the tear has progressed around a significant portion of the diameter of the tube as shown in the figure. This result demonstrates that the CFT column sustained deformation without deterioration well beyond this level, showing its superior damage resistance and deformability relative to conventional reinforced concrete columns.

5.6. **POST EARTHQUAKE INSPECTION AND EVALUATION**

Post earthquake inspection is an important aspect of bridge maintenance, and Fig. 5-12 provides considerable guidance about the expected seismic performance of CFT pier columns and foundation connections. For CFT, deterioration or damage is visible, because it is a result of severe local buckling and ultimately tube tearing. Therefore post-earthquake maintenance should be quite easy and direct for this CFT pier and foundation connection. First and foremost, the permanent deflection of the pier should be noted, because this is very likely to define requirements for repair or replacement of the CFT element or the bridge. If the connection is adequately embedded into the concrete foundation, cracking of the footing or pile cap should be minimal. If severe cracking is noted, this implies that the connection was not embedded to an adequate depth. Figure 5-13a shows severe footing cracking that would be expected if the embedment depth does not meet that specified by Eqn. 5-6. If the CFT pier has been subject to large inelastic deformations, some footing cracking may be noted as depicted in Fig. 5-13b, but this cracking will not result in any measurable loss of stiffness or resistance.

Figure 5-13. Footing Damage; a) Severe resulting from cone pullout of connection with inadequate embedment, b) Moderate due to large inelastic deformations

The expected damage of these CFT pier columns and connections (illustrated in Figure 5-13) is flexural yielding of the tube, including tube buckling at moderate drifts and tearing at large levels of drift. This yielding is directly observable, since the steel is directly exposed. If the steel is physically buckled (this would indicate large residual buckling, and not initial buckling), the confinement of the concrete inside the tube within the buckled region is reduced and concrete damage may initiate. The critical aspect of damage that impacts response is tube tearing. Therefore, the buckled region should be closely examined to determine if tearing has initiated. If tearing has not initiated, the pier has not sustained significant loss of stiffness, resistance, or deformation capacity. The magnitude and extent of inelastic deformation that could be tolerated in future earthquakes depends upon the severity of damage due to the prior event. The decision to repair or replace and the priority of any such action are then primarily dependent upon the extent of yielding, the permanent offset and the serviceability of the bridge. However, if local tearing has initiated, significant deterioration of resistance and stiffness must be expected although the CFT column will continue to sustain large axial load capacity. However, additional cyclic demands may result in additional tearing of the tube it is expected that the tube would need to be repaired prior to a future significant earthquake. A number of repair or retrofit strategies are possible with CFT piers, including jacketing. However, none of these strategies have been experimentally verified or tested, and they are therefore not included in this document.

5.7. **DESIGN EXAMPLE FOR LIVE LOAD STRENGTH DESIGN**

This example aims to redesign conventional reinforced concrete bridge columns as concrete-filled tube bridge columns using the design recommendations and expression provided in this report.

A two-column bridge bent was redesigned using CFT columns and column-to-footing connections. The columns are 44' in height (to the base of the bridge deck.) The column was originally designed as a reinforced concrete column. The column diameter was 6'-0". A total of 36 No. 11 bars were used as longitudinal reinforcement. The transverse hoops were No. 8 bars spaced at 5 in. on center in the plastic hinge region. The resulting longitudinal reinforcement ratio was 1.4%. The effective horizontal reinforcement was approximately 1.1%. For the cross section, the total steel area/foot was the area of the vertical steel = 36*1.56 = 56.2 in^2 + area of a hoop per foot = 1 in^2*68 in*pi*(2.4/12 in) = 13.6 in^2 = 69.8 in^2.

In the original problem the bridge was analyzed using the in-house program available at the California Department of Transportation. The results were used for the design of the CFT column bridge.

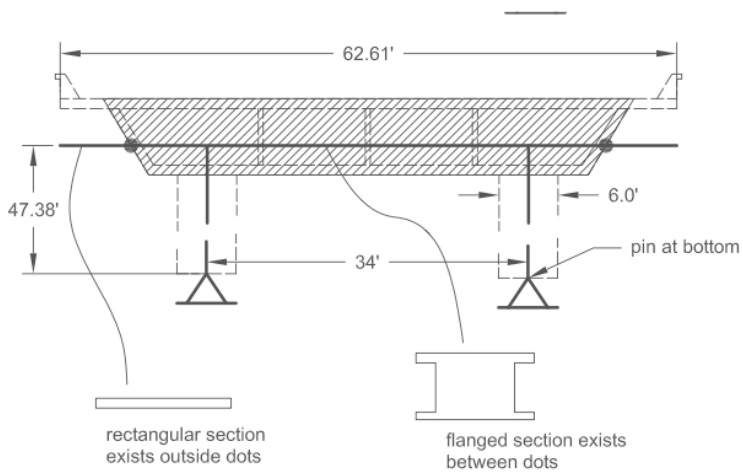

Figure 5-14. Elevation of Bridge Used in Design Example

DESIGN PROCESS

The columns were redesigned using the following procedure. This procedure is similar to the procedure currently used by Caltrans to design RC columns.

1. Determine the factored load demands (axial, bending and shear) on the columns. (Note, in the example, these demands were adopted from the results WinYield, as presented in Appendix A).

2. Find initial estimate of the column diameter and tube thickness to sustain the axial load such that $0.1<P/P_o < 0.2$ for the full range of loading. Initial estimates of D/t between 80 and 100.
3. Determine the effective stiffness of the column.
4. Using the effective stiffness, determine the moment magnification factor for the column, δ_s.
5. Magnify the moments by the magnification factor.
6. Determine the required M_n and P_n combinations for each load case, i.e., M_u/ϕ and P_u/ϕ where ϕ=0.75 for most live loads and ϕ=1.0 for seismic load case
7. Compute the P-M interaction curve
8. Compare the computed demands and capacities.
9. For the designed column, find the required connection (embedment depth) to the foundation.

MATERIAL PROPERTIES

f'_c = 4000 psi
E_c = 3,605 ksi
E_s = 29,000 ksi
F_y = 50 ksi (note, f_y = 60 ksi for reinforcing steel. 50 ksi typical for tube steel.)

LOADS
The critical load case is the live load strength load case:
Str-II 2 M_u = 3542 k-ft P_u = 2949 k

DESIGN

1. Initial size

   Bridge piers commonly have axial loads in the range of $0.1P_o$ to $0.2P_o$ where:
   $P_o = \pi*D*t*f_y + 0.95*D^2/4*\pi*f'_c$ (Equation 5.4c)
   Target D/t = 80

   The maximum value of P_u is 2949 kips but normal service operations and dead load only are smaller values in the order of 1200 kips.
   Therefore, solve the quadratic for D given an initial estimate of t.

   Try D = 50 in. and t = 0.625 in. (5/8 in.). Resulting D/t is 80.
   For this combination, P_o is 16,279 kips and, and the axial load capacity falls into typical range of $0.074P_o$ to $0.18P_o$. This is typical of that expected for bridge pier design.

2. Determine effective stiffness of column (EI_{eff}) (using Eqs. 5-1 a and b)
   Note, EI_{eff} depends on the axial load ratio.

For dead load only, P ≈ 1200 kips, and EI_{eff} = 8.0e06 (k-ft^2)
(compare with 8.137e06 k-ft^2 for original RC column). δs = 1.4
For live load case, P_u = 2949, EI_{eff} = 12.9e06 (k-ft^2)
(compare with 10.498e06 k-ft^2 for original RC column) δs = 1.0

Note, that the effective stiffness values are close to original column and therefore same moment magnification factors are used. The resulting demands are provided in the following table.

Load Case	P_u (k)	M_u(k-ft)	δ_s*M_u(k-ft)	P_u/ϕ, δ_s*M_u/ϕ	
Str-II 2	2949	3542	4959	4213	7084

3. Compute P-M interaction diagram
The P-M interaction diagram was computed using the procedure laid out in the chapter. First, the theoretical P-M interaction surface was computed from the plastic stress distribution process. Then impact of geometric nonlinearities was considered to develop the design interaction diagram. The demands are shown in the final column of the table and the plot below. As seen from the plot, the column has adequate capacity to sustain the combined loading combination. (Equations 5-2 a through e, with stability adjustment as described on page 76 with Equations 5-4 a through c)

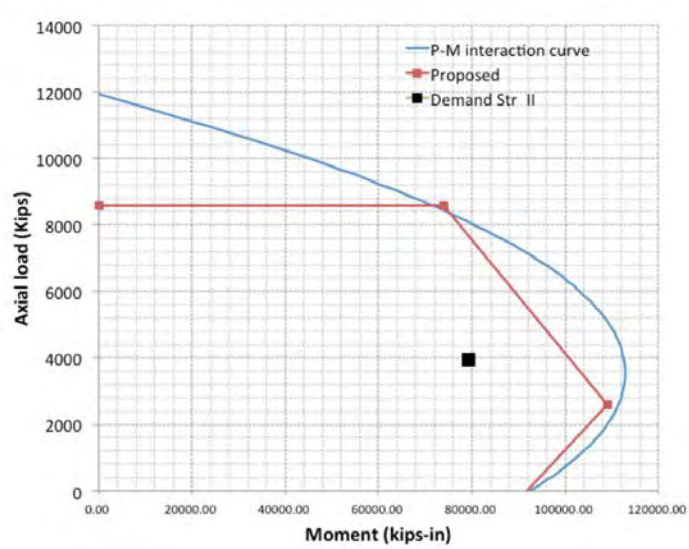

Figure 5-15. P-M Interaction Diagram of Column Example.

4. Shear strength
   The shear capacity of the section was computed assuming that only the steel contributes to the strength. This computation is conservative but in almost all cases, bridge columns are sufficiently long that this will not control the design. The following expression is adopted from AISC 2010.

   $V_n = 0.6f_y*A_v$ where $A_v=0.5A_s$ (AISC 2010)

   V_n=1545 k
   $\phi V_n = 0.75*V_n$ = 1159 k
   Maximum shear force, $V_u = \frac{2*113000}{12*44} = 428 kips$ OK

5. Connection Design
   The annular ring has the following dimensions:
   $t_{ring} = t_{tube}$ = 0.625 in.
   D_o (outer diameter) = D+32t = 50+32*0.625 = 70 in.
   D_i (inner diameter) = D-16t = 50-16*0.625 = 40 in.

   The connection must be embedded in the adjacent element for full fixity. For this column the embedded length is:

$$l_e = \sqrt{\frac{D_o^2}{4} + \frac{DtF_u}{6\sqrt{f_c'}}} - \frac{D_o}{2} \qquad \text{(Equation 5-6)}$$

   For the column in this example, the required embedment depth is 44 in.

   Finally, the total depth of the foundation is computed as:

$$C_{max} = C_s + C_c = P_u + T_s$$

$$l_e = \sqrt{\frac{D^2}{4} + \frac{C_{max}}{4\sqrt{f_c'}}} - \frac{D}{2} \qquad \text{(Equations 5-7 a and b)}$$

   From the PSDM analysis,
   C_{max} = 2632 kips.
   Therefore,
   d_f = 77 in.

   Use a 78 in. deep footing with 44 in. embedment depth. Total footing width is 2*44 in. + 70 in. = 158 in.

COMPARISON

The resulting CFT is 50 in. in diameter and 0.625 in thick. The RC column was 6 feet thick in diameter, with 36 No. 11 bars and No. 8 bars at 5 in. on center. The two columns have similar cross sectional stiffness values, although the CFT column is smaller. This is possible since there is a larger coefficient on the moment of inertia of the concrete to find the effective value for the CFT column relative to an RC column.

The total cross-sectional steel area is 40% larger for the CFT column, if both the longitudinal and transverse reinforcement steel areas are considered, $A_{s,CFT} = 96.95$ in^2 vs. $A_{s,RC} = 69.8$ in^2. The total diameter of the CFT column is only 69% of the original RC column.

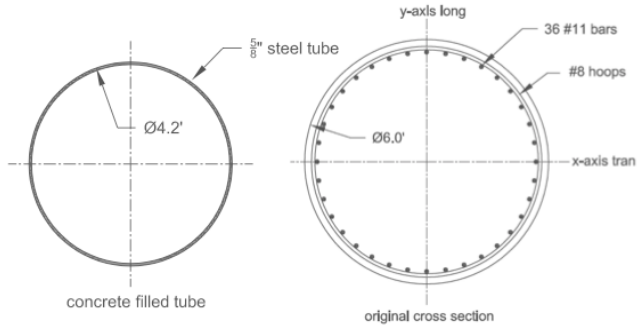

Figure 5-16. Comparison of CFT and RC Column Cross Sections

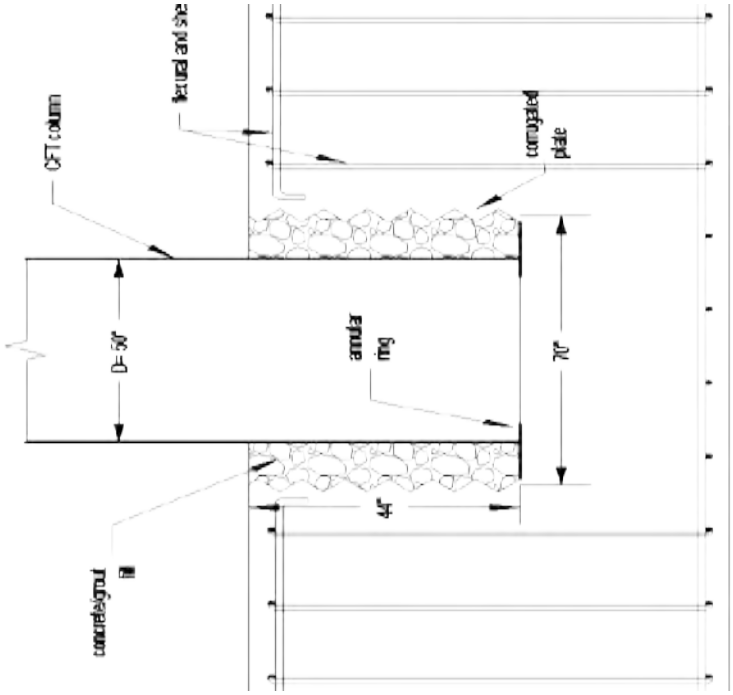

Figure 5-17. CFT Connection Design

SEISMIC COMPARISON

Seismic design requires consideration of inelastic deformation demands and a simplified comparison of the CFT and reinforced concrete prototype is also provided. This simplified evaluation is based upon the characteristics of the prototype structure provided earlier, and the standard acceleration response spectra curves provided in Appendix B of the CALTRANS Seismic Design Criteria Manual. The actual location and weight, W, of the prototype structure is unknown, but for the purposes of this comparison the response spectra curves of Fig. B.6 (0.7g peak ground acceleration with Soil Profile C) and a tributary weight of 2400 kips is employed.

The estimated period of the two 2-column bent systems becomes:

CFT:

$$T = 0.32\sqrt{\frac{W}{K}}$$

where

$$K \approx 2\,\frac{12EI_{eff}}{L^3} = 2\,\frac{12*8{,}000{,}000}{44^3} = 2254$$

and

$$T = 0.32\sqrt{\frac{2400}{2254}} = .33\text{sec}$$

Reinforced Concrete:

$$T = 0.32\sqrt{\frac{W}{K}}$$

$$K \approx 2\,\frac{12EI_{eff}}{L^3} = 2\,\frac{12*8{,}137{,}000}{44^3} = 2292$$

$$T = 0.32\sqrt{\frac{2400}{2292}} = .33\text{sec}$$

with both systems having approximately a 0.33 second period, the given spectral acceleration is approximately 1.8g, and the estimated seismic deflection, Δ, is

$$\Delta \approx \frac{1.8*2400*12}{2254} = 23 inches$$

$$\Delta \approx \frac{1.8*2400*12}{2292} = 22.6 inches$$

Since the columns are effectively in double curvature with hinges at both ends the effective ductility demands for the two options are:

$$\theta = \frac{23}{2*22*12} = .044 radians$$

Capacity is defined by Equation 5-12

$$\theta_c = \frac{0.065(44+16*0.625)}{50} = 0.07 \geq 0.044$$

The steel tube would clearly have buckled, but, the CFT pier retains it full stiffness and resistance and has sustained no

$$\theta = \frac{22.6}{2*22*12} = .043 radians$$

Capacity defined by X-Section analysis.

The yield displacement is 4.6 inches.

$$\theta_p = 0.043 - \frac{4.6}{44*12} = .034 radians$$

and with a 35 inch plastic hinge length, this indicates an average curvature,

permanent damage. $\phi \cong \frac{0.034}{35} = 0.00097$ rad/in. This curvature exceeds the 0.000805 rad/in limit determined from the X-section analysis.

This basic comparison shows that the proposed CFT pier column is expected to have at least equal and probably more favorable seismic performance than the reinforced concrete pier that it replaces. The CFT column has sustained local buckling, but it has retained its full stiffness and resistance with no initiation of tearing or deterioration in performance. Further, the CFT column requires less material and can be constructed more quickly. The reinforced concrete column has exceeded the maximum curvature limit recommended by the X-Section analysis.